

Three-Dimensional Radiation-Hydrodynamic Study
on the Formation of Star Clusters
Regulated by External Ultraviolet Radiation

Makito ABE

February 2016

Three-Dimensional Radiation-Hydrodynamic Study
on the Formation of Star Clusters
Regulated by External Ultraviolet Radiation

Makito ABE
Doctoral Program in Physics

Submitted to the Graduate School of
Pure and Applied Sciences
in Partial Fulfillment of the Requirements
for the Degree of Doctor of Philosophy in
Science

at the
University of Tsukuba

Graduate School of Pure and Applied Sciences

Three-Dimensional Radiation-Hydrodynamic Study
on the Formation of Star Clusters
Regulated by External Ultraviolet Radiation

(外部紫外線輻射場によって制御される
星団形成に関する 3次元輻射流体力学による研究)

Makito ABE

Doctoral Program in	Physics
Student ID	201330089
Doctor of Philosophy in	Science
Advised by	Masayuki Umemura

Abstract

The star cluster formation is a prime mode of the star formation in not only the present galaxies but also an early universe following the hierarchical cosmology. Globular clusters (GCs) are known as the oldest, velocity dispersion supported compact star cluster. The observation has suggested the relationship between the velocity dispersion σ and luminosity L exhibits $\sigma \propto L^{1/2}$ in GCs, steeper index than the other dispersion supported dwarf galaxies, which show $\sigma \propto L^{1/4}$. The origin of such separation is still unclear. Recent observations have revealed that the cosmic reionization takes place at $z \gtrsim 6$. Hence, the existence of strong ultraviolet (UV) background is predicted at the epoch of GC formation. The UV radiation significantly contributes to the state of the gas through the photoionization of hydrogen atoms, photoheating, and photodissociation of hydrogen molecules. Thus, the self-shielding effect is a prime condition to form the stars, and the dynamical property of the star cluster depend on the procedure of self-shielding effect.

In the case when the gas cloud is irradiated by a weak UV radiation, the self-shielding region immediately forms, and the stars promptly form in the shielded region (*prompt star formation*). On the other hand, if the background intensity is strong enough to photoionize the bulk of the cloud, the low mass cloud evaporate since its gravitational energy is sufficiently small contrary to the thermal energy. However, if the cloud is irradiated at the phase when the infall velocity exceeds the sound speed of the photoionized gas, the cloud continues to contract with higher kinetic energy dissipation due to its strong thermal pressure. Eventually, the cloud is self-shielded against the background radiation and begin to form the stars at a compact region (*supersonic infall*). As a result, GC-like compact star cluster form. One-dimensional spherically symmetric radiation hydrodynamical simulation have proposed such a novel branch and argued that the supersonic infall would be possible to occur at the higher ($1 < \sigma$) overdensity peaks in a Λ CDM cosmology framework (Hasegawa et al. 2009).

However, it is well known that the efficiency of self-shielding is affected by three-dimensional inhomogeneity. Moreover, in the case when the background radiation is quite anisotropic, the self-shielded region is also anisotropic. The one-dimensional calculation cannot treat such effects, thus, the contraction and star formation process in three-dimension is still open to discussing. To assess the questions, we have performed the three-dimensional radiation hydrodynamical (3D-RHD) simulation. In our simulation, three-dimensional hydrodynamics (SPH), non-equilibrium chemical reactions, radiative transfer, and gravity of the dark matter are fully taken into account. According to the prediction of the one-dimensional calculation of Hasegawa et al. (2009), we have generated the inhomogeneous gas cloud mass of $10^{6-7}M_{\odot}$ that correspond to the high σ overdensity peak, embedded them in one-sided, and isotropic background radiation field and explored the

contraction process of the cloud. Also, we have calculated the star formation in the self-shielded region and pursued the dynamics of the star cluster by N -body calculation.

As a result of 3D-RHD calculation, we have found the anisotropic ionizing structure in one-sided background radiation. However, in the case when the gas cloud is irradiated by the strong UV background at the phase of supersonic infalling, the contraction of photoionized gas with strong kinetic energy dissipation have been observed regardless of anisotropy of background radiation. Also, self-shielding and star formation takes place in the compact region of ~ 10 pc. Contrary to the supersonic infall, when the background radiation is weak, the self-shielding region immediately forms and stars begin to form before dissipating a sufficient infall energy. As a result of N -body calculation, we have found the stellar-dominated star cluster in diffuse dark matter halo in the case of supersonic infall. On the other hand, in the case of prompt star formation, resultant star clusters tend to be the diffuse, dark matter dominated stellar system. We have also compared our clusters with observation. As a result, star clusters formed via supersonic infall seems to be in good agreement with observations concerning the half-mass radius, mass-to-light ratio, and σ - L relation. As for star cluster formed via prompt star formation, their properties are similar to dwarf spheroidal galaxies rather than GCs. Our result suggests that the UV background radiation regulates the dynamics of the low mass stellar system in an early universe. In particular, regardless of anisotropy of background radiation, supersonic infall seems to be a plausible theoretical scenario for old GC formation.

Contents

1	Introduction	1
1.1	Globular Clusters: the Oldest Star Clusters in the Universe	1
1.1.1	Clue to the Galaxy Formation	1
1.1.2	Dynamical Feature of the Low-mass Dispersion-supported Systems	5
1.2	Formation of Star Clusters in Ultraviolet Background Radiation Fields	7
1.2.1	Theoretical Predictions for Globular Cluster Formation	7
1.2.2	Prospect of Ultraviolet Background Radiation at an Early Universe	9
1.2.3	Physical Model	11
1.3	Purpose of This Study	13
2	Numerical Method & Model Description	16
2.1	Basic Physics	16
2.1.1	Gravitational Contraction & Thermal Evolution	16
2.1.2	Description of Radiative Feedback and Radiative Transfer	18
2.1.3	Self-Shielding Effect	20
2.2	Numerical Method	22
2.2.1	Three-Dimensional Hydrodynamics	22
2.2.2	Cooling & Chemical Reactions	24
2.2.3	Three-Dimensional Ray-Tracing & Description of Radiative Processes	25
2.2.4	Star Formation	26
2.2.5	Setup	27
3	Results	32
3.1	Contraction of Gas Clouds in Three-Dimensional UV Background Radiation	32
3.1.1	Supersonic Infall in Anisotropic Background Radiation Field	32
3.1.2	Prompt Star Formation in Anisotropic Background Radiation Field	37
3.2	Self-Shielding and Star Formation	39
3.3	Stellar Dynamics	43
3.3.1	Mass Distribution and Stellar Density Profile	43
3.4	Comparison to Observations	47
4	Discussion	52
4.1	Formation Site of GCs Based on Our Model	52
4.2	Effect of Tidal Field	54
4.3	Velocity Dispersion Profile	54
5	Conclusions	58
A	Other Suggestive Properties of Globular Clusters	59
A.1	Specific Frequency	59
A.2	Color Bimodality	60

A.3	Age-Metallicity Relation	60
B	Realization of Random-Gaussian Density Field	63
C	Estimation of Ionizing Photon Number Incident on the Cloud	64
D	Ray-Tracing in SPH Scheme	66
	Acknowledgments	68
	References	69

Chapter 1 Introduction

1.1 Globular Clusters: the Oldest Star Clusters in the Universe

The star formation in galaxies takes place through forming a star cluster. Lada & Lada (2003) have investigated the Galactic embedded clusters and revealed that star formation in giant molecular clouds is dominated by the embedded cluster formation. For extragalactic systems, Meurer et al. (1995) have investigated nine starburst galaxies. They have found that the ultraviolet (UV) light emitted from star clusters account for on average $\sim 20\%$ of the total emitted from the galaxies, indicating that the star cluster formation is a powerful mode of star formation in starburst. Fall et al. (2005) have argued that at least $\sim 20\%$ of total $H\alpha$ emission in the Antennae galaxies emitted from the locations of the clusters. The star cluster formation seems to be a prime mode of the star formation of the galaxies. Furthermore, according to a standard hierarchical merging scenario in Λ CDM cosmology, the formation of the low-mass sub-galactic stellar system would be an especially important consideration for star formation in an early universe.

1.1.1 Clue to the Galaxy Formation

Globular clusters (GCs) are relatively massive ($\sim 10^4\text{--}6M_{\odot}$), stellar dominated star clusters, ubiquitously distributed in the galaxies regardless of the masses, morphologies of the hosts. So far, 157 GCs are identified in Milky Way (MW, Harris 1996), typically distribute in halo rather than the disc in MW. Historically, in the era when the precise picture of MW had not been well-known, the kinematics of the GCs in Galactic halo are used to infer the structure of MW. Shapley & Shapley (1919) have investigated the spatial distribution of GCs by using the RR Lyrae in the GC to determine the distance. As a result, they have found that the distance of the GCs from the sun extend across $\gtrsim 10$ kpc. The predicted size of MW is sufficiently larger than proposed ever. Moreover, they have pointed that biased distribution, implying that the sun does not locate at the center of the MW. Their report is innovative at the time and significant to progress the interpretation of the Galactic structure.

The typical color-magnitude diagram (CMD) of the GC system is displayed in the upper panel of Figure 1.1. For comparison, the CMD for Galactic open cluster (OC) also appears in the lower panel. Contrary to the GCs, OCs typically distribute in the Galactic disc. We see in the figure that there are many stars turn away from the main sequence, evolve to the giant branch, and horizontal branch (HB). The Figure 1.1 indicates that the GC is the well-evolved stellar system, differently from the OCs. Furthermore, the stars belong to GC distribute quite tightly in the CMD contrary to the one for nearby field stars (e.g., Perryman et al. 1997). Therefore, the stars in GC is thought to be simultaneously formed. In other words, GC system can be presumed to the single stellar population (SSP), that is, the stars have same metallicity and age. The age of GC is estimated by performing the isochrone fitting, i.e., the observed CMD is fitted by the isochrone predicted by the theoretical model of stellar evolution, and the age is determined at the main sequence turnoff point. Here, we have to define the distance of the GC to obtain the absolute magnitude. The determination of the distance gives the major part of the uncertainty in age estimation. The most usual approach is what using the standard candle; the distance is derived from its apparent magnitude and intrinsic luminosity. As a standard candle, RR Lyra stars are commonly adopted. In addition, helium abundance, the metallicity of the cluster also affects the estimation of the age. Krauss & Chaboyer (2003)

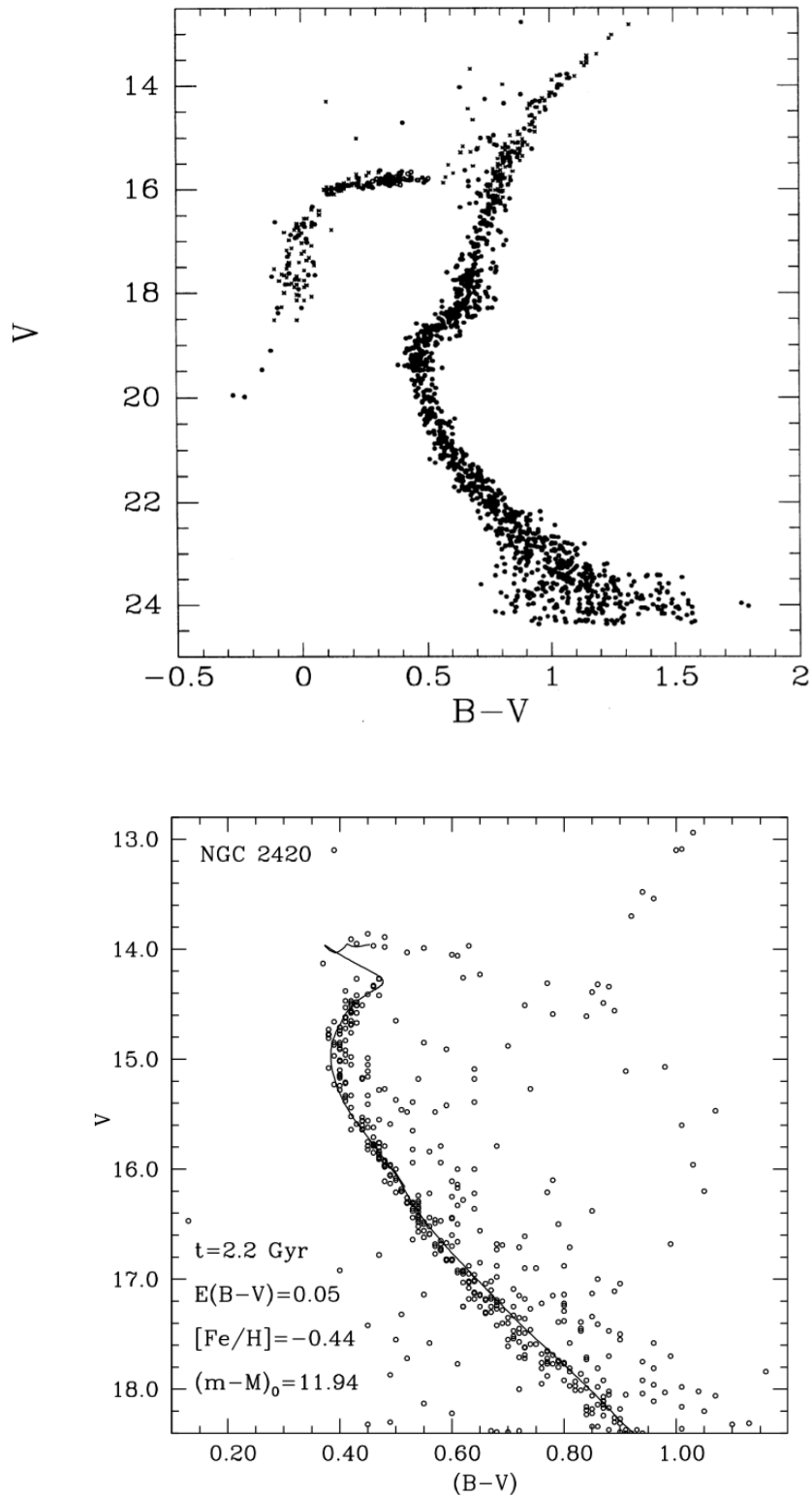


Fig. 1.1: Color-magnitude diagram of M15 (GC, upper panel) and NGC 2420 (OC, lower panel), taken from Figure 7 of Durrell & Harris (1993) and Figure 2 of Salaris et al. (2004), respectively. The vertical axis shows the $B - V$ color index, and the horizontal axis indicates the absolute V-band magnitude. For the lower panel, best-fit isochrone is also overplotted.

have applied the Monte Carlo simulation to theoretical stellar evolution model by taking into account the uncertainty of the parameters for the model and have derived the age of Galactic globular clusters (GGCs). The resultant best-fit age of GGC is 12.6 Gyr, and upper, lower limits are 10.4 Gyr and 16 Gyr in 95% confidence level, respectively (Figure 1.3). Another isochrone fitting works have also reported such old age (Dotter et al. 2007; VandenBerg et al. 2013), the typical ages of GCs somehow exhibit $\gtrsim 10$ Gyr. The age distribution of GGCs appears in Figure 1.2 as a function of $[\text{Fe}/\text{H}]$. Namely, GCs are the oldest star

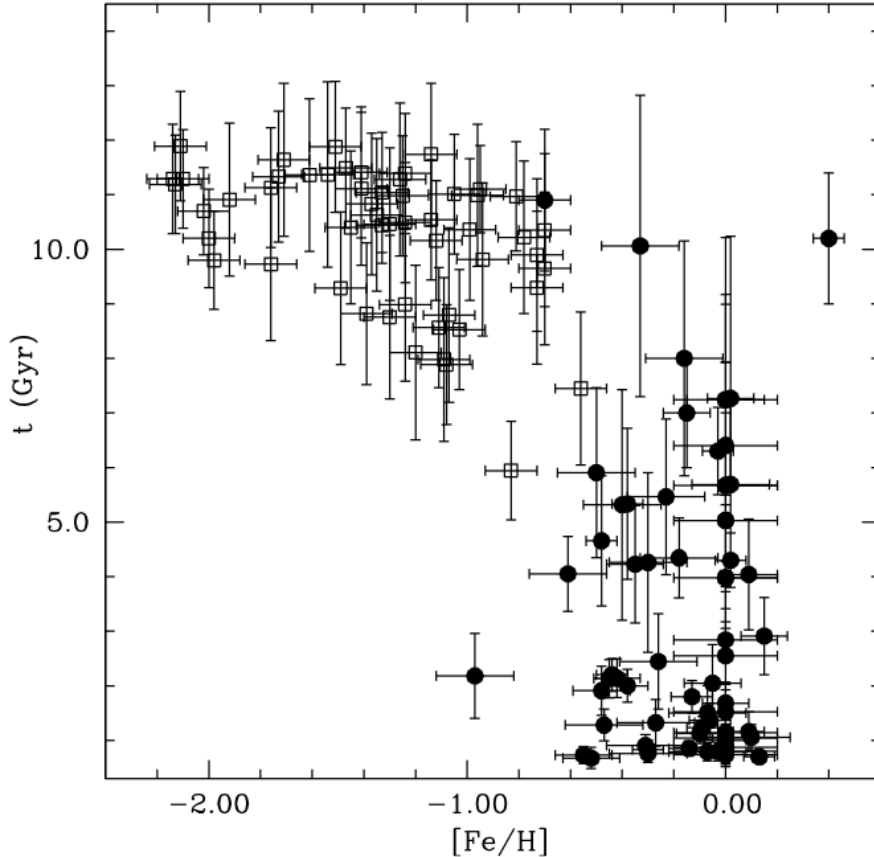


Fig. 1.2: Age distribution of Galactic GCs, taken from Figure 10 of Salaris et al. (2004). The vertical axis shows the age of the clusters, and the horizontal axis indicates the $[\text{Fe}/\text{H}]$. Open square represents the GCs, and filled circle is corresponding to OCs.

cluster ever observed, fossil remnant of the universe. Seen in this light, they can be the useful tracer of the early stage of galaxy formation. Also, the existence of GCs has a significant meaning for cosmology, in terms of limiting the age of the universe. Krauss & Chaboyer (2003) have constrained the lower limit of the age of the universe as 11.2 Gyr from their estimation of GC age. Assuming the present Hubble constant as $72 \text{ km s}^{-1} \text{ Mpc}^{-1}$ and the flat universe, they have ruled out the matter-dominated flat universe at 95% confidence level. It is remarkable that the different technique of distance-redshift relation (supernova cosmology) has obtained the same conclusion.

It might be a reasonable idea that the kinematical feature of old stars including GCs may trace the history of the Galaxy formation. For instance, Eggen et al. (1962) have investigated the relationship between the orbit of ~ 200 dwarf stars and their metallicities. As a result, they have pointed that the low-metal stars systematically exhibit significant eccentricity compared to the metal-rich stars. Furthermore, the metallicity decreases with the increasing distance from the Galactic center. Their result implies that the Galactic old stellar component seems to form at the early phase of rapid contraction of the single protogalactic system.

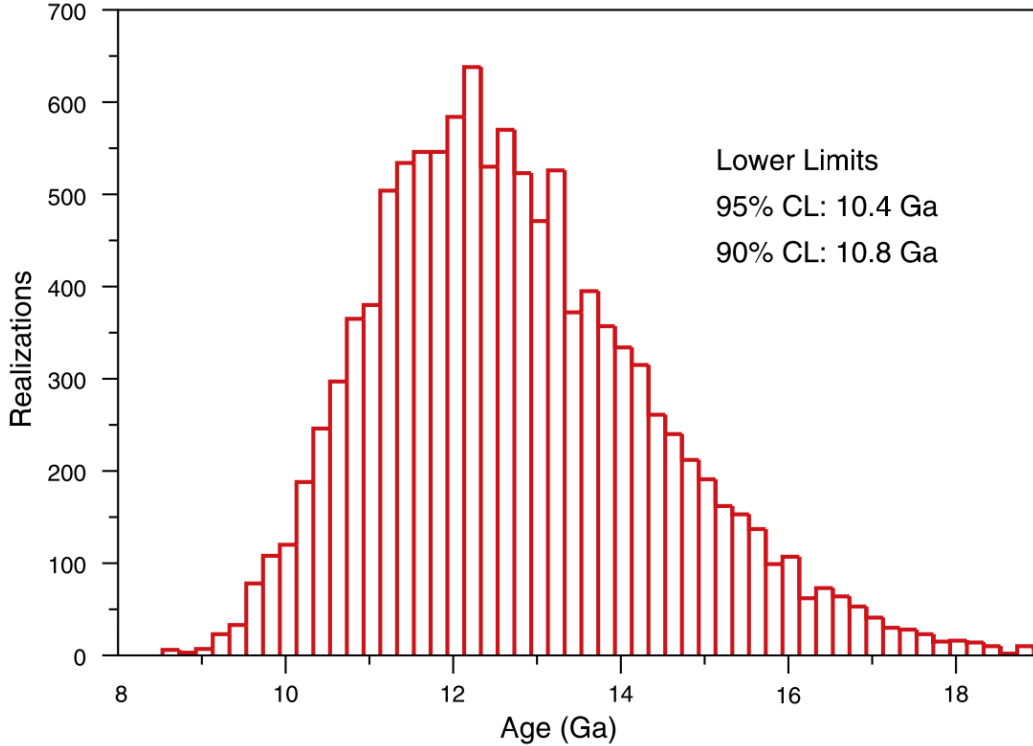


Fig. 1.3: Estimation of GGC age. Isochrone fitting with Monte Carlo simulation is performed by Krauss & Chaboyer (2003). The vertical axis shows the realization of fitting and the horizontal axis indicates the realization of the ages.

On the other hands, according to the law of conservation of angular momentum, the circular component is thought to be dominated by the progression of the collapse. As a consequence, the stars formed at a later phase exhibit circular orbit and metal-rich. Interestingly, Marín-Franch et al. (2009) have studied the age dispersion of Galactic GCs (GGCs) and mentioned that the timescale for particularly metal-poor GCs is comparable to the dynamical time of MW DM halo (~ 0.8 Gyr, Wilkinson & Evans 1999). However, subsequent more accurate analysis have found no strong correlation as Eggen et al. (1962) presented (Chiba & Beers 2000). The reason such discrepancy arises is the selection criterion. Eggen et al. (1962) have selected the only stars that have a large proper motion since the halo stars are thought to be orbiting differently from the solar neighborhood. However, the selection also excludes the intrinsically circular orbiting halo stars. Moreover, Chiba & Beers (2000) have also presented the average rotation velocity of the stars as a function of the metallicity. They have pointed that the stars with low metallicity as $[\text{Fe}/\text{H}] < -1.7$ show quite low rotation velocity regardless of the value of the metallicity while the rotation velocity increases with increasing the metallicity for the stars of $[\text{Fe}/\text{H}] > -1.7$. The discontinuity suggests that the formation process of the halo part is sharply distinguished from disc part, conflicting the picture of the continuous collapse of the single protogalactic system. Searle & Zinn (1978) have investigated the spatial distribution of GCs with their metal abundance. They have revealed that the color distribution of the HB stars in GCs belong to the outer halo disperses at the given metallicity. The dispersion implies that age of the GCs spread of \sim Gyr, which is inconsistent with the scenario of the single rapid collapse protogalactic system proposed by Eggen et al. (1962). Furthermore, they have argued that there be no spatial gradient for metal abundance. They have considered the existence of sub-galactic component (e.g., dwarf galaxies) that accreted onto the MW. The GCs are thought to be formed along with the infall of such sub-galactic systems before the MW halo came into dynamical equilibrium, and the halo accomplished the dynamical

equilibrium state slowly over time of \sim Gyr. Both the age dispersion of GCs and absence of spatial gradient of abundance can be interpreted by considering such formation picture, though the explanation of the disc formation, discontinuity of the rotation velocity of $[\text{Fe}/\text{H}] = -1.7$ are still lacking. Nevertheless, what should be emphasized here is that we can obtain the clue of the galaxy formation history by investigating features like kinematics, the chemical abundance of GC system.

1.1.2 Dynamical Feature of the Low-mass Dispersion-supported Systems

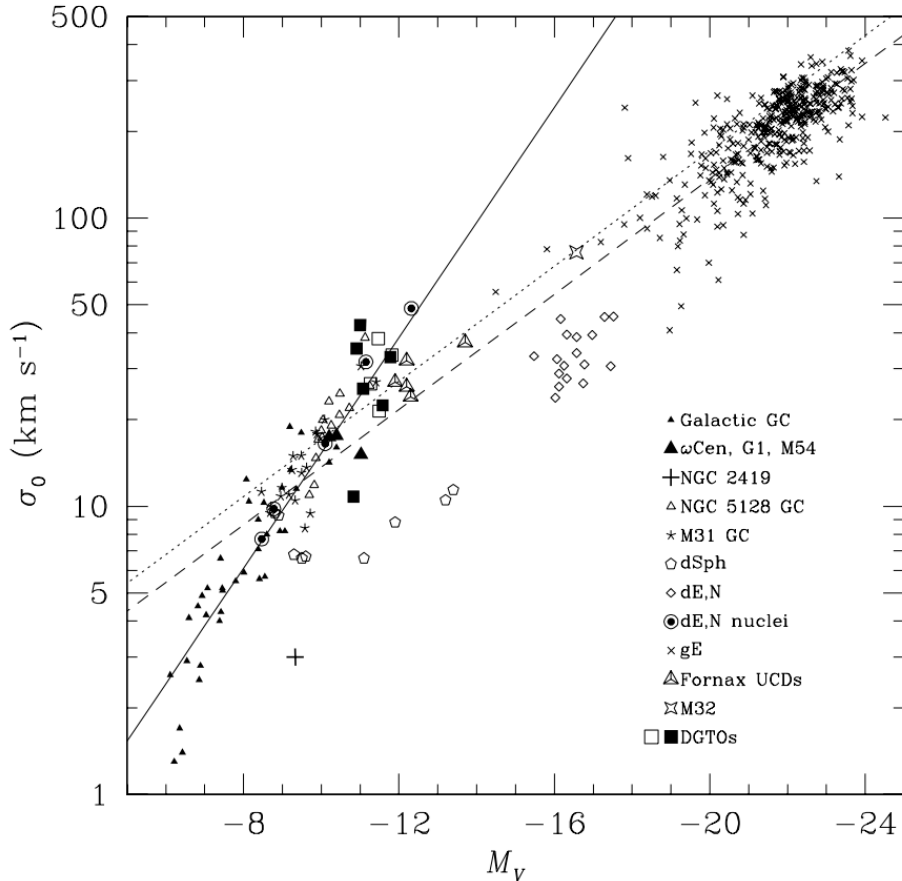


Fig. 1.4: σ - M_V relation taken from Figure 7 of Hasegan et al. (2005). Vertical axis indicates the central velocity dispersion, and horizontal axis indicates the absolute V-band magnitude. Solid line denotes the relation of GCs, $\sigma \propto L^{1/2}$. Dashed, dotted line denotes the Faber-Jackson relation, $\sigma \propto L^{1/4}$ derived by Hasegan et al. (2005), and Drinkwater et al. (2003), respectively.

As we see in the previous section, GCs are the powerful tracer to reveal the galaxy formation. Here, we have to consider the formation process of GC itself. It might be reasonable to suppose that GCs had formed in the early stages of hierarchical cosmology with other protogalactic objects, e.g., dwarf spheroidal galaxies (dSphs), ultra-compact dwarfs (UCDs). These are relatively low-mass dispersion-supported objects, and the luminosity is similar to GCs. However, the internal dynamical property of GCs is sharply different from such dwarf galaxies. According to a virial theorem, velocity dispersion σ relates to gravitational energy as $\sigma^2 \sim GM/r_h$, where G is gravitational constant, M is a dynamical mass of the system, and r_h is half-mass (light) radius, respectively. Besides, luminosity L is thought to be proportion to the stellar mass M_* . That is to say, the relationship between the velocity dispersion and the luminosity (σ - L relation) specifies the

size of the system with respect to the mass. Several observations have revealed that the σ - L relation of GCs is expressed as $\sigma \propto L^{1/2}$ (McLaughlin 2000; Drinkwater et al. 2003; Hasegan et al. 2005; Forbes et al. 2008, see Figure 1.4). On the other hand, the dSphs are the DM dominated, diffuse stellar system. As a result, dSphs lie off GC's σ - L relation. UCDs exhibit low mass-to-light ratio similar to GCs but have slightly higher mass than GCs (Mieske et al. 2008). Tollerud et al. (2011) have studied the behavior of dispersion-supported galaxies in the 'MRL' space (three-dimensional space of dynamical masses, half-light radii, and the luminosities). They have found a best-fitted separation plane that divides GCs from dSphs in MRL space. Furthermore, the plane also divides UCDs from dSphs, and there is no significant separation between UCDs and GCs despite the plane determined without any UCD's information. The fact implies the possibility that UCDs are the same class as GCs. Intriguingly, however, σ - L relation discriminates UCDs from GCs. UCDs are along the lines of the extrapolation of elliptical's Faber-Jackson relation $\sigma \propto L^{1/4}$ (Faber & Jackson 1976) rather than $\sigma \propto L^{1/2}$ of GCs. Figure 1.5 shows the half-light radius r_h vs. absolute V-band magnitude M_V of GCs and dwarf galaxies belong to Local Group. We see in the figure that the r_h

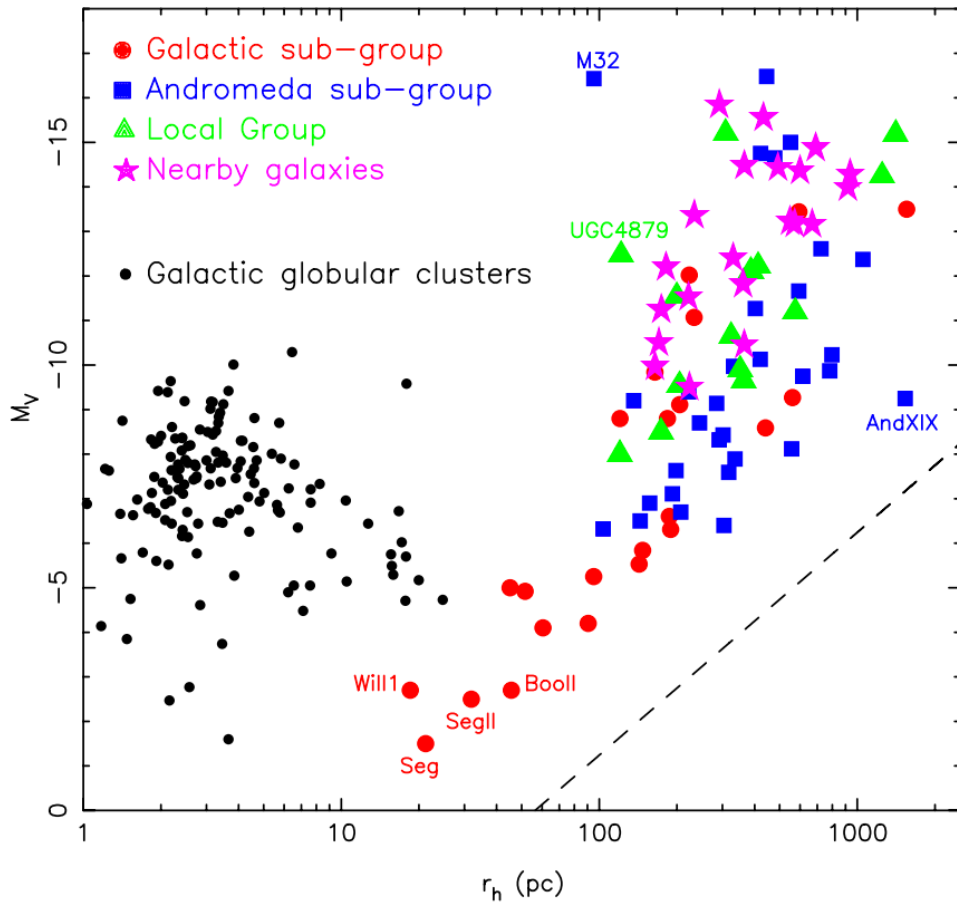


Fig. 1.5: Half-light radius as a function of absolute V-band magnitude M_V , taken from Figure 6 of McConnachie (2012). Black dots represent GCs, and other colored points represent the galaxy samples as summarized in the key.

of GCs exhibit $\lesssim 10$ pc regardless of M_V and are quite small compared to other galaxies that have similar M_V . Note that, the OCs are also separated from the GCs regarding the dynamical feature, since the OCs are diffuse, loosely bounded star clusters. The compactness is the unusual property that divides the GCs with other velocity-supported low-mass stellar systems, hence, implies any particular formation mechanism.

1.2 Formation of Star Clusters in Ultraviolet Background Radiation Fields

1.2.1 Theoretical Predictions for Globular Cluster Formation

Theoretically, the several scenarios of old GC formation have been proposed but still controversial.

Saitoh et al. (2009) have performed N -body/SPH simulation to investigate the evolution of interacting two disc galaxies. They have presented that large-scale high-dense region in the colliding interface forms due to shock compression. As a result, the formation of star clusters mass range of $\sim 10^6\text{--}10^8 M_\odot$ is triggered (Saitoh et al. 2011, Figure 1.6). The "shock-induced star formation" is in good agreement with present-day star cluster formation in Antennae (Whitmore & Schweizer 1995; Whitmore et al. 1999). However, this may be appropriate to a star cluster formation in the later phase of hierarchical merging rather than an early stage of host galaxy formation.

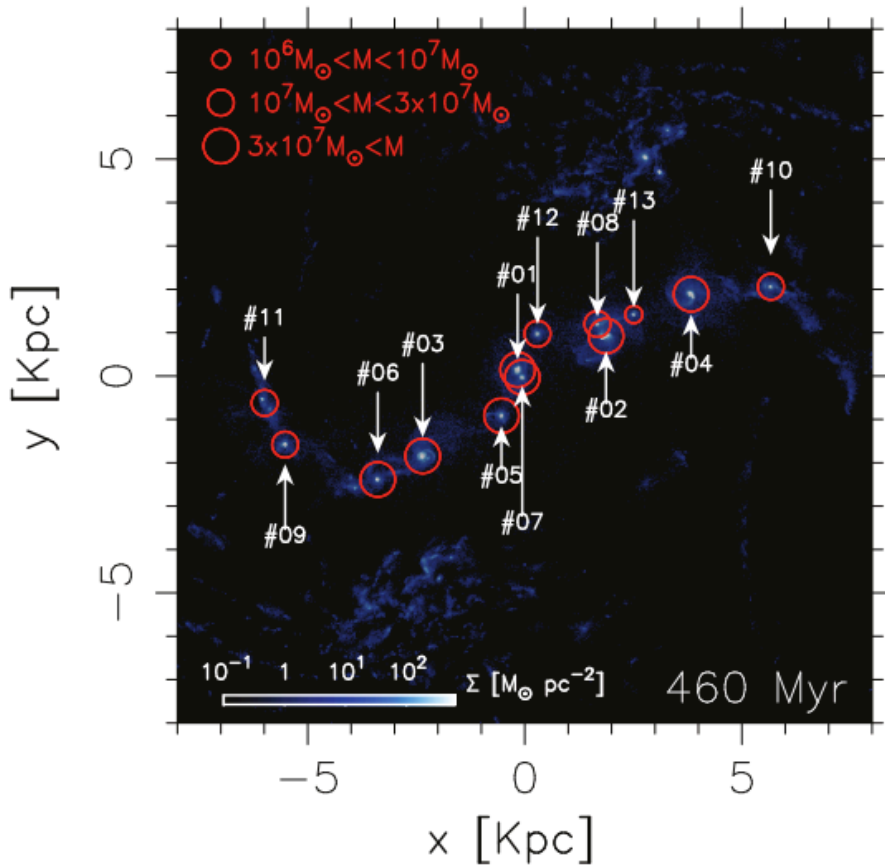


Fig. 1.6: Shock-induced star formation, taken from Figure 6 of Saitoh et al. (2011). Circle indicates the position of the star clusters formed via shock-induced star formation, and the radius expresses the mass of the star cluster as represented in the key.

Kravtsov & Gnedin (2005) have performed high-resolution cosmological simulation and investigated the formation of GCs in Milky Way size galaxy. They have found that the cold metal-poor gas can be delivered to the center of the galaxy by both mergings of smaller galaxies and direct accretion of gas along the dark matter (DM) filament. The interaction of gas induces density fluctuation and generate the separate molecular cloud that would be able to evolve to GCs (Figure 1.7). Their result suggests that the GCs naturally form in the host galaxy in Λ CDM cosmology. Recently, Harris et al. (2013, 2015) have studied the

relationship between the galaxy halo mass and the total mass of GC belong to the host galaxy. They have argued that the total mass of GC system proportion to the mass of host galaxy halo. The relationship is valid over five orders of magnitude and regardless of morphological types of the host galaxy. They have also pointed that the numerical model of Kravtsov & Gnedin (2005) can represent the observation. However, it should be mentioned that the simulations could not resolve the structure of each cluster. Also, their simulation predicts the GC formation in the dense gaseous disc at high- z and they have not considered the present-day spatial distribution.

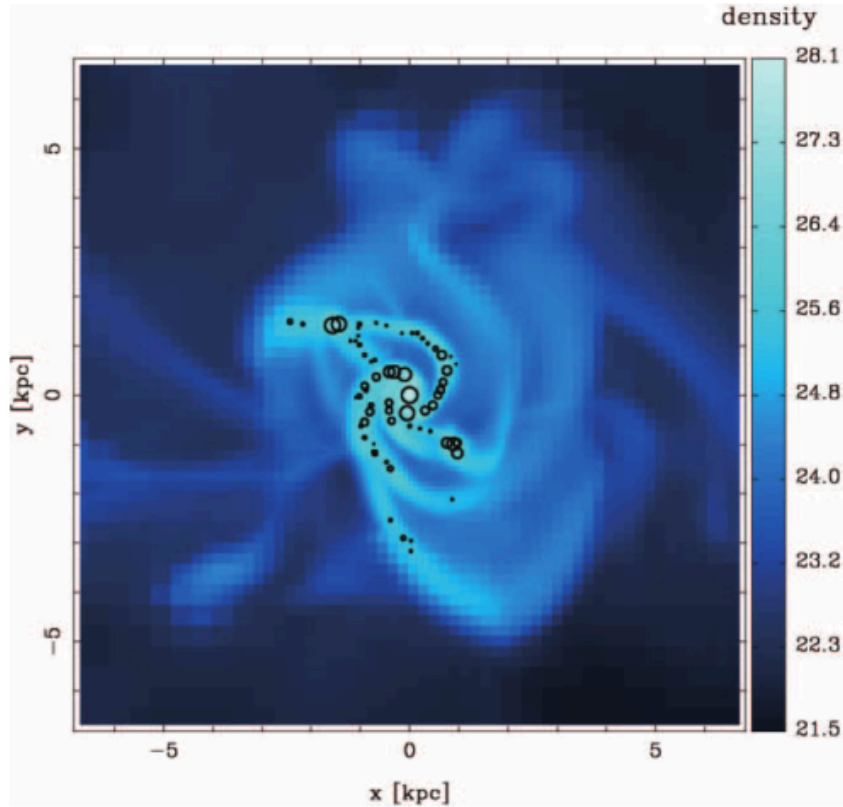


Fig. 1.7: Star cluster formation in the disc of the host galaxy, taken from Figure 1 of Kravtsov & Gnedin (2005). Color indicates the density of the gas. Circle represents the position of the dense gas component, which would evolve to GC.

On the other hand, several studies have presented the plausible argument that GC formation would take place in primordial DM subhalo. Diemand et al. (2005) and Moore et al. (2006) have performed high-resolution cosmological pure N -body simulation. They have revealed that the radial distribution of subhalos that constitute the present day MW sized DM halo depend on the rarity of the peak of the density fluctuation, more rare peaks, the more concentrate on the present day halo. The distribution only depends on the rarity but not on the subhalo mass or redshift z . They have mentioned that the $> 2.5\sigma$ peaks of the overdensity fluctuation resemble the Galactic GCs (Figure 1.8). They have also represented that the mass fraction of such high- σ peak roughly independent of halo mass. This tendency is qualitatively consistent with the observation of Harris et al. (2013, 2015). These works suggest the scenario of GC formation originates in low-mass DM subhalos at an early universe while GCs are the DM-free stellar system. Saitoh et al. (2006) have performed N -body/SPH simulations to explore the GC formation in DM subhalo in a standard CDM cosmology framework. They have demonstrated that tidal force from the host galaxy effectively works, and outer DM halo can be stripped away while the central stellar system remains. Thus, a

stellar dominated system can form even if the system was embedded in DM halo at one time. Interestingly, recent observation of Taylor et al. (2015) has presented the sequence of compact stellar systems that exhibit half-light radii similar to GCs but higher mass-to-light ratio order of ~ 10 in the solar unit. Although the origin is uncertain, they have discussed that the one of the possible implication of such dark sequence is DM halos. Hence, the GC formation originated in DM subhalo at the high- z universe is also a reasonable scenario.

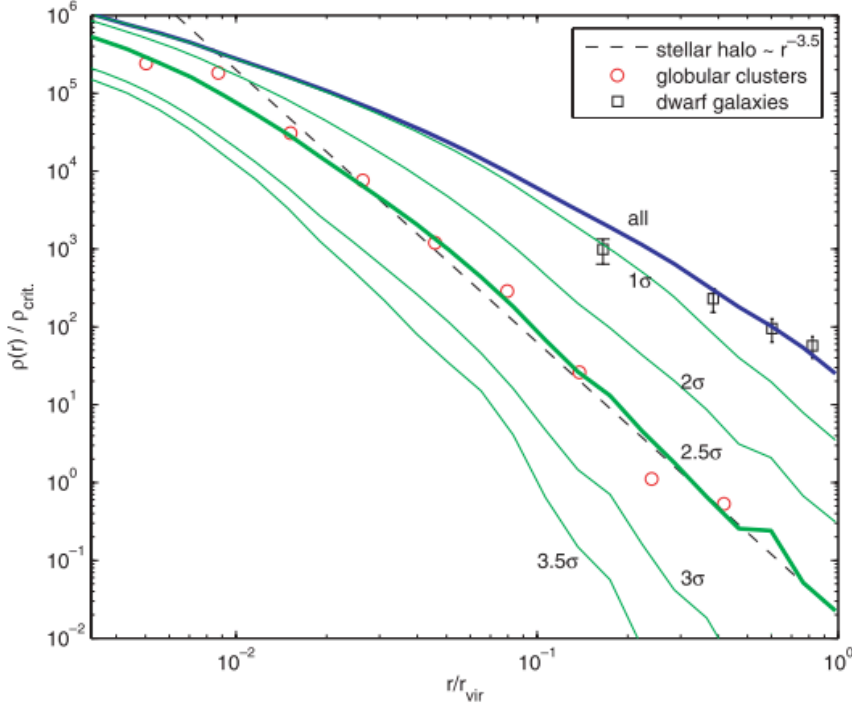


Fig. 1.8: Radial distribution of the high- σ overdensity peak, taken from Figure 2 of Moore et al. (2006). Green lines indicate the present-day distribution of the overdensity peaks of any given σ , as denoted in the figure.

Although several GC formation scenario have been proposed in theoretical works as described above, it is necessary to keep in mind that such simulations cover as large, galaxy-scale hence they cannot pursue the internal motion of star clusters due to numerical resolution. The numerical simulation in more small, i.e., sub-galactic scale is required to argue the formation process of GCs. Then, the compactness of GCs would be the key to revealing the scenario for GC formation.

1.2.2 Prospect of Ultraviolet Background Radiation at an Early Universe

According to cosmic reionization, the existence of strong UV background radiation field would be one of the most important consideration for formation process for ancient sub-galactic objects.

So-called Gunn-Peterson effect has obtained one of the most strong evidence for a cosmic reionization. If the high- z distant luminous sources, e.g., quasars are supposed, the spectrum would be absorbed owing to the rest-frame resonant absorption, e.g., Ly α absorption by the neutral hydrogen in the intergalactic medium (IGM). The evolution of ionization state of IGM can be constrained by the observation of the Gunn-Peterson effects. Fan et al. (2006) have investigated the Ly α absorption line of the high- z quasar to estimate the fraction of neutral hydrogen as a function of z . They have revealed that the fraction of neutral

hydrogen drastically changes around $z \sim 6$, thereby constraining the epoch of reionization (EoR) as $z_r \gtrsim 6$ (Figure 1.9).

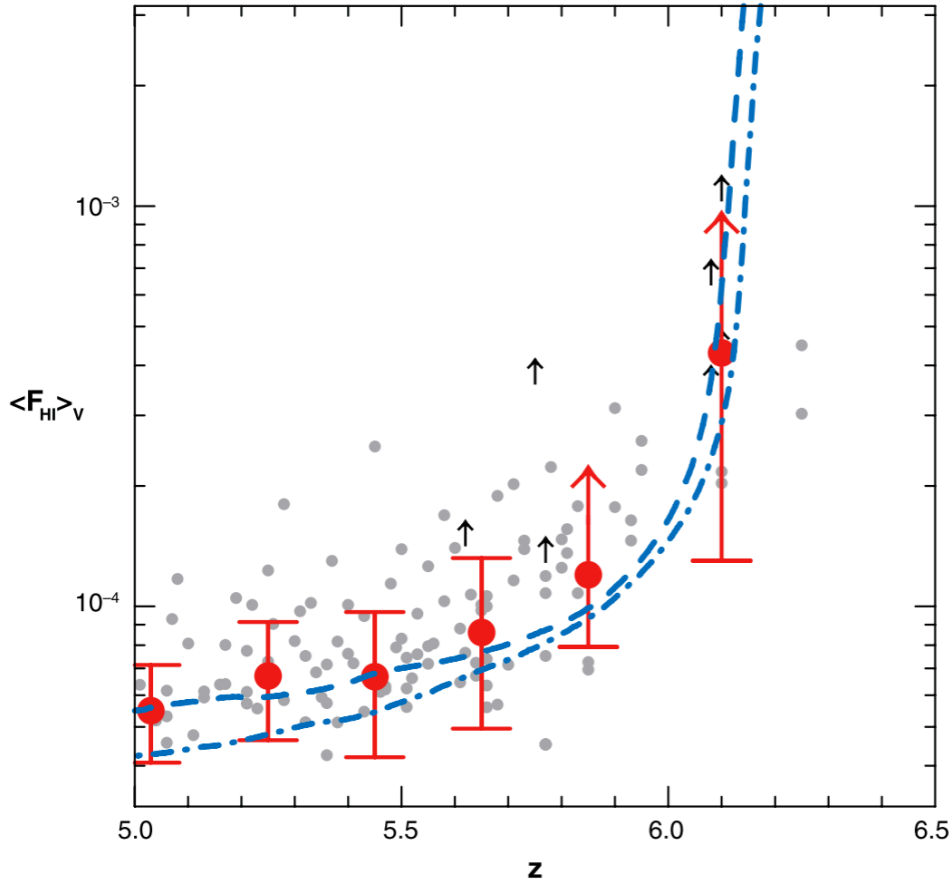


Fig. 1.9: Volume-averaged hydrogen neutral fraction in IGM, taken from Figure 6 of Fan et al. (2006). Red point with error bar represents the measurement based on the observation. Dashed, and dashed-dotted-dashed line indicates the result of the numerical simulation.

On the other hands, Gamma-Ray Burst (GRB) is also a powerful tool to probe the high- z universe owing to its cosmological origin and the luminosity. Totani et al. (2006) have investigated the optical afterglow spectrum of the GRB050904 at redshift $z = 6.3$. They have performed χ^2 fitting for $\text{Ly}\alpha$ damping wing profile in the spectrum and showed that the considerable amount of intergalactic medium (IGM) hydrogen seems to be ionized at $z = 6.3$, the best-fitted neutral fraction of IGM is 0.0, and an upper limit of the fraction is 0.6 with 95 % confidence level.

Moreover, recent observations have revealed the evolution of a luminosity function for high- z $\text{Ly}\alpha$ emitters (LAEs). Ouchi et al. (2010) have found the decrease of the LAE luminosity functions at $z = 6.6$ compared to $z = 5.5$. Although it may be caused by not only IGM neutral hydrogen absorption but also intrinsic galaxy evolution, they have argued that a large number of IGM hydrogens may be not highly neutral and constrained the neutral hydrogen fraction as < 0.2 at $z = 6.6$, thus, the reionization may take place at $\gtrsim 7$.

The optical depth for Thomson scattering of the free electrons has been derived from the polarization of cosmic microwave background (CMB) observation. Since the optical depth is proportional to the integration of electron column density at z , the EoR can be predicted. Hinshaw et al. (2013) have estimated the optical depth for Thomson scattering from the data of nine-year *Wilkinson Microwave Anisotropy Probe* (WMAP) and derived that the reionization may take place at $z_r \sim 10.6$, assuming the instantaneous reionization.

Thus, it is reasonable to suppose that the most of the old GCs formed via strong UV background radiation field.

1.2.3 Physical Model

The gas cloud embedded in the UV background radiation field is photoionized, and the temperature rises to $\sim 10^4$ K. Then, the contraction of the cloud is prevented due to its thermal pressure unless the total mass of cloud is higher than Jeans mass of $\sim 10^4$ K. Moreover, UV photons destroy the hydrogen molecules and catalysts for H_2 formation (H^- , H_2^+). Thus, the gas cloud should be self-shielded against UV photon to form a low-mass sub-galactic object. Tajiri & Umemura (1998) have performed spherically symmetric frequency-dependent radiative transfer calculation coupled with the ionization process. They have assumed the power-law UV background radiation intensity $I_\nu = 10^{-21} \times I_{21} (\nu/\nu_L)^{-1} \text{ erg cm}^{-2} \text{ s}^{-1} \text{ str}^{-1} \text{ Hz}^{-1}$ (ν_L denotes the Lyman limit frequency) and revealed that the critical number density n_{crit} required to self-shield against the background radiation field is given by

$$n_{\text{crit}} = 1.40 \times 10^{-2} \text{ cm}^{-3} \left(\frac{M}{10^8 M_\odot} \right)^{-1/5} I_{21}^{3/5} \quad (1.1)$$

or corresponding critical radius is

$$r_{\text{crit}} = 4.10 \text{ kpc} \left(\frac{M}{10^8 M_\odot} \right)^{2/5} I_{21}^{-1/5} \quad (1.2)$$

where M is the total mass of the cloud. If the density of the cloud exceeds the critical density, the cloud can shield the external UV photons at the radius of r_{shield} (quantitative estimation is described in chapter 2). In other words, r_{shield} is zero unless the gas cloud satisfies the above condition.

Since the self-shielded region ($r < r_{\text{shield}}$) never be photoionized and photoheated, the gas interior of the area can contract by self-gravity even though the mass $M(< r_{\text{shield}})$ is less than $M_J(10^4\text{K})$. Eventually, the cloud can effectively form the hydrogen molecules, and cooled down to several 100 K due to hydrogen molecular cooling. Then, the gas can collapse to form stars if the gas of mass $M(< r_{\text{shield}})$ is more massive than the Jeans mass of 100 K.

We need to treat such physical processes, i.e., hydrodynamics of baryon, non-equilibrium chemical reaction, and self-shielding effect with radiative transfer consistently to consider the formation of the sub-galactic system under UV background radiation. Then, the hydrodynamics coupled with the radiative transfer; radiation-hydrodynamics (RHD) calculation is required. For instance, Susa & Umemura (2004) have performed three-dimensional radiation hydrodynamical simulation to handle self-shielding effect accurately and investigated the formation of dwarf galaxies at the cosmic reionization epoch. They have found that UV background radiation suppresses the star formation. However, baryons belong to high-density peak can collapse and evolve to dwarf galaxy by virtue of self-shielding effect. They have mentioned that the final stellar fraction of dwarf depends on the collapse epoch, the mass of density peaks. Their study indicates the importance of UV background radiation that controls the character of final stellar objects.

Hasegawa et al. (2009) have performed spherically symmetric radiation hydrodynamical simulation to investigate the formation process of low-mass (initial baryonic mass of $10^{6-8} M_\odot$) sub-galactic objects under UV background radiation field. As a result, they have found that the UV background radiation separates the star cluster formation path into three types as a function of initial baryonic mass, intensity of background UV photons, epoch of irradiation. The qualitative explanation for each formation branch is described as follows.

prompt star formation

In the case when the cloud of the mass M is $M_J(100\text{K}) < M < M_J(10^4\text{K})$. If the UV intensity is relatively weak, the self-shielded region immediately forms. Then, the stars promptly begin to form in the gas interior of the self-shielded region while the outer region conversely evaporates by photoheating. This formation branch is named *prompt star formation*. The prompt star formation is accepted branch concerning the low-mass galaxy formation in the epoch of reionization (e.g., Susa & Umemura 2004).

In this case, star formation occurs at an early epoch of contraction. Hence, gas components are effectively converted to collisionless stellar components when the kinetic energy dissipation of contracting gas is relatively weak. As a result, diffuse systems tend to be formed. The resultant star clusters distribute similar to dSphs in the σ - M_V plane.

delayed star formation

In the case when the mass of the cloud exceeds the Jeans mass of 10^4 K; $M > M_J(10^4\text{K})$. When the cloud is exposed to the strong UV background radiation, r_{shield} to be much smaller, the bulk of the cloud is photoionized and photoheated. However, even the outer part of the self-shielded region ($r > r_{\text{shield}}$) can also contract since the gravitational energy exceeds the thermal pressure of the photoionized gas. Eventually, cloud radius shrinks less than r_{shield} and stars begin to form. The bulk of the cloud photoionized on at least one occasion, which induces the delay the star formation. Therefore, this scenario is named as *delayed star formation*.

In this case, the gas cloud can collapse whether the bulk of cloud is photoionized or not. Therefore, contraction is decelerated due to the thermal pressure but not sufficient. As a result, the objects formed via delayed star formation cannot exhibit the high velocity dispersion with respect to the mass of the cluster. Consequently, the σ - L relation tends to deviate from the GCs.

supersonic infall

Finally, we consider the cloud of the mass of $M_J(100\text{K}) < M < M_J(10^4\text{K})$ with the strong UV background radiation. In the case, r_{crit} is sufficiently small compared to the cloud radius. Apparently, the cloud never contract but evaporate because the self-gravity is much lower than ionized thermal pressure. However, if the strong UV background is to be effective when the later phase of contraction, the infall velocity exceeds the sound speed of 10^4 K, the cloud can continue to contract. Eventually, the cloud sufficiently contracts ($r < r_{\text{crit}}$) and stars begin to form. This branch is *supersonic infall*, newly propounded by Hasegawa et al. (2009). In this scenario, self-shielding region r_{shield} can be more compact due to the intense UV radiation. Hence, the star forming region is compact. In addition, the infall velocity is strongly decelerated due to adiabatic heating of 10^4 K. As a result, the size of the star cluster formed via supersonic infall tends to be compact.

The conceptual figure for the three models appears in Figure 1.10.

Figure 1.11 shows the stellar σ - M_V relation simulated by Hasegawa et al. (2009). Figure 1.11 indicates that each branch systematically separates the distribution of star clusters in the σ - M_V plane. Star clusters formed via supersonic infall exhibit a steep relationship between the velocity dispersion and the luminosity (mass) compared to star clusters formed through other two branches. Moreover, they have also mentioned that the half-mass radii formed via supersonic infall systematically $\lesssim 10$ pc regardless of stellar mass. The features are in good agreement with observed GCs. Hasegawa et al. (2009) have argued that the steep σ - L relation of GCs can only be reproduced by star clusters formed through supersonically infalling photoionized gas.

1.3 Purpose of This Study

The supersonic infall seems to be a good physical model to explain the compactness of GCs. However, it is notable that there are some effects of radiative transfer in three-dimensions that would have to be taken into account in the simulations. First, it is expected that the background radiation field in the more realistic (general) situation is thought to be anisotropic. In an anisotropic background radiation field, the self-shielding region is also anisotropic. Thus, the contraction process of the cloud may be affected by the anisotropy of background radiation. Furthermore, the self-shielding effect is also affected by an inhomogeneous density field of the gas. For instance, Nakamoto et al. (2001) have calculated six-dimensional radiative transfer to explore the photon propagation during the reionization in an inhomogeneous universe. They have shown that the photoionizing process in an inhomogeneous media is delayed compared to homogeneous one, because of local shadowing effect come from three-dimensional inhomogeneity of density field. In the case of the non-uniform medium, the shielding condition is proportion to root-mean-square of the density (Madau et al. 1999).

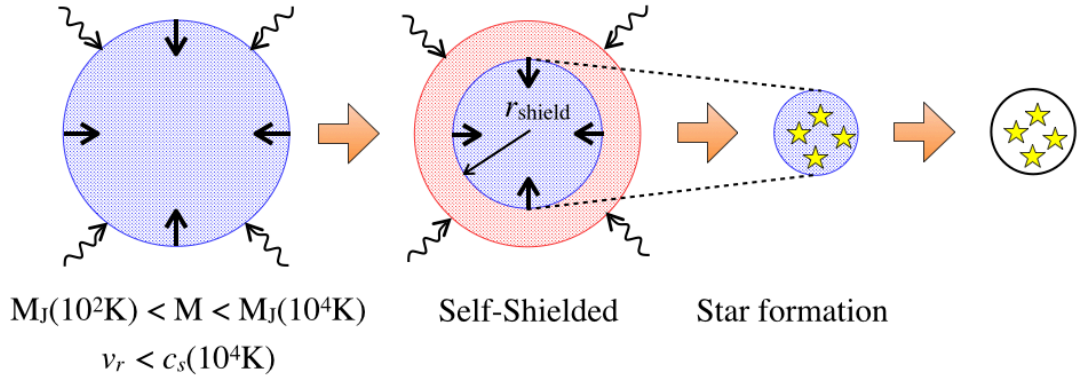
Thus, if we suppose more general situation and correctly take into account such radiative transfer effect upon the star cluster formation, it is possible that the resultant star cluster behaves in different ways from one-dimensional previous works. It should be considered how is self-shielding affected by the anisotropy of background radiation field and the three-dimensional density structure of the cloud.

In this study, three-dimensional radiation hydrodynamical simulations are performed to investigate the star cluster formation exposed to an anisotropic UV background radiation field. Our goal is set out to construct a more progressive, realistic physical model of star cluster formation, and we reconsider a possibility of GC formation under UV background radiation field in the standard cosmological framework.

This thesis is organized as follows. In Chapter 2, the basic physics, numerical method, and our numerical model are described. The numerical results including the contraction of the cloud, stellar dynamics, and comparison with the observations are presented in Chapter 3. Chapter 4 is devoted to the discussions based on our numerical results. Finally, we summarize our study in Chapter 5.

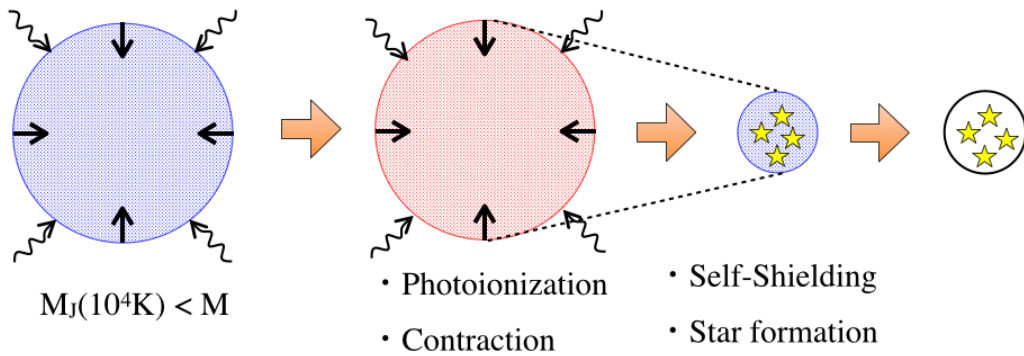
Prompt star formation

UV radiation (Weak intensity)



Delayed star formation

UV radiation (Strong intensity)



Supersonic infall

UV radiation (Strong intensity)

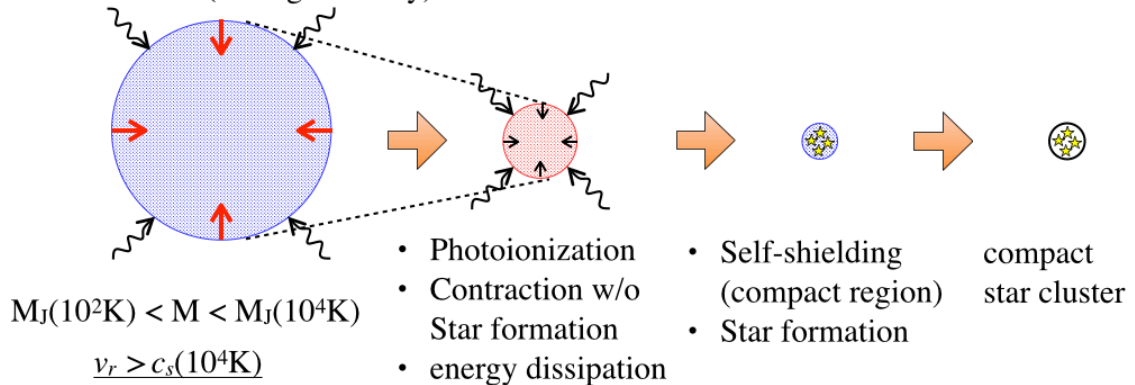


Fig. 1.10: Conceptual figure for the physical models of star cluster formation proposed by Hasegawa et al. (2009). Upper, middle, bottom represent the *prompt star formation*, *delayed star formation*, and *supersonic infall*, respectively (see the text). In each panel, red-shaded region and blue-shaded region indicate the photoionized area and self-shielded area. Arrow indicates the infall velocity vectors.

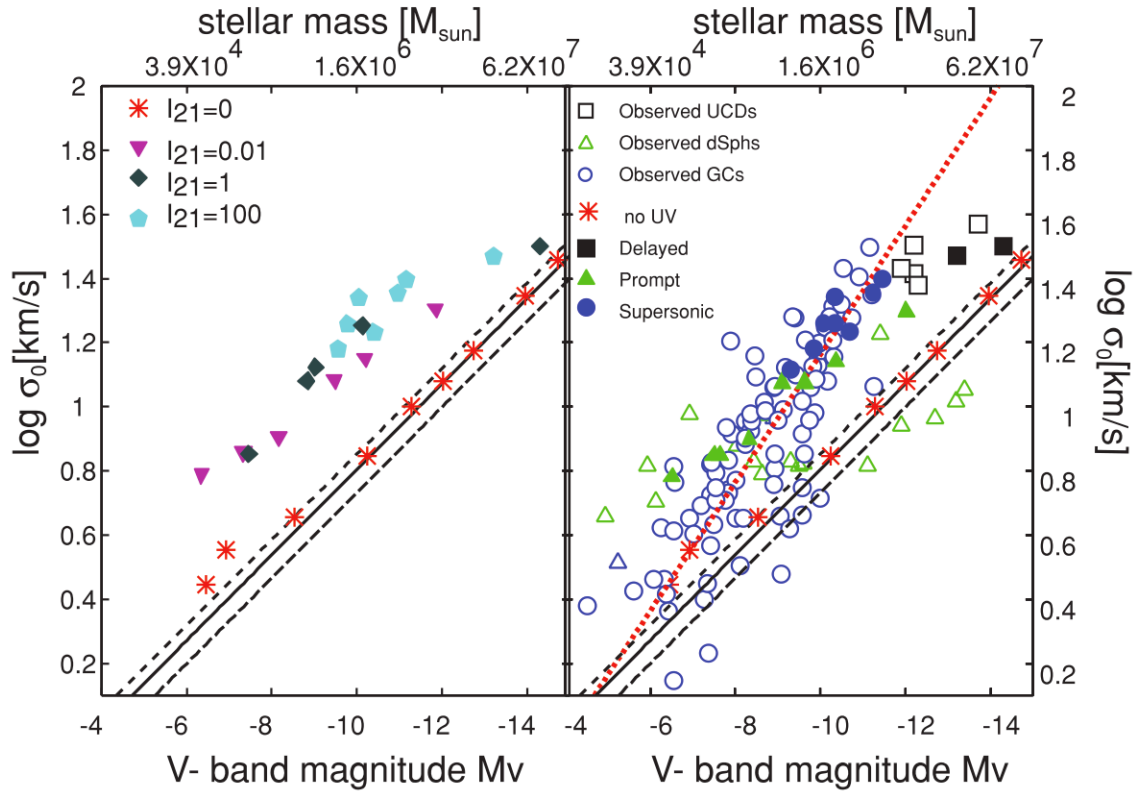


Fig. 1.11: $\sigma-M_V$ relation obtained by the spherically symmetric RHD simulations, taken from Figure 9 of Hasegawa et al. (2009). In the right-hand panel, filled symbols represent the star clusters formed via prompt star formation (green triangle), delayed star formation (black square), and supersonic infall (blue circle), respectively. Observation for dSphs, UCDs, and GCs are overplotted. Left-hand panel represents the dependency on the UV background intensity.

Chapter 2 Numerical Method & Model Description

2.1 Basic Physics

2.1.1 Gravitational Contraction & Thermal Evolution

In most astronomical situations including star cluster formation, the fluid approximation for gas dynamics is adaptive because the mean-free-path of the components of gas (i.e., atoms and/or molecules) is much smaller than typical scale length of the system. The gas cloud contract with self-gravity but restoring force due to its thermal pressure also works with contraction. According to Jeans analysis, a critical mass that can induce the gravitational instability, Jeans mass M_J is given by

$$M_J = \frac{\pi}{6} \left(\frac{\pi}{G\rho} \right)^{3/2} c_s \rho \propto T^{3/2} \rho^{-1/2} \quad (2.1)$$

where G , ρ , T , c_s are gravitational constant, mass density, temperature, sound speed of the gas cloud, respectively. If we assume ideal gas, c_s can be described as $\sqrt{\gamma k_B T / \mu}$ where γ , k_B , μ are specific heat ratio, Boltzmann constant, mean molecular weight, respectively. This condition suggests that sufficient mass is needed with increasing temperature because the thermal pressure (internal energy) becomes to be non-negligible relative to gravitational energy. Let us look at this condition from a different angle. The timescale of gravitational collapse is roughly given by a free-fall timescale $t_{\text{ff}} = \sqrt{3\pi/32G\rho}$. On the other hand, the perturbation of fluid propagates with sound speed c_s hence crossing time $t_{\text{cross}} = L/c_s$ is the time scale that restoring force effectively works, where L is the typical scale of the system. Since $t_{\text{ff}} < t_{\text{cross}}$ is a condition for gravitational collapse, we can also obtain the required mass as $M \sim L^3 \rho \propto c_s^3 \rho^{-1/2} \propto T^{3/2} \rho^{-1/2}$ which is similar to the result of Jeans analysis (equation 2.1).

If the initial mass of the cloud M_{ini} satisfies the condition $M_{\text{ini}} > M_J$, the cloud begins to contract adiabatically. Simultaneously the temperature increase with increasing the density; hence M_J is also increase and contraction would be eventually stopped. Thus, in addition to initial gravitational instability, gas cloud needs to transfer heat from cloud to outer region by the cooling process and prevent Jeans mass from increasing. At an early universe, there is few abundance of metal. In the case of atomic cooling for $[\text{Fe}/\text{H}] \leq -3.0$ gas, thermal energy escape from gas cloud due to line cooling, recombination cooling, collisional ionization cooling, bremsstrahlung radiation, inverse-Compton scattering of H and He. However, the atomic cooling is inefficient at $T \gtrsim 10^4$ K. The most significant cooling process at $T \lesssim 10^4$ K is the vibrational-rotational transition of H_2 molecule that can cool the gas temperature down to ~ 100 K. Since the hydrogen molecular has no electric dipole moment, the formation process via the collision of two hydrogen atoms is forbidden. When the system is low-density gas, H_2 molecules are effectively formed via H^- -process



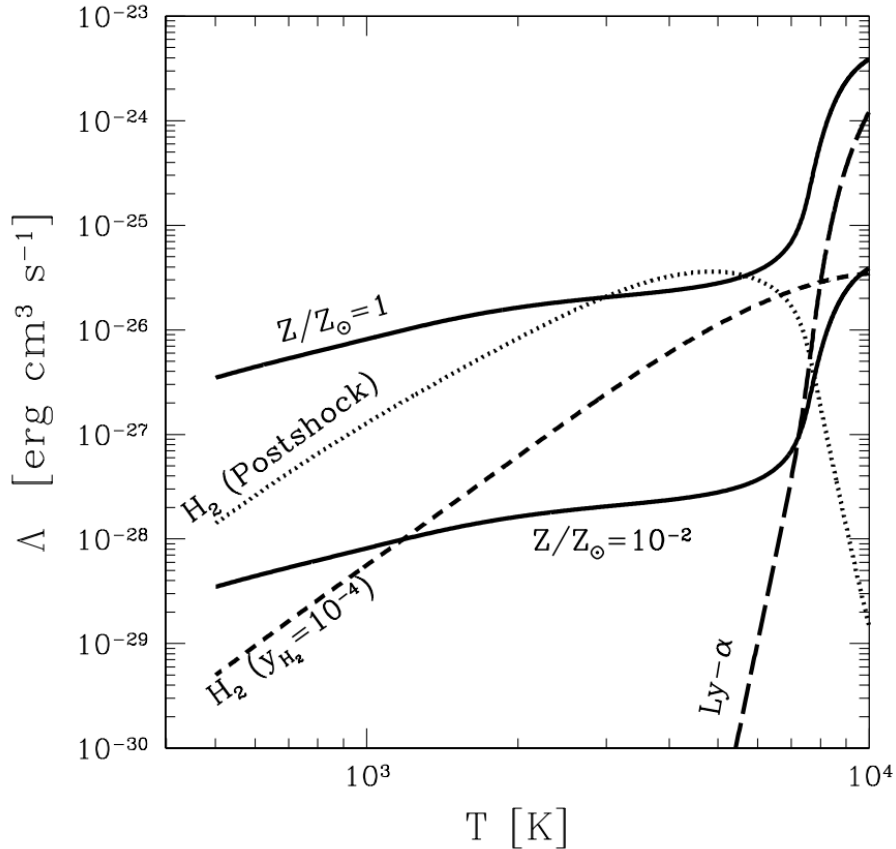


Fig. 2.1: Cooling function, taken from Figure 2 of Susa & Umemura (2004). The vertical axis indicates the cooling rate λ , and the horizontal axis is the temperature T , respectively. Dotted line represents the H_2 cooling. Solid lines denote the cooling due to metal. The metallicity is assumed as $Z/Z_\odot = 1, 10^{-2}$ as presented in the figure.

and H_2^+ -process



As a result, the cloud can continue to contract with decreasing its Jeans mass. Note that, the cooling rate of H_2 is not essentially efficient while the most important coolant at an early universe. If some metals were also taken into account, cooling due to carbon would be important at $T \lesssim 10^4$ K. Figure 2.1 show the comparison of H_2 cooling function with metal cooling. As we see in the figure, H_2 cooling is still dominant in the temperature range of $10^3 - 10^4$ K unless the metallicity is 0.01 of the solar abundance Z_\odot .

Finally, the thermal evolution of the gas obtained by Omukai et al. (2005) is shown in Figure 2.2. Initially gravitationally unstable gas cloud adiabatically contracts to $\sim 1\text{cm}^{-3}$ with increasing temperature. When the temperature come up to $\sim 10^3$ K, H_2 molecules are effectively formed, and the cloud can continue to contract by virtue of cooling. When the gas density is relatively low, the energy transition in the upward direction is dominated by collisional excitation and downward is dominated by spontaneous emission. Then,

equilibrium of transition can be described as

$$\begin{aligned} \sum_{i \geq 2} \sum_{j < i} n_e n_j C_{ji} &= \sum_{i \geq 2} \sum_{j < i} n_i A_{ij} + \sum_{i \geq 2} \sum_{j < i} n_e n_i C_{ij} \\ &\sim \sum_{i \geq 2} \sum_{j < i} n_i A_{ij} \end{aligned} \quad (2.4)$$

where A , C , n_i , n_e are Einstein A coefficient, collisional coefficient, the number density of i -th energy state, electron number density, respectively. The second formula is obtained by assuming the condition of low-density gas thereby $n_i A_{ij} > n_e n_i C_{ij}$. A cooling function of H_2 , Λ_{H_2} , radiative energy emitted per unit time is described as

$$\Lambda_{\text{H}_2} = \sum_{i \geq 2} \sum_{j < i} n_i A_{ij} h\nu_{ij} = \sum_{i \geq 2} \sum_{j < i} n_e n_j C_{ji} h\nu_{ij} \quad (2.5)$$

where h is Planck constant, and $h\nu_{ij}$ is corresponding to an energy difference between two levels of i -th and j -th. At this phase, the cooling efficiency is proportion to a square of gas number density n and gas temperature decreases due to the emission line of H_2 . However, the relationship of $n_i A_{ij} < n_e n_i C_{ij}$ would come to be satisfied with increased amount of density and collisional de-excitation to be dominated. At this time,

$$\sum_{i \geq 2} \sum_{j < i} n_e n_j C_{ji} = \sum_{i \geq 2} \sum_{j < i} n_e n_i C_{ij} \quad (2.6)$$

and the energy states are determined by local temperature

$$\frac{n_i}{n_j} = \frac{g_i}{g_j} \exp[h\nu_{ij}/k_B T] \quad (j > i) \quad (2.7)$$

where g_i is degeneracy factor. That is to say, the gas consists of the Local Thermodynamics Equilibrium (LTE). As a result, a cooling function is described as

$$\Lambda_{\text{H}_2} = \sum_{i \geq 2} \sum_{j < i} n_i A_{ij} h\nu_{ij} \quad (2.8)$$

Hence cooling efficiency becomes to be proportion to n with increasing the number density. This fact indicates that the decreasing of cooling efficiency with density evolution. The turn-off number density is the critical density n_c , located at $\sim 10^4 \text{cm}^{-3}$ in the case of primordial gas. Decreasing of cooling efficiency induces the fragmentation of gas cloud into a scale corresponding to Jeans mass of n_c , which corresponds to the typical mass of molecular cloud "core". Since the critical density are determined by the Einstein A coefficient and collisional coefficient, n_c depends on the metallicity.

2.1.2 Description of Radiative Feedback and Radiative Transfer

As described above, H_2 is the most important coolant for star cluster formation at an early universe. However, the catalysts for H_2 formation are destroyed by UV radiation such as



Note that, the hydrogen molecules can also be formed without catalysts through the three-body reaction as



while the three-body reaction is not to be effective unless the gas density exceeds $\sim 10^8 \text{cm}^{-3}$, hence it is not crucial to the early phase of star cluster formation.

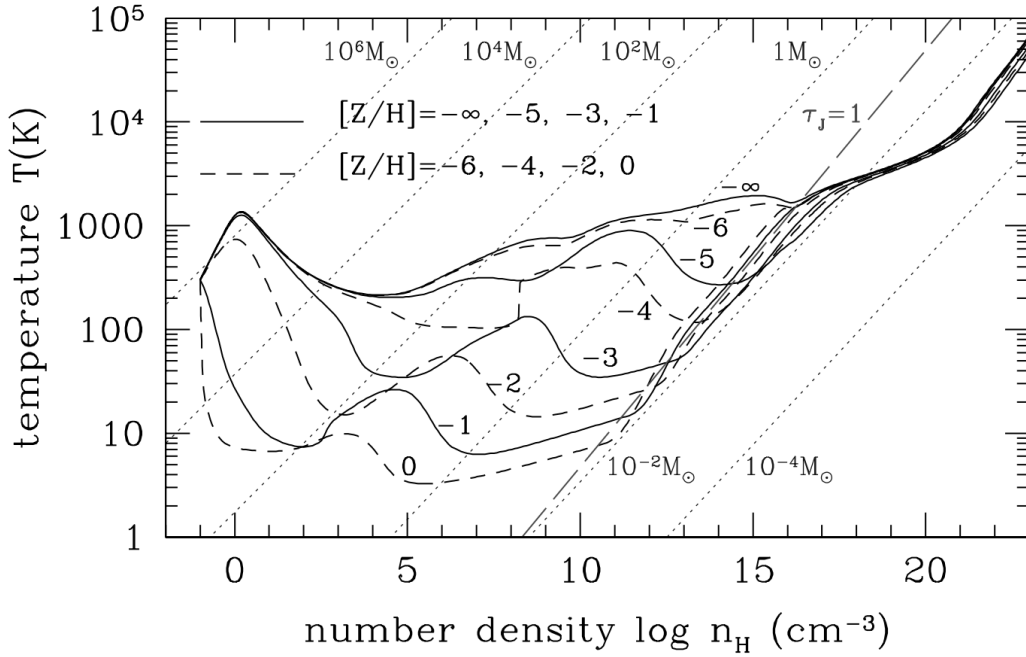


Fig. 2.2: Thermal evolution of the gas with different metallicity (as presented in the figure), taken from Omukai et al. (2005). The vertical axis indicates the temperature, and the horizontal axis is the number density of the gas, respectively. The straight dotted line indicates the corresponding Jeans mass.

Furthermore, H_2 can be directly photodissociated by Lyman-Werner band photons due to the Solomon-process, 85% of states populate vibrational-rotational level but 15% of excited states decay to the continuum thereby



Moreover, UV photon that has a frequency higher than Lyman-limit frequency ν_L , i.e., $h\nu > h\nu_L = 13.6\text{eV}$ can photoionize the hydrogen atoms



The photoionizing is a heating process since the surplus energy of ionizing is imposed on the kinetic energy of free-electron. The typical temperature of the photoionized/photoheated gas is $\sim 10^4$ K. Therefore, such processes act in the direction of preventing the formation of star cluster because of an increasing of temperature induce the larger Jeans mass and gravitational contraction would be suppressed. Note that, the impact of photoionization is not only negative but also positive. An electron produced via photoionization also be used in H^- -process (see equation 2.2). Thus, H_2 formation would be promoted.

As just described, the effect of UV radiation is complex, considerable for dynamical evolution of gas cloud. It is needed to solve the radiation transfer equation to take into account such radiative feedback correctly.

A radiative energy pass through the surface dA in the direction of solid angle $d\Omega$ in frequency $d\nu$ in time dt is defined by $I_\nu dA dt d\nu d\Omega$, where I_ν [$\text{erg cm}^{-2} \text{sec}^{-1} \text{sr}^{-1}$] is specific the intensity of radiation. Radiative transfer equation is described as loss and gain of the intensity I_ν as it travels a distance ds along with the ray

$$\frac{dI_\nu}{ds} = -\kappa_\nu I_\nu + j_\nu \quad (2.15)$$

where κ_ν and j_ν are absorption coefficient and emission coefficient, respectively. The absorption coefficient is a product of number density of media n and cross-section σ_ν

$$\kappa_\nu = n\sigma_\nu \quad (2.16)$$

The formal solution of equation (2.15) can be obtained as follows. The optical depth τ_ν is defined as

$$\tau_\nu = \int_{s_0}^s ds' \kappa_\nu(s') \quad (2.17)$$

Note that, the unity of the optical depth is corresponding to a mean-free-path l_ν of photons because of $l_\nu = 1/n\sigma_\nu$.

Then, the radiation transfer equation can be rewritten to τ_ν instead of ds as

$$\frac{dI_\nu}{d\tau_\nu} = -I_\nu + S_\nu \quad (2.18)$$

where $S_\nu = j_\nu/\kappa_\nu$ is the source function. Now define the new quantities $\tilde{I}_\nu \equiv I_\nu e^{\tau_\nu}$, $\tilde{S}_\nu \equiv S_\nu e^{\tau_\nu}$ and equation (2.18) becomes

$$\frac{d\tilde{I}_\nu}{d\tau_\nu} = \tilde{S}_\nu \quad (2.19)$$

with the solution is

$$\tilde{I}_\nu(\tau_\nu) = \tilde{I}_\nu(0) + \int_0^{\tau_\nu} d\tau' \tilde{S}_\nu(\tau') \quad (2.20)$$

As a result, we obtain the solution for the equation (2.18)

$$I_\nu(\tau_\nu) = I_\nu(0)e^{-\tau_\nu} + \int_0^{\tau_\nu} d\tau' e^{-(\tau_\nu - \tau')} S_\nu(\tau') \quad (2.21)$$

Moreover, if the source function is independent of optical depth,

$$I_\nu(\tau_\nu) = I_\nu(0)e^{-\tau_\nu} + S_\nu(1 - e^{-\tau_\nu}) \quad (2.22)$$

Then, radiation transfer problem reduces to determine τ_ν along with the ray. Furthermore, if the emissivity was negligible, the solution of radiation transfer equation is simply proportion to $e^{-\tau_\nu}$.

The radiative flux is found by taking the moment of the intensity as

$$\vec{F}_\nu = \int d\Omega \vec{n} I_\nu \quad (2.23)$$

If the intensity is independent of the direction, the flux in a vertical direction, e.g., the flux at the surface of the star is

$$F_\nu = \int d\Omega \cos \theta I_\nu = \int_0^{2\pi} d\phi \int_0^\pi d\theta \sin \theta \cos \theta I_\nu = \pi I_\nu \quad (2.24)$$

2.1.3 Self-Shielding Effect

For simplicity, suppose the gas cloud composed of pure hydrogen. As described above, the UV radiation of $\nu > \nu_L$ photoionizes the hydrogen atom. On the other hand, photoionized hydrogen also recombines to any energy state with certain rate. If the recombination photon emitted by recombining to a ground state, the photon ionizes hydrogen again because its energy must be > 13.6 eV. However, if an electron recombined to the excitation state, the emitted photon never ionize hydrogen atom and escapes from the gas cloud. Thus, the net ionizing photon number decreases with interacting with the hydrogen atoms and recombining to the excitation state. As a result, UV photons penetrate gas cloud until ionization rate equals recombination rate for excitation state. This is the self-shielding effect. Since the self-shielded region is never photoheated, the low-mass cloud can be gravitationally unstable even though the entire mass of the cloud is less than $M_J(10^4 K)$. Therefore, the self-shielding effect is a critical physics for star cluster formation when the gas cloud is exposed to UV background radiation.

The recombination rate of hydrogen ion per unit volume is given by $n_e n_{\text{HII}} \alpha_B$ where n_e , n_{HII} are electron/ionized hydrogen number densities, respectively. α_B is recombination coefficient recombining to all energy level except for ground state hence

$$\alpha_B = \sum_{n=2} \alpha_n \quad (2.25)$$

where α_n is recombination coefficient recombining to n -th energy state. The recombination coefficient is temperature-dependent value, $\alpha_B = 2.59 \times 10^{-13} \text{ cm}^3 \text{ s}^{-1}$ at $T = 10^4$ K. If we assume UV photon number incident upon the cloud per unit time as \dot{N}_{ion} , the photoionizing volume of the cloud V_{ion} is determined by equating the photoionization rate to recombination rate

$$\dot{N}_{\text{ion}} = \int_{V_{\text{ion}}} dV n_e n_{\text{HII}} \alpha_B \quad (2.26)$$

and subtracted volume of $V_{\text{cloud}} - V_{\text{ion}}$ is self-shielded. If we suppose spherically symmetric uniform cloud radius of r and self-shielded neutral radius is r_{shield} , we can obtain

$$\dot{N}_{\text{ion}} = \frac{4\pi}{3} (r^3 - r_{\text{shield}}^3) n_e n_{\text{HII}} \alpha_B \quad (2.27)$$

According to equation (2.24), \dot{N}_{ion} is related to intensity I_ν as

$$\dot{N}_{\text{ion}} = 4\pi r^2 \int_0^{2\pi} \int_0^\infty \tilde{n} d\Omega \int_{\nu_L}^\infty d\nu \frac{I_\nu}{h\nu} \quad (2.28)$$

If we assume the power-law intensity $I_\nu = I_{\nu_L} (\nu/\nu_L)^{-\alpha}$,

$$\dot{N}_{\text{ion}} = \frac{4\pi r^2}{h\alpha} I_{\nu_L} \quad (2.29)$$

Therefore, the self-shielded radius r_{shield} is derived as

$$r_{\text{shield}} = \left[r^3 - \frac{3\pi r^2 I_{\nu_L}}{h\alpha n_e n_{\text{HII}} \alpha_B} \right]^{1/3} \quad (2.30)$$

The radius that r_{shield} converges to 0 is a critical radius $\equiv r_{\text{crit}}$. In this case, $n_e \sim n_{\text{HII}}$, then

$$r_{\text{crit}} = \left[\frac{3\alpha_B h}{16\pi^3 m_p^2} \right]^{1/5} M^{2/5} \left(\frac{I_{\nu_L}}{\alpha} \right)^{-1/5} \quad (2.31)$$

where M , m_p are cloud mass and proton mass, respectively. Assuming $T = 10^4$ K for photoionized gas, the critical radius can be obtained as

$$r_{\text{crit}} = 3.50 \text{ kpc} \left(\frac{M}{10^8 M_\odot} \right)^{2/5} \left(\frac{I_{21}}{\alpha} \right)^{-1/5} \quad (2.32)$$

also correspond critical density n_{crit} for the uniform sphere is

$$n_{\text{crit}} = 2.3 \times 10^{-2} \text{ cm}^{-3} \left(\frac{M}{10^8 M_\odot} \right)^{-1/5} \left(\frac{I_{21}}{\alpha} \right)^{3/5} \quad (2.33)$$

where I_{21} is intensity at Lyman-limit frequency normalized by $10^{-21} \text{ erg cm}^{-2} \text{ sec}^{-1} \text{ sr}^{-1}$. The self-shielding condition is analytically obtained in this manner. The equation (2.32) and (2.33) are similar to equation (1.1) and (1.2) derived by numerical radiation transfer calculation of Tajiri & Umemura (1998) exclusive of a little difference in the values. This is because of some ideal assumption for analytic derivation, such as discontinuity of photoionized/neutral regions, overestimate of ionizing photon in consequence of assuming that all photons emitted from the source contribute to photoionizing.

2.2 Numerical Method

We perform three-dimensional radiation hydrodynamics (3D-RHD) simulations and investigate star cluster formation process in a cold dark matter (CDM) cosmology framework. We assume the standard cold dark matter cosmology, thus, we neglect a dark energy density Ω_Λ . This is a good assumption for our interest of early universe. We consistently solve the three-dimensional hydrodynamics, non-equilibrium chemistry, radiative transfer, and gravitational force of dark matter (DM). The most of the code is developed by Kenji Hasegawa (Hasegawa & Umemura 2010), and we newly add star-formation part and optimized the formulation of hydrodynamics. Here, we show the description of the numerical methods and some essential point with regard to the simulation.

2.2.1 Three-Dimensional Hydrodynamics

Hydrodynamics is calculated by standard Smoothed Particle Hydrodynamics (SPH, basically based on Monaghan 1992; Thacker et al. 2000; Springel & Hernquist 2002; Springel 2010). The density at a -th SPH particle is described as

$$\rho_a = \sum_b m_b W(|\vec{r}_{ab}|, h_a) \quad (2.34)$$

where m_a , \vec{r}_{ab} , h_a , W , are the mass of the a -th particle, the relative position vector between a -th and b -th particle, the smoothing length of the a -th particle, and the kernel function, respectively. In this study, we adopt the standard spline kernel function which is the usual SPH smoothing kernel

$$W(r, h) = \frac{8}{\pi h^3} \begin{cases} 1 - 6u^2 + 6u^3 & 0 \leq u < 1/2 \\ 2(1 - u)^3 & 1/2 \leq u < 1 \\ 0 & u \geq 1 \end{cases} \quad (2.35)$$

where $u = r/h$.

The equation of motion of a -th SPH particle is described as

$$\frac{d\vec{v}_a}{dt} = \vec{g}_a - \sum_b m_b \left[\frac{P_a}{\Omega_a \rho_a^2} \nabla_a W_{ab}(h_a) + \frac{P_b}{\Omega_b \rho_b^2} \nabla_a W_{ab}(h_b) \right] - \sum_b m_b \Pi_{ab} \nabla_a \bar{W}_{ab} \quad (2.36)$$

$$P_a = \frac{k_B \rho_a T_a}{\mu_a} \quad (2.37)$$

where \vec{g}_a is the gravitational acceleration, P_a is the pressure of a -th particle and $W_{ab}(h_a) = W(|\vec{r}_{ab}|, h_a)$, respectively. Π_{ab} is the standard artificial viscosity of Monaghan (1992)

$$\Pi_{ab} = \frac{-\mu_{ab}(c_{s,a} + c_{s,b})/2 + 2\mu_{ab}^2}{(\rho_a + \rho_b)/2} \quad (2.38)$$

where $c_{s,a}$ denotes a sound speed of a -th particle and

$$\mu_{ab} = \begin{cases} h_{ab} \vec{v}_{ab} \cdot \vec{r}_{ab} / (|\vec{r}_a - \vec{r}_b|^2 + 0.01 h_{ab}^2) & \vec{v}_{ab} \cdot \vec{r}_{ab} < 0 \\ 0 & \vec{v}_{ab} \cdot \vec{r}_{ab} > 0 \end{cases} \quad (2.39)$$

\bar{W}_{ab} is the symmetrized kernel function given by

$$\bar{W}_{ab} = \frac{1}{2} [W_{ab}(h_a) + W_{ab}(h_b)] \quad (2.40)$$

and the Ω_a is described as

$$\Omega_a = 1 - \frac{\partial h_a}{\partial \rho_a} \sum_b m_b \frac{\partial W_{ab}}{\partial h_a} \quad (2.41)$$

The Ω is a correction term for energy conservation caused by variability of smoothing length (Springel & Hernquist 2002). To calculate the Ω -term, we have to define the relationship between ρ and h . Price & Monaghan (2007) assume the relation as

$$h_a = \eta \left(\frac{m_a}{\rho_a} \right)^{1/3} \quad (2.42)$$

or more explicit formula is

$$\frac{4\pi}{3} h_a^3 \rho_a - m_a N_{\text{neigh}} = 0 \quad (2.43)$$

where η is the dimensionless parameter. The neighbor particle number N_{neigh} is given by $N_{\text{neigh}} = \frac{4\pi}{3} \eta^3$. We assume $\eta = 2.4$ which is corresponding to ~ 60 neighbor particles.

To determine the smoothing length h_a , we consider the following equation

$$f(h_a) = \rho_a(h_a) - \rho_{\text{sum},a}(h_a) = 0 \quad (2.44)$$

where ρ_a is a density which is given by equation (2.42), and $\rho_{\text{sum},a}$ is a density calculated by equation (2.34). According to Newton-Raphson method, the solution of the above equation is given by the recurrence formula

$$h_{a,\text{new}} = 1 - \frac{f(h_a)}{f'(h_a)} \quad (2.45)$$

where $f'(h_a)$ is the differential, thus,

$$f'(h_a) = \frac{\partial \rho_a}{\partial h_a} - \sum_b m_b \frac{\partial W_{ab}}{\partial h_a} = -\frac{3\rho_a}{h_a} \Omega_a \quad (2.46)$$

We iteratively renew the $h_{a,\text{new}}$ until satisfying the convergence criterion. The criterion is set as $|h_{a,\text{new}} - h_a|/h_a < 0.001$. The Newton-Raphson iteration method rapidly converges to the solution, but initial h_a has to be close to the actual solution. If the iteration crashes in Newton-Raphson method, we switch the iteration to the bisection method.

Then, the derivative value is given by

$$\frac{\partial h_a}{\partial \rho_a} = -\frac{h_a}{3\rho_a} \quad (2.47)$$

and the Ω -term can be obtained. The equation of motion is integrated using second-order leap-frog algorithm.

$$\vec{v}^{(i+1/2)} = \vec{v}^{(i)} + \Delta t \frac{\vec{a}(\vec{x}^{(i)})}{2} \quad (2.48)$$

$$\vec{x}^{(i+1)} = \vec{x}^{(i)} + \Delta t \vec{v}^{(i+1/2)} + \Delta t^2 \frac{\vec{a}^{(i+1)}}{2} \quad (2.49)$$

$$\vec{v}^{(i+1)} = \vec{v}^{(i+1/2)} + \Delta t \frac{\vec{a}(\vec{x}^{(i+1)})}{2} \quad (2.50)$$

The energy equation is given by

$$\frac{du_a}{dt} = -\frac{\Lambda_a - \Gamma_a}{\rho_a} + \frac{P_a}{\Omega_a \rho_a^2} \sum_b m_b \vec{v}_{ab} \cdot \nabla_a W_{ab} + \sum_b m_b \frac{1}{2} \Pi_{ab} \vec{v}_{ab} \cdot \nabla_a \bar{W}_{ab} \quad (2.51)$$

where Λ_a and Γ_a are the cooling/heating rate. The adiabatic heating, heating due to radiative process and cooling due to chemical reaction are taken into account, and the energy equation is consistently coupled with radiation transfer and non-equilibrium chemical reaction.

In SPH scheme, local Jeans instability has to be represented by several times its neighbor particle number. Namely, the mass-resolution for SPH simulation is given by

$$M_J \gtrsim \lambda \times N_{\text{neighbor}} m_{\text{SPH}} \quad (2.52)$$

where N_{neighbor} is the neighbor particle number ~ 60 and λ is a dimensionless factor of $1.5 \sim 2$ (Bate & Burkert 1997; Bate et al. 2003). The Jeans mass of equation (2.52) has to be set as what we would like to resolve. In this thesis, the main interest is the evolution of gas cloud and dynamical feature of the star cluster formed in UV background radiation. We have to consider the local star formation, but we do not resolve individual star formation. Hence, we adopt the simple-stellar-population (SSP) approximation, we assume that "stellar particle" represents the association of star with certain initial mass function (IMF). Thus, we would like to resolve the Jeans instability at the critical density of the cloud, in other words, the scale that the first fragmentation occurs. In this study, the SPH particle mass is set to be the order of $10M_{\odot}$ thereby the mass resolution is $\sim 1000M_{\odot}$. Then, the local Jeans instability of primordial gas of at $\sim 10^4 \text{ cm}^{-3}$ can be resolved (Omukai et al. 2005, see Figure 2.2).

As for gravitational force calculation, both baryonic particles and DM particles are considered. The Tree-algorithm is adopted to reduce the computational cost of gravitational interaction (Barnes & Hut 1986), and the opening angle is set to be $\theta = 0.5$.

2.2.2 Cooling & Chemical Reactions

Through this study, we assume primordial composition and consider the 6 species, e^- , H^+ , H , H^- , H_2 , and H_2^+ . The cooling due to metals are neglected despite that GCs are categorized as Population II (Pop II), formed in the early stage of the universe but are not first stars hence they contain few metals, typical order of $\sim Z/Z_{\odot} = 10^{-2}$. As we see in Figure 2.2, the thermal evolution strongly depends on the composition of the gas. However, our primary interest is the evolution of gas exposed to UV background radiation. Therefore, the cooling process at the temperature of $\sim 10^{3-4}$ K is the most important, regarding photoheating and self-shielding effect. As seen in Figure 2.1, the primary coolant is H_2 at the temperature range of $T \sim 10^{3-4}$ K as long as the low metallicity gas of $Z/Z_{\odot} \leq 10^{-2}$. Also, atomic cooling is negligible at $T < 10^4$ K, hence we can also neglect He atom. Consequently, it is concluded that pure hydrogen composition is still a good approximation to pursue the thermal process of the gas cloud in the early universe.

As for cooling processes, collisional ionization cooling, collisional excitation cooling, recombination cooling, bremsstrahlung radiation cooling of the hydrogen atom, and line cooling of the hydrogen molecule are considered. The cooling functions Λ are given by

- Collisional ionization cooling (bound-free transition)

$$\Lambda^{\text{bf}} = 1.27 \times 10^{-21} T^{1/2} \left[1 + \left(\frac{T}{10^5} \right)^{1/2} \right]^{-1} \exp[-1.58 \times 10^5 / T] n_{\text{H}_I} n_e \text{ erg cm}^{-3} \text{ s}^{-1} \quad (2.53)$$

- Collisional excitation cooling (bound-bound transition)

$$\Lambda^{\text{bb}} = 7.5 \times 10^{-19} \left[1 + \left(\frac{T}{10^5} \right)^{1/2} \right]^{-1} \exp[-1.18 \times 10^5 / T] n_{\text{H}_I} n_e \text{ erg cm}^{-3} \text{ s}^{-1} \quad (2.54)$$

- Recombination cooling (free-bound transition)

$$\Lambda^{\text{fb}} = 6.50 \times 10^{-27} T^{1/2} \left(\frac{T}{10^3} \right)^{-0.2} \left[1 + \left(\frac{T}{10^6} \right)^{0.7} \right]^{-1} n_{\text{H}_\text{II}} n_e \text{ erg cm}^{-3} \text{ s}^{-1} \quad (2.55)$$

- Bremsstrahlung radiation (free-free transition)

$$\Lambda^{\text{ff}} = 1.42 \times 10^{-27} g_{\text{ff}} T^{1/2} n_{\text{H}_\text{II}} n_e \text{ erg cm}^{-3} \text{ s}^{-1} \quad (2.56)$$

- H₂ line cooling

$$\Lambda_{\text{H}_2} = \frac{\Lambda_{\text{H}_2}(\text{LTE})}{1 + n^{\text{cr}}/n_{\text{H}_I}} \text{ erg cm}^3 \text{ s}^{-1} \quad (2.57)$$

where g_{ff} is Gaunt factor, $\Lambda(\text{LTE})$ is the cooling function for LTE and n^{cr} is the critical density defined as

$$\frac{n^{\text{cr}}}{n_{\text{H}_I}} = \frac{\Lambda_{\text{H}_2}(\text{LTE})}{\Lambda_{\text{H}_2}(n_{\text{H}_I} \rightarrow 0)}$$

where $\Lambda_{\text{H}_2}(n_{\text{H}_I} \rightarrow 0)$ denotes the cooling function with a low-density limit. For the atomic and H₂ cooling function, we adopt the formula of Fukugita & Kawasaki (1994) and Galli & Palla (1998), respectively.

The estimation of the local fractions of all species is required to evaluate the cooling rate. In the general formula, the non-equilibrium chemistries are described as

$$\frac{dy_i}{dt} = \sum_j \sum_k k_{jk} y_j y_k + \sum_l \sum_m \sum_n k_{lmn} y_l y_m y_n \quad (2.58)$$

where y_i , k_{jk} or k_{lmn} are the fractions of i -th species and reaction rate. The first term denotes the two-body interaction and second is the three-body interaction, respectively. Since the chemical reaction time-scale is sufficiently small compared with the dynamical time-scale, the non-equilibrium chemical reactions are implicitly solved. The chemical reaction rates are taken from Galli & Palla (1998) and Shapiro & Kang (1987). Moreover, the reaction with radiation should be added to the equation (2.58). As for the reactions rate related to radiative process, the rates are evaluated by solving radiation transfer equation.

2.2.3 Three-Dimensional Ray-Tracing & Description of Radiative Processes

Several numerical scheme to solve the RHD problem have been developed ever (e.g., Iliev et al. 2006, 2009). In this study, SPH coupled with Radiation transfer (RSPH) scheme developed by Susa (2006) is adopted to perform the three-dimensional ray-tracing. In RSPH method, we create only one grid point on the light ray from source to SPH particle by assigning the physical variables of neighbor particle hence we do not create the grid point by using all SPH particles that contribute to the light ray. Although the accuracy is somewhat inferior as compared with the SPH-based scheme developed by Kessel-Deynet & Burkert (2000), computational cost for ray-tracing is reduced.

For three-dimensional ionization process, the shadowing effect is of concern for anisotropic, i.e., one-sided like background radiation field. As for the shadowing effect, the ionizing erosion caused by diffuse recombination photons ($\nu > \nu_L$) is non-negligible when the size of local dense clump r_{clump} is less than the mean-free-path of ionizing photon L_{mfp} (Hasegawa & Umemura 2010). At Lyman limit frequency, L_{mfp} is given by

$$L_{\text{mfp}} = 51.4 \times \left(\frac{10^{-3} \text{ cm}^{-3}}{n_{\text{H}}} \right) \text{ pc} \quad (2.59)$$

If $r_{\text{clump}} < L_{\text{mfp}}$, the emissivity have to be taken into account in radiation transfer equation (equation 2.15). In this study, the most interest is to consider the GC-sized star cluster formation, thus, the minimum gas clump size located in the center of the cloud can roughly be estimated as ~ 10 pc. Thus, the condition $r_{\text{clump}} > L_{\text{mfp}}$ is satisfied when the number density of surrounding gas is $\sim 10^{-2} \text{ cm}^{-3}$. Actually, the condition is satisfied through the simulations, and the erosion would be negligible in the shadowing region.

For the reason, we adopt on-the-spot approximation or Case B (Spitzer 1978), assuming that recombination photon emitted by recombining to ground state is immediately absorbed into the emitted region and emission term is reduced from radiation transfer equation (2.15). Thus, the solution can be rewritten simply as

$$I_{\nu}(\tau_{\nu}) = I_{\nu}(0) \exp(-\tau_{\nu}) \quad (2.60)$$

The photoionization rate k_{ion} and photoheating Γ_{ion} are obtained as

$$k_{\text{ion}} = \int_{\nu_L}^{\infty} d\nu \int d\Omega \frac{I_\nu}{h\nu} n_{\text{H}} \sigma_\nu \quad (2.61)$$

$$\Gamma_{\text{ion}} = \int_{\nu_L}^{\infty} d\nu \int d\Omega \frac{I_\nu}{h\nu} n_{\text{H}} \sigma_\nu (h\nu - h\nu_L) \quad (2.62)$$

with photoionization cross-section for hydrogen atom is given by

$$\sigma_\nu = 6.30 \times 10^{-18} \left(\frac{\nu_L}{\nu} \right)^3 \text{ cm}^2 \quad (2.63)$$

for neutral hydrogen atoms.

The photodesorption rate for H^- and photodissociation rate for H_2^+ are calculated by

$$k_{\text{H}^-} = \int_{0.74\text{eV}}^{13.6\text{eV}} d\nu \int d\Omega \frac{\sigma_{\text{H}^-} I_\nu}{h\nu} \quad (2.64)$$

$$k_{\text{H}_2^+} = \int_{0.062\text{eV}}^{13.6\text{eV}} d\nu \int d\Omega \frac{\sigma_{\text{H}_2^+} I_\nu}{h\nu} \quad (2.65)$$

The cross-section σ_{H^-} is taken from Tegmark et al. (1997), and $\sigma_{\text{H}_2^+}$ is taken from Stancil (1994). Through this study, photodesorption of H^- and photodissociation of the H_2^+ are assumed to be optically thin owing to their small fraction.

The H_2 photodissociation, we adopt the self-shielding function derived by Draine & Bertoldi (1996). The photodissociation rate k_{H_2} is given by

$$k_{\text{H}_2} = 1.13 \times 10^{18} F_{\text{LW}} f_{\text{shield}} \left(\frac{N_{\text{H}_2}}{10^{14} \text{ cm}^2} \right) \quad (2.66)$$

with the self-shielding function described as

$$f_{\text{shield}}(x) = \begin{cases} 1 & x \leq 1 \\ x^{-3/4} & x > 1 \end{cases} \quad (2.67)$$

where F_{LW} indicates unshielded incoming radiative flux at 12.4 eV and N_{H_2} is H_2 column density, respectively.

2.2.4 Star Formation

The stars are considered to be formed in dense, sufficiently cooled gas component. In this sense, we set the star formation criteria as follows : (1) $\nabla \cdot \vec{v} < 0$, (2) $y_{\text{H}_2} \geq 5 \times 10^{-4}$ and (3) $T \leq 5000\text{K}$ where \vec{v} , y_{H_2} , T are the local velocity, hydrogen molecular fraction and temperature, respectively. In SPH, the contraction term $\nabla \cdot \vec{v}$ is given by

$$\nabla \cdot \vec{v}_a = \frac{1}{\rho_a \Omega_a} \sum_b m_b (\vec{v}_a - \vec{v}_b) \cdot \frac{\partial W_{ab}(h_a)}{\partial \vec{r}_a} \quad (2.68)$$

In particular, condition (2) and (3) are never satisfied unless gas is self-shielded against the UV photon and effectively cooled by H_2 . Thus, these are prime conditions for simulating the star formation in UV background radiation field.

Next, we consider the timescale that converts the gas particle into the collisionless stellar particle as follow: The star formation timescale is roughly considered to be consistent with the local free-fall timescale t_{ff} . One-dimensional calculation of Hasegawa et al. (2009) have assumed that the timescale of star formation is sufficiently shorter than the dynamical time of the cloud, thus, the gas shell is immediately converted to the collisionless stellar shell when the gas satisfies the star formation criteria. They have neglected the star formation timescale; nevertheless, it is a reasonable assumption because the one-dimensional simulation

cannot originally pursue the local density structure and star formation there. On the other hand, Susa & Umemura (2004) have treated the star formation in three-dimensional SPH simulation with taking into account the timescale of star formation. For the conversion timescale from gas particle to stellar particle, they have assumed the simple formula

$$\frac{d\rho_{\text{gas}}}{dt} = -\frac{d\rho_*}{dt} \quad (2.69)$$

and

$$\frac{d\rho_*}{dt} = c_* \frac{\rho_{\text{gas}}}{t_{\text{ff}}} \quad (2.70)$$

where ρ_* is a stellar density, ρ_{gas} is a gas density, and c_* is a dimensionless parameter to control star formation efficiency. When the gas particle satisfied the star formation criteria, the gas particle is converted to stellar particle after the time $\Delta t_{\text{form}} = t_{\text{ff}}/c_*$. However, it should be mentioned that the simulation timestep is typically much smaller than the Δt_{form} . Hence, until waiting for the conversion timescale, the density evolve to denser and the simulation time step becomes to be tiny. To avoid this, they have introduced the minimum smoothing length to prevent stopping the simulation. However, this method has a somewhat disadvantage concerning the computational cost, since the number of neighbor particle sufficiently increases.

In this study, we treat the star formation *stochastically* (Okamoto et al. 2003, 2005). From the equation (2.70), we can derive the stellar mass Δm_* that formed from gas of mass m_{gas} during the timestep Δt

$$\Delta m_* = m_{\text{gas}} \left\{ 1 - \exp\left(-c_* \frac{\Delta t}{t_{\text{ff}}}\right) \right\} \quad (2.71)$$

Unfortunately, however, Δm_* is very small in general hence it is numerically difficult to treat. Thus, we derive the probability p_* that gas particle of mass m_{gas} forms the stellar particle stochastically stellar particle of mass $\alpha_* \times m_{\text{gas}}$ ($0 < \alpha_* < 1$) during the time step Δt as

$$p_* = \alpha_*^{-1} \left\{ 1 - \exp\left(-c_* \frac{\Delta t}{t_{\text{ff}}}\right) \right\} \quad (2.72)$$

The α_* and c_* are the free parameter, thus, we can choose the value arbitrarily. We assume $\alpha_* \sim 0.3$ (Okamoto et al. 2003, 2005), and c_* is set as unity.

In every timestep, the conditions for star formation is recalculated and solve the equation (2.72) if the particle has satisfied the star formation criteria. At the same time, we generate the uniform random numbers r_{random} distributed between 0 and 1. Then, if $r_{\text{random}} < p_*$, the gas particle is converted to collisionless stellar particles.

2.2.5 Setup

Hasegawa et al. (2009) have explored the dependency of the cloud mass, collapse epoch, UV background intensity, and the epoch of irradiation on the models of star cluster formation that described in §1.2.3. Hasegawa et al. (2009) have summarized the dependency as shown in Figure 2.2.5. They have revealed that the supersonic infall can be expected preferentially in the low-mass high- σ ($\gtrsim 1\sigma$) overdensity peak. Hence in this study, the low-mass gas cloud with the initial baryonic mass of $10^6 M_{\odot} \leq M_{\text{ini}} \leq 10^7 M_{\odot}$ with DM halo that collapses at collapse redshift z_c of $6 \leq z_c \leq 12$ are considered.

The gas cloud with a DM subhalo that comes up to maximum expansion epoch at redshift $z = z_{\text{max}}$ are firstly generated, and we pursue the contraction evolution of the cloud. Here, z_{max} is related to collapse redshift z_c as $(1 + z_{\text{max}}) = 2^{2/3}(1 + z_c)$.

The maximum expansion (or turnaround) radius is given by

$$r_{\text{max}} = \left(\frac{4M}{3\pi^3 \rho_{c0}} \right)^{1/3} (1 + z_{\text{max}})^{-1} \quad (2.73)$$

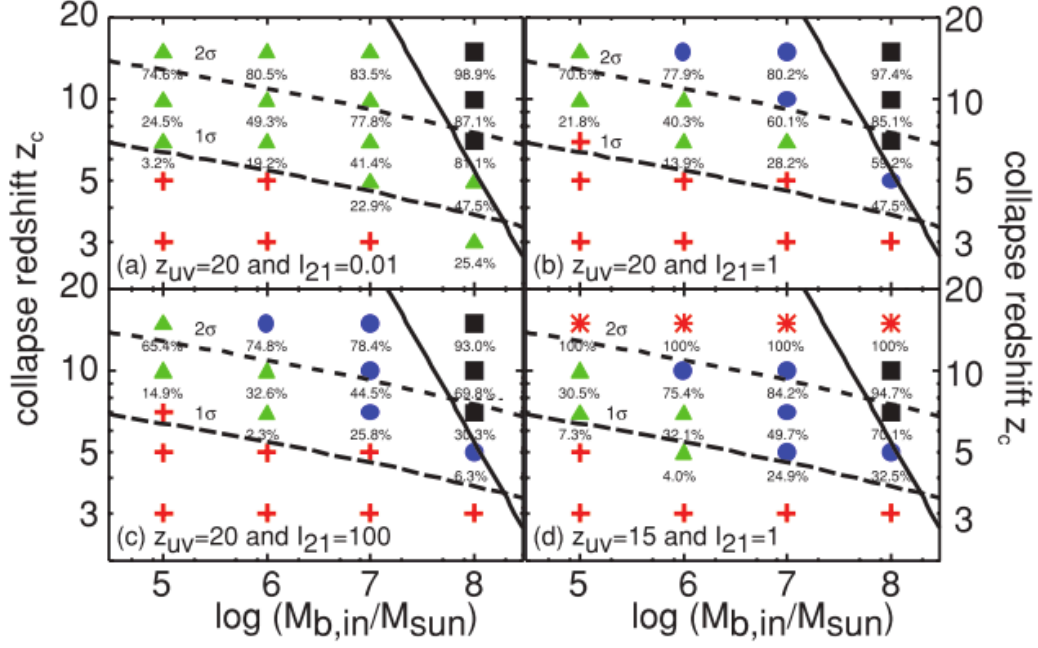


Fig. 2.3: Parameter dependency on shielding branches, taken from Hasegawa et al. (2009). The long- and short-dashed line denote the 1σ and 2σ CDM overdensity fluctuations. The blue-circle denotes the star cluster formed via supersonic infall. The green-triangle is formed via prompt star formation.

where M , $\rho_{c0} = 3H_0^2/(8\pi G)$ are the total mass of the cloud, and present cosmic critical density, respectively.

As for the initial overdensity structure for both baryon and DM, the spherical symmetric fluctuation profile is assumed. One of the most significant advantage of assuming the overdensity profile is to avoid the concentration on a central point of the system that induces non-negligible numerical error at the collapse epoch. In this study, the overdensity profile is assumed as (Kitayama et al. 2001)

$$\delta(r) \equiv \frac{\rho(r) - \rho_c}{\rho_c} = \delta_0 \frac{\sin(\lambda r)}{\lambda r} \quad (2.74)$$

Moreover, the corresponding volume-averaged overdensity profile is given by

$$\bar{\delta}(r) = 3\delta_0 \frac{\sin(kr) - kr \cos(kr)}{(kr)^3} \quad (2.75)$$

where $\rho_c = 3H(z_{\max})^2/(8\pi G)$ is the critical density at turnaround epoch, r is the distance from the center of the cloud, λ is the wave number defined by the cloud radius r_{\max} as $\lambda r_{\max} = \pi$, and δ_0 is constant that adjust the amplitude of overdensity. In Einstein-de Sitter universe, overdensity at the turn-around epoch is defined as

$$\delta_{\max} = \frac{9\pi^2}{16} - 1 \quad (2.76)$$

Therefore, we set the δ_0 as

$$\bar{\delta}(r_{\max}) = 3\frac{\delta_0}{\pi^3} = \frac{9\pi^2}{16} - 1 \quad (2.77)$$

In addition to the spherically symmetric overdensity profile, the three-dimensional inhomogeneity of the density field is taken into account. The density field is represented as the random-Gaussian density field that obeys a power-law power spectrum, namely

$$P(k) = \langle |\tilde{\delta}(\vec{k})|^2 \rangle_{|\vec{k}|=k} = Ak^p \quad (2.78)$$

with

$$\bar{\delta}(\vec{k}) = \int d^3x \delta(\vec{r}) e^{-i\vec{k}\cdot\vec{r}} \quad (2.79)$$

where \vec{k} is the wave number vector. The realization of the random-Gaussian density field for given power spectrum is based on Braun et al. (1988, see Appendix). The power index is chosen as $p = -3$, i.e., scale-free density fluctuation, motivated by the extrapolation from CDM power spectrum. The amplitude of the power spectrum A is related to the initial clumping factor of the gas cloud $C = \langle n^2 \rangle / \langle n \rangle^2$. As for initial density field, the small fluctuation is assumed. The A is set to be that the initial clumping factor $C = 1.7$. For SPH, the clumping factor is evaluated by following simple formula (Springel & Hernquist 2003)

$$C = \frac{\sum_i m_i \rho_i^{-1} \sum_j m_j \rho_j}{(\sum_i m_i)^2} \quad (2.80)$$

An example of the density distribution and the power spectrum is shown in Figure 2.4.

We define the critical ionizing photon number per unit time $\equiv \dot{N}_{\text{crit}}$, as that required ionizing the entire volume of the gas cloud V_{cloud} . The critical ionizing photon number is evaluated by modifying the equation (2.26), and which is given by (Madau et al. 1999),

$$\dot{N}_{\text{crit}} = \langle n \rangle^2 \alpha_B C V_{\text{cloud}} \quad (2.81)$$

where the complete photoionization (ionization rate equals unity) is assumed.

Through this study, the UV photon number incident on the cloud \dot{N}_{ion} is defined as the unit of \dot{N}_{crit} . For supersonic infall case $\dot{N}_{\text{ion}}/\dot{N}_{\text{crit}} = 10$ is assumed hence contraction of photoionized gas can be expected. On the other hand, we set $\dot{N}_{\text{ion}}/\dot{N}_{\text{crit}} = 0.1$ for prompt star formation case, thus, the self-shielding region would immediately form.

As for background radiation field, the two extreme cases are considered: one-sided background radiation, one source is located on the x-axis, and isotropic background radiation, 18 sources are isotropically surrounded around the cloud. An ionizing photon number incident upon the cloud is set to be equal to investigate the effect of anisotropy of the radiation field.

The epoch of irradiation z_{UV} is assumed as $6 \leq z_{\text{UV}}$ because the strong UV background radiation field can be expected in such epoch regarding cosmic reionization (see chapter 1).

Finally, the background intensity is also specified as

$$J_{21} \times 10^{-21} \text{ erg cm}^{-2} \text{ s}^{-1} \text{ Hz}^{-1} \text{ sr}^{-1} = \frac{\dot{N}_{\text{ion}} h \alpha}{4\pi^2 R_{\text{cloud}}^2} \quad (2.82)$$

where R_{cloud} is the radius of the gas cloud ¹.

The parameter set of this work is summarized in Table 2.1.

¹The background intensity is defined as an isotropic formula of equation (2.29) regardless of practical anisotropy of radiation field. In the light of this definition, the notation J_{21} , meaning of intensity averaged over angular direction, is more proper rather than I_{21} .

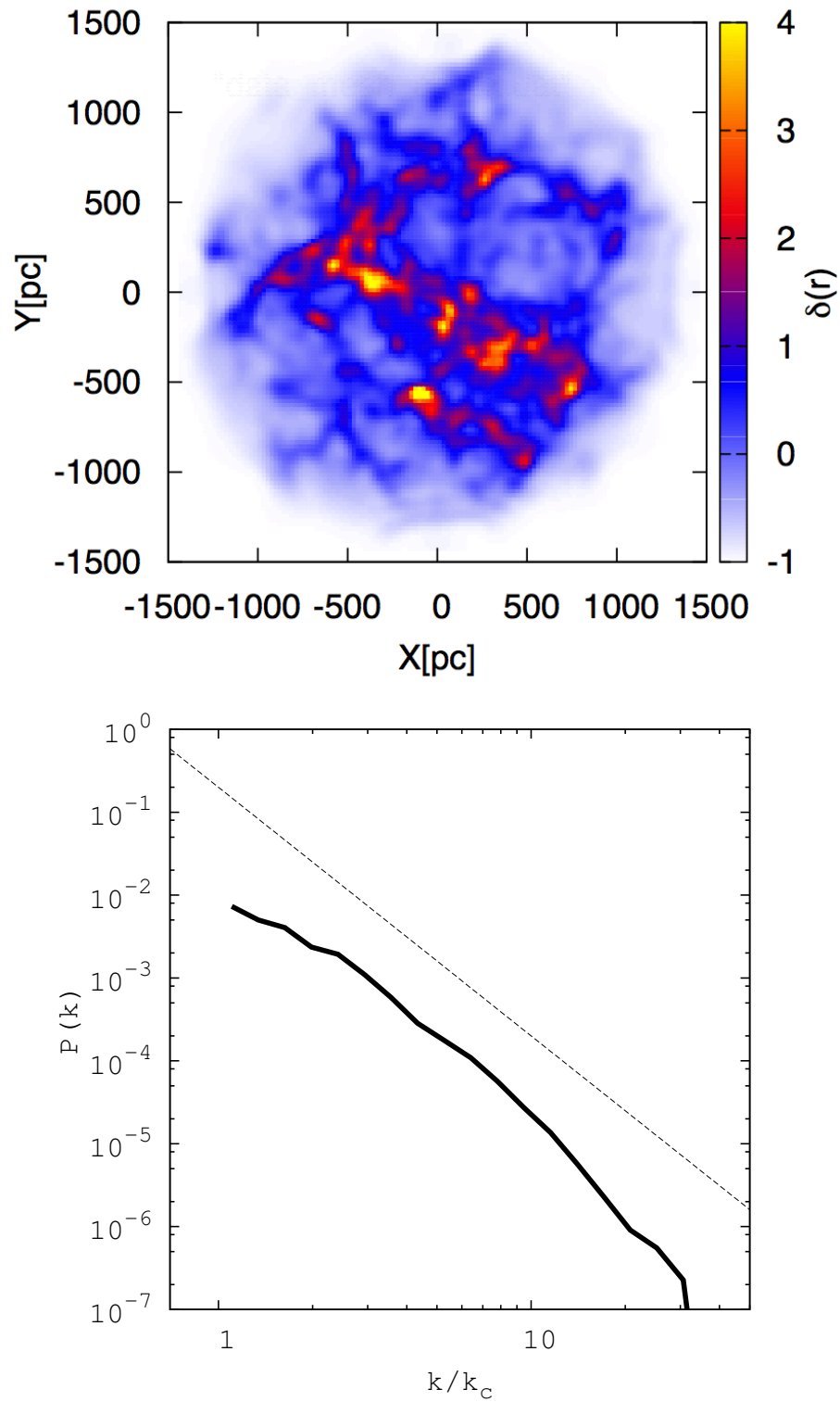


Fig. 2.4: Initial density field of the cloud. In upper panel, the color indicates the density fluctuation $\delta(r)$ as represented by the color bar. Bottom panel indicates the power spectrum. Dashed line represents the relation $P(k) \propto k^{-3}$.

Table. 2.1: The parameters

z_c	radiation field	formation	z_{UV}	M_{ini} [$10^6 M_{\odot}$]	$\dot{N}_{\text{ion}}/\dot{N}_{\text{crit}}$	J_{21}/α
6	one-sided/isotropic	supersonic	6.8	2.5	10	386.0
6	one-sided/isotropic	supersonic	6.9	5.0	10	399.8
9	one-sided/isotropic	supersonic	10.3	2.5	10	939.8
9	one-sided/isotropic	supersonic	10.5	5.0	10	236.5
12	one-sided/isotropic	supersonic	13.8	2.5	10	1762.1
12	one-sided/isotropic	supersonic	14.0	5.0	10	1172.5
9	one-sided	supersonic	10.5	10.0	10	716.3
12	one-sided	supersonic	14.0	10.0	10	2127.1
6	one-sided	prompt	8	2.5	0.1	9.5×10^{-3}
6	one-sided	prompt	8	5.0	0.1	1.3×10^{-2}
9	one-sided	prompt	8	1.0	0.1	3.7×10^{-3}
9	one-sided	prompt	12	2.5	0.1	5.6×10^{-2}
9	one-sided	prompt	12	5.0	0.1	7.5×10^{-2}
9	one-sided	prompt	12	10.0	0.1	9.6×10^{-2}
12	one-sided	prompt	15.9	1.0	0.1	0.15
12	one-sided	prompt	15.9	2.5	0.1	0.22
12	one-sided	prompt	15.9	5.0	0.1	0.29

Chapter 3 Results

3.1 Contraction of Gas Clouds in Three-Dimensional UV Background Radiation

3.1.1 Supersonic Infall in Anisotropic Background Radiation Field

First, we investigate how are the contraction and self-shielding process that has been proposed by one-dimensional spherical symmetric RHD calculation affected by the three-dimension.

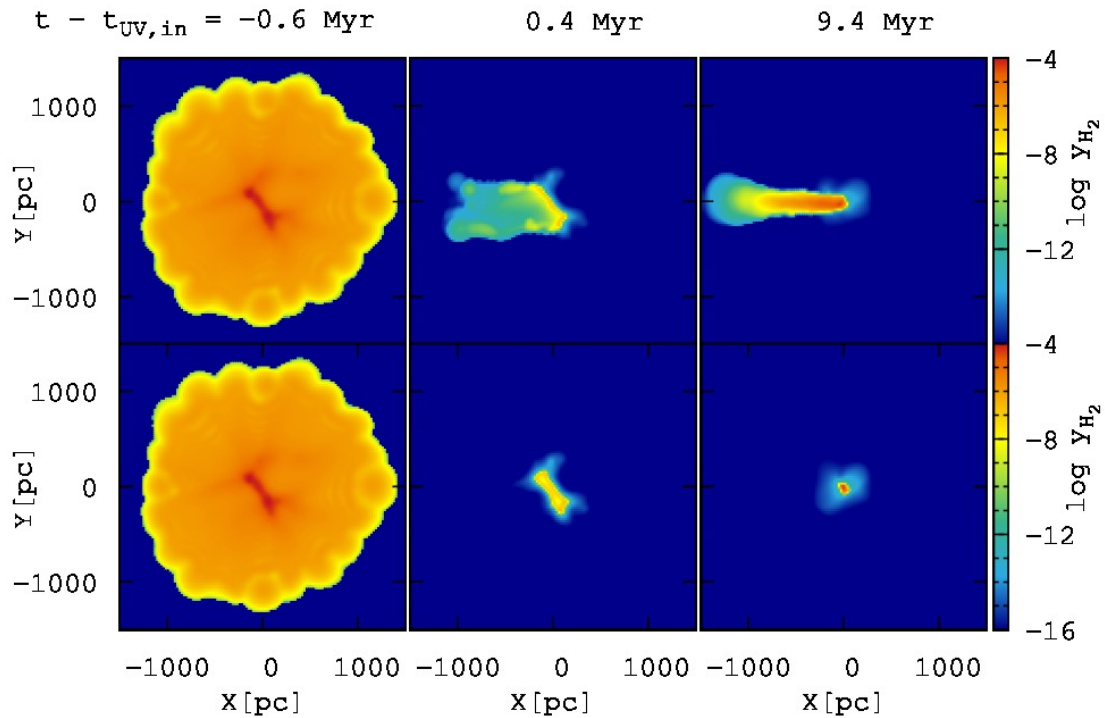
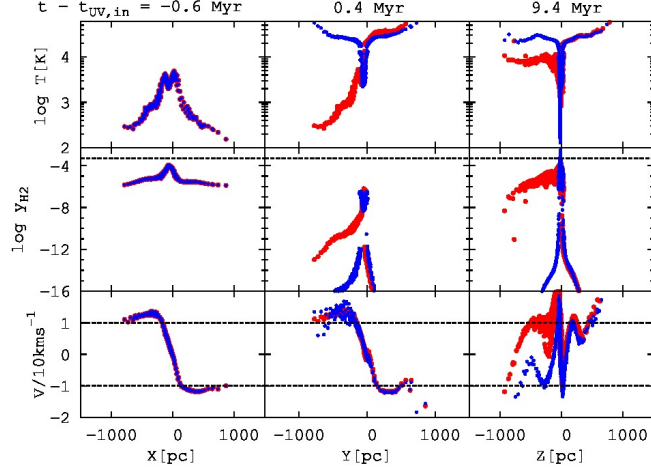
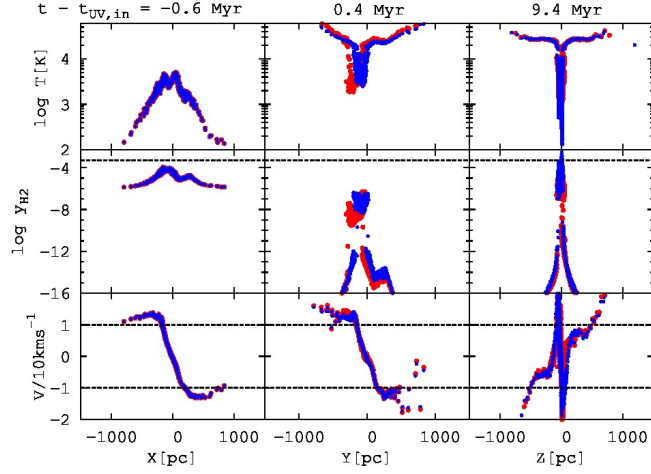


Fig. 3.1: Time evolution of the gas cloud of $M_{\text{ini}} = 5 \times 10^6 M_{\odot}$, $z_c = 9$ irradiated at $z_{\text{UV}} = 10.5$ with intensity of $\dot{N}_{\text{ion}}/\dot{N}_{\text{crit}} = 10$. Upper panel shows the one-sided background radiation and the lower panel is an isotropic one. In the case of one-sided radiation, the source is located on the x-axis and the cloud is irradiated from the right-hand side. On the other hand, as for isotropic background radiation, the 18 sources are isotropically distributed around the cloud. The panels show the H_2 distribution on the x-y plane, represented in logarithmic scale as shown in the color bars. The left panel indicates the cloud at 0.6 Myr before irradiation while the middle and right panel show the states at 0.4 Myr and 9.4 Myr after irradiation, respectively. The panels show the $1500 \text{ pc} \times 1500 \text{ pc}$ region.

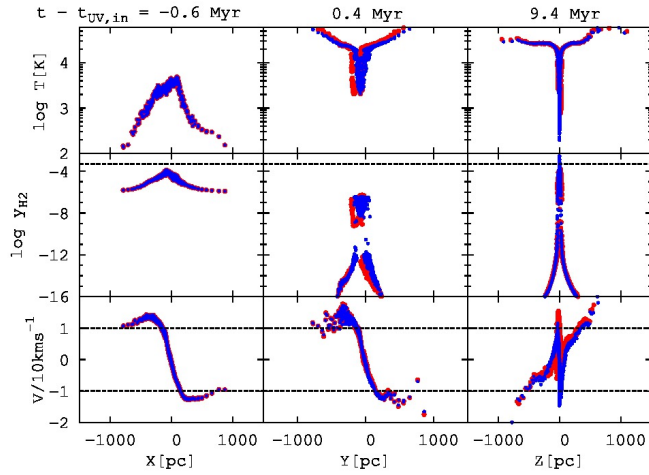
3.1 Contraction of Gas Clouds in Three-Dimensional UV Background Radiation



(a) Physical values on x-axis



(b) Physical values on y-axis



(c) Physical values on z-axis

Fig. 3.2: Temperature T (upper), H_2 fraction (middle), and velocity (bottom) on the (a)x-, (b)y-, (c)z-axis are shown. The initial condition for the cloud is $M_{\text{ini}} = 5 \times 10^6 M_{\odot}$, $z_c = 9$, and irradiated at $z_{\text{UV}} = 10.5$ with intensity of $\dot{N}_{\text{ion}}/\dot{N}_{\text{crit}} = 10$. From left- to right-hand side, each panel is compatible with the time sequence of Figure 3.1. The red points indicate one-sided background radiation case, and the blue points are isotropic background radiation. Horizontal dashed lines in the bottom panel represented the velocity of 10 km/s and hydrogen molecular fraction of 5×10^{-4} in the middle panel.

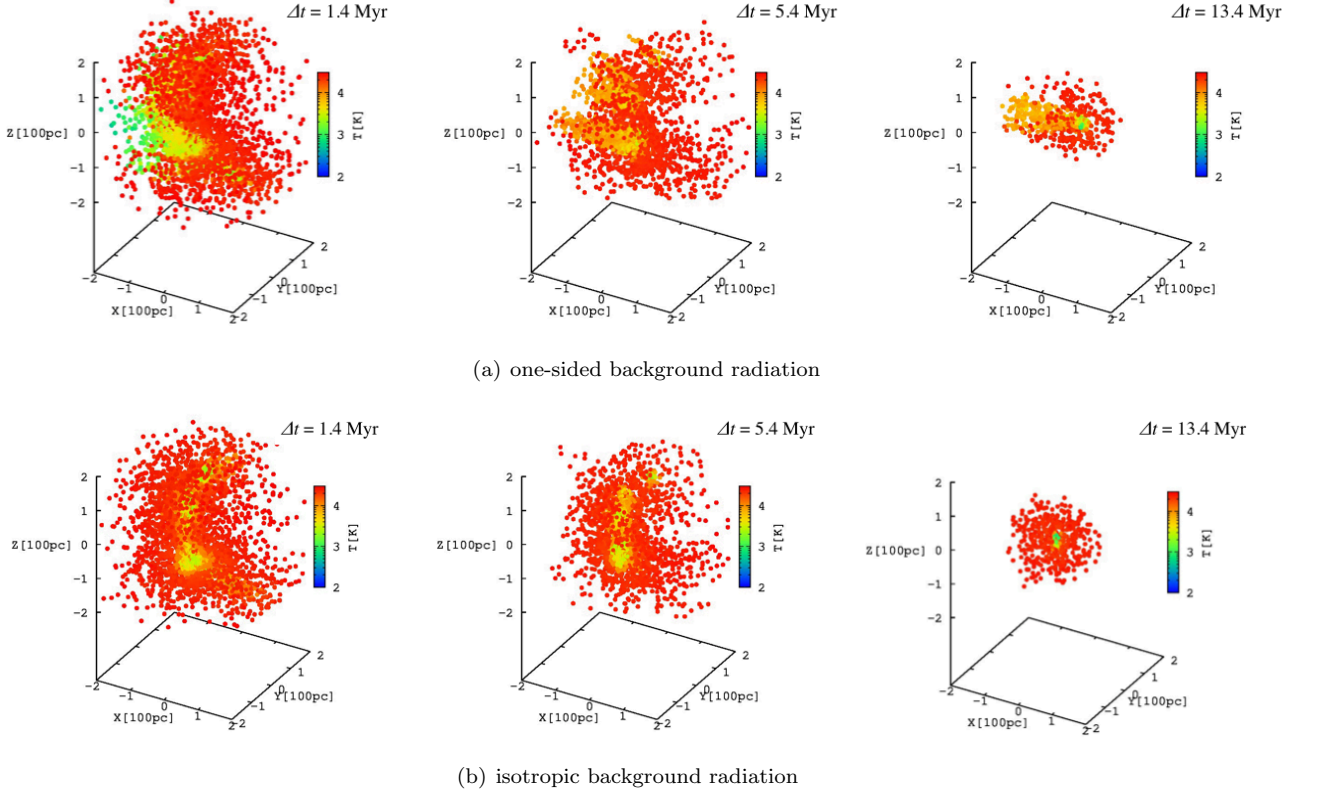


Fig. 3.3: Three-dimensional distribution of SPH particles at 1.4 Myr, 5.4 Myr, and 13.4 Myr after irradiation. The initial condition for the cloud is $M_{\text{ini}} = 5 \times 10^6 M_{\odot}$, $z_c = 9$, and irradiated at $z_{\text{UV}} = 10.5$ with intensity of $\dot{N}_{\text{ion}}/\dot{N}_{\text{crit}} = 10$. In this Figure, only the SPH particles that contract to the center of mass are chosen, evaporated particles are omitted. The color indicates the temperature in logarithmic scale as described in the color bar. The box size is 400 pc at the center of the cloud. Note that, the particles displayed in the box is not all of the particle, appropriately thinned out in the light of visibility.

Figure 3.1 shows the time evolution of the gas cloud of $M_{\text{ini}} = 5 \times 10^6 M_{\odot}$, $z_c = 9$ irradiated by one-sided/isotropic background radiation with UV intensity $\dot{N}_{\text{ion}}/\dot{N}_{\text{crit}} = 10$. In addition, the temperature T , H_2 fraction, and velocity profiles on x -, y -, z -axis are shown in Figure 3.2. In the simulation run, the infall velocity exceeds 10 km/s before irradiation (see left panel of Figure 3.2). Hence, the supersonic infall proposed by Hasegawa et al. (2009) can be expected.

Regardless of anisotropy of radiation, the bulk of the cloud is photoionized and photodissociated at the moment of irradiation owing to the strong background UV intensity of $\dot{N}_{\text{ion}}/\dot{N}_{\text{crit}} = 10$ (see middle panel of Figure 3.1). However, we see in the middle panel of Figure 3.2, the photoionized part of the cloud exhibit infalling with infall velocity of ~ 10 km/s rather than evaporation. The aspect of infall of the photoionized gas is also shown in Figure 3.3. In the figure, only the contracting (i.e., radial velocity $v_r < 0$) SPH particles are displayed thereby omitting the photo-evaporated particles. As shown in the left panel, we see that large part of the gas photoionized and temperature rises to $\sim 10^4$ K. As time proceeds, the compact self-shielded region forms at the center of the cloud. Also, we find the photoheated but contracting part of gas in Figure 3.3 (middle and right panel). It is worth noting that the tendency can be seen not only isotropic but also one-sided background radiation case. Therefore, kinetic energy dissipation is expected due to its thermal pressure before self-shielding occurs, and the gas cloud continues to contract to compact size without star formation.

Here, as we see in Figure 3.1, the apparent difference between one-sided and isotropic radiation is the formation of the shaded region. Since the shaded region is not affected by the UV feedback, the temperature does not rise to $\sim 10^4$ K thus the infall velocity would not be decelerated. The effect can be seen in Figure 3.2(a), the direction along with shadow. However, the profile along with the direction of y - and z -axis exhibit almost same behavior, contraction of photoheated gas can be seen in the figure. Therefore, infall of gas cloud with strong kinetic energy dissipation would be expected regardless of anisotropy of background radiation field.

In Figure 3.4 and 3.5, the evolution of the cloud of $M_{\text{ini}} = 2.5 \times 10^6 M_{\odot}$ and $z_c = 9$ irradiated by one-sided/isotropic background radiation at $z_{\text{UV}} = 10.3$ with ionizing photon number of $\dot{N}_{\text{ion}}/\dot{N}_{\text{crit}} = 10$ are shown.

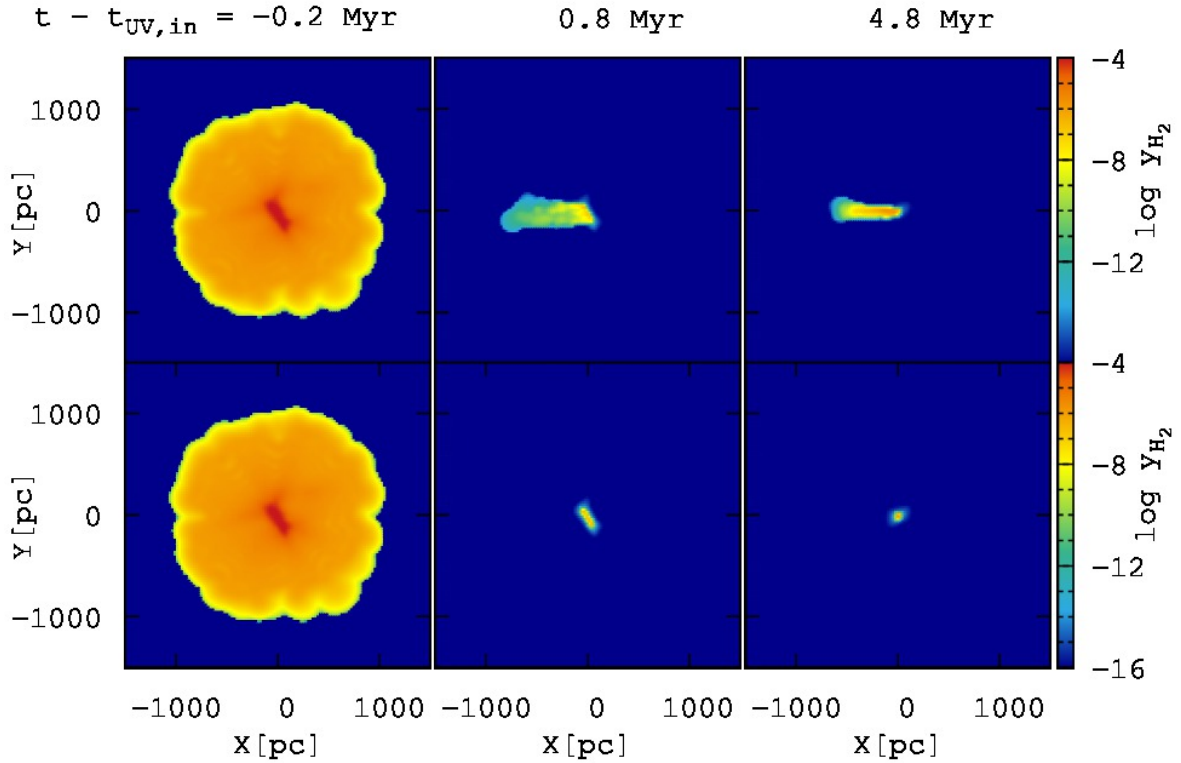
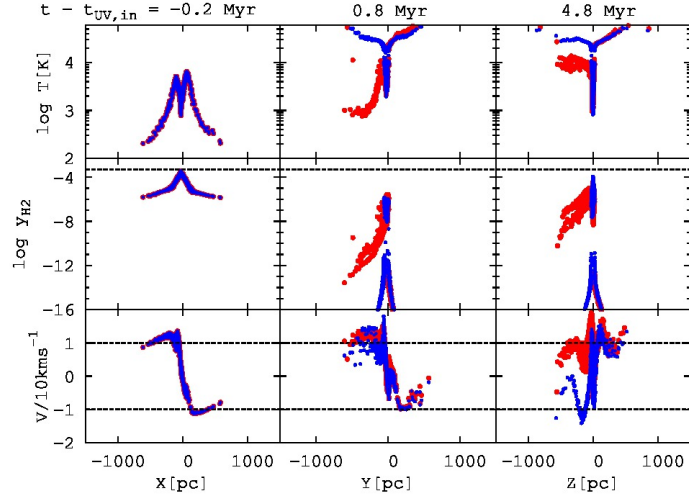
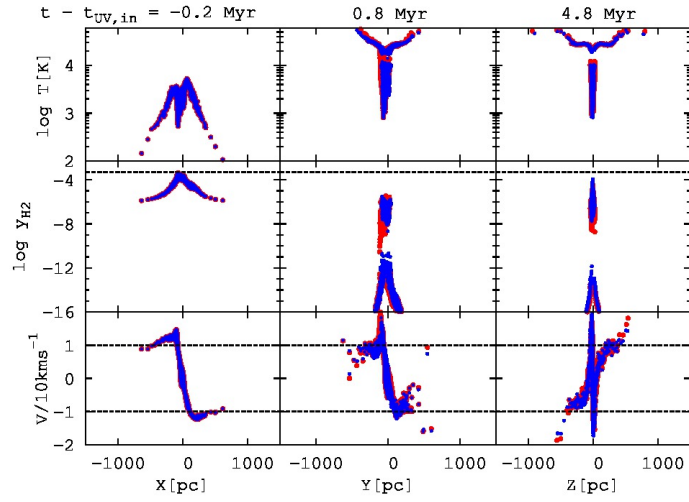


Fig. 3.4: Same as Figure 3.1, but for the case of $M_{\text{ini}} = 2.5 \times 10^6 M_{\odot}$, $z_c = 9$, and $z_{\text{UV}} = 10.3$ by one-sided and isotropic background radiation with intensity of $\dot{N}_{\text{ion}}/\dot{N}_{\text{crit}} = 10$. The left panel indicates the cloud at 0.2 Myr before irradiation while the middle and right panel show the states at 0.8 Myr and 4.8 Myr after irradiation, respectively.

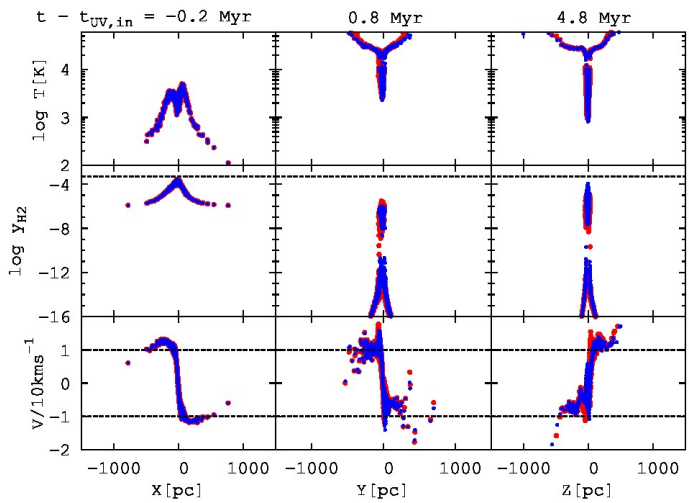
In the figures, we also see the supersonically infalling gas component as with the cloud of $5 \times 10^6 M_{\odot}$. In the right panel of Figure 3.5, at the moment of that infall velocity come up to ~ 10 km/s, we find the sufficiently cooled gas component in the central region that would be ready to form stars. As for lesser mass cloud, the more gravitational contraction is needed to reach the infall velocity of ~ 10 km/s. As a result, density evolution proceeds and sufficient amount of hydrogen molecules form at the center of the cloud. However, as we will describe below, we can expect the essence of the supersonic infall even though the some quantity of stars already formed before irradiation.



(a) The physical values on x-axis



(b) The physical values on y-axis



(c) The physical values on z-axis

Fig. 3.5: Same as Figure 3.2, but for the case of $M_{\text{ini}} = 2.5 \times 10^6 M_{\odot}$, $z_c = 9$, and $z_{\text{UV}} = 10.3$ with $\dot{N}_{\text{ion}}/\dot{N}_{\text{crit}} = 10$. From left- to right-hand side, the three panels are compatible with the time sequence of Figure 3.4.

3.1.2 Prompt Star Formation in Anisotropic Background Radiation Field

Figure 3.6 shows the hydrogen molecular distribution for the gas cloud of $5 \times 10^6 M_\odot$, $z_c = 9$. Also, the temperature T , H_2 fraction, and velocity profiles on x-, y-, z-axis are shown in Figure 3.7.

In this instance, the cloud is irradiated at an early phase of contraction ($z_{UV} = 12$, contrary to the supersonic infall case of $z_{UV} = 10.5$), infall velocity is less than 10 km/s as shown in the left panel of Figure 3.7. Therefore, photoionized gas cannot continue to contract, star cluster can only form in a weak UV intensity field owing to self-shielding effect. In Figure 3.6, since the cloud is irradiated by weak UV intensity of $\dot{N}_{ion}/\dot{N}_{crit} = 0.1$, the extensive self-shielded region is formed promptly. In Figure 3.7, we see the broad self-shielded region compared to the supersonic infall case, and the self-shielded region only continues to contract contrary to the photoionized region where eventually evaporates.

Note that, we find the anisotropy of hydrogen molecule distribution in Figure 3.6, the formation of the hydrogen molecule is more efficiently at the region face to the source rather than the center of the cloud. This behavior is caused by the increasing of electron fraction owing to photoionization. As described in equation (2.2), hydrogen molecule is formed via H^- -process. Thus, the role of the electron is a catalyst for H_2 formation in this case. The increasing of H_2 fraction encourages the shielding of Lyman-Werner band of radiation, thereby preventing the photodissociation and stars would be formed more efficiently. This effect is the positive feedback of UV background radiation, as Susa et al. (2009) have proposed ever.

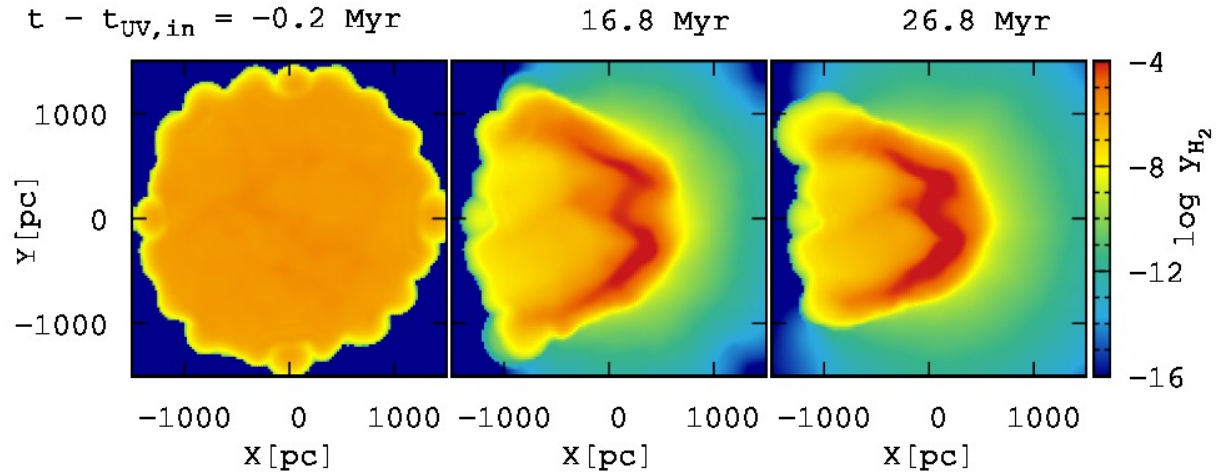
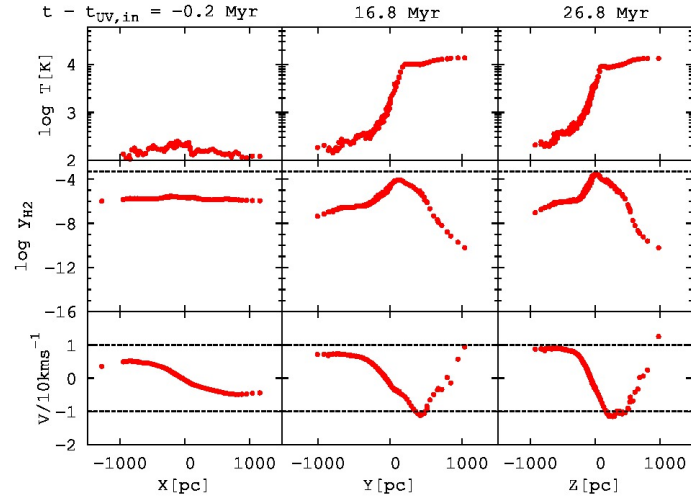
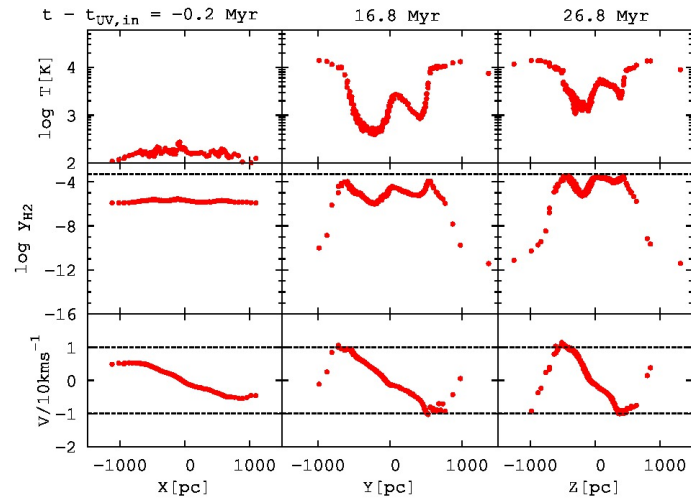


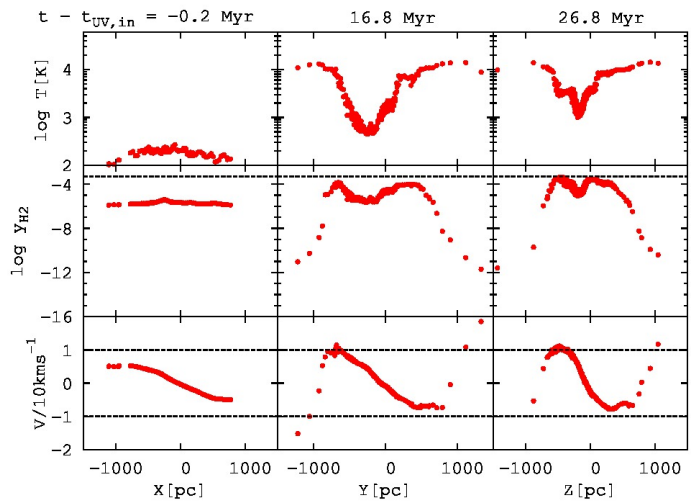
Fig. 3.6: Time evolution of the gas cloud of $M_{ini} = 5 \times 10^6 M_\odot$, $z_c = 9$ irradiated at $z_{UV} = 12$ by one-sided radiation with intensity of $\dot{N}_{ion}/\dot{N}_{crit} = 0.1$. The panels show the H_2 distribution on the x-y plane, represented in logarithmic scale as shown in the color bars. The left panel indicates the cloud at 0.2 Myr before irradiation while the middle and right panel show the states at 16.8 Myr and 26.8 Myr after irradiation, respectively. The panels show the $1500 \text{ pc} \times 1500 \text{ pc}$ region.



(a) Physical values on x-axis



(b) Physical values on y-axis



(c) Physical values on z-axis

Fig. 3.7: Same as Figure 3.2, but for the case of $M_{\text{ini}} = 5 \times 10^6 M_{\odot}$, $z_c = 9$, and $z_{\text{UV}} = 12$ with $\dot{N}_{\text{ion}}/\dot{N}_{\text{crit}} = 0.1$. From left to right hand side, the three panels are compatible with the time sequence of Figure 3.6.

3.2 Self-Shielding and Star Formation

In this section, we investigate the self-shielding and star formation procedure in the three-dimensional calculation.

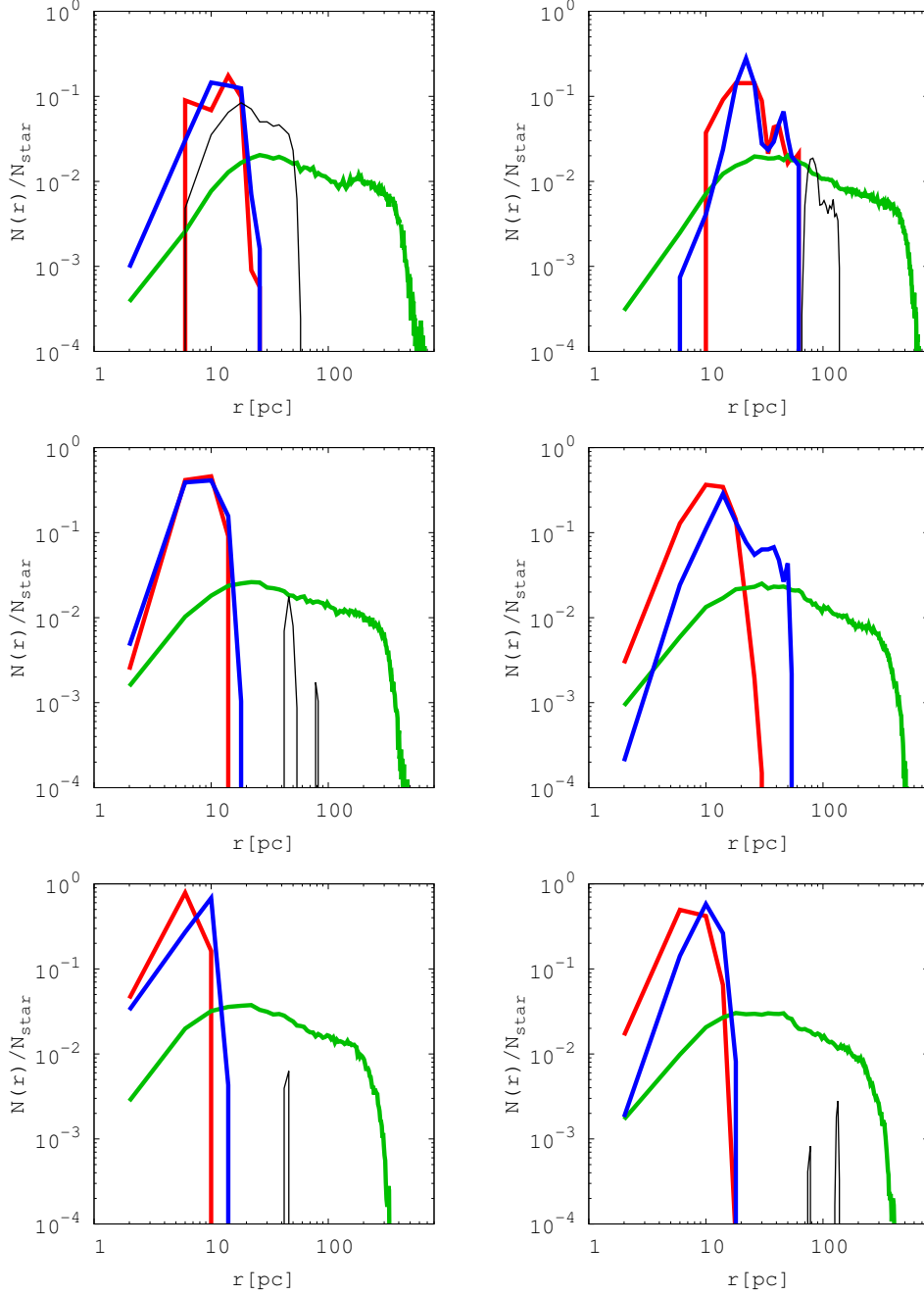
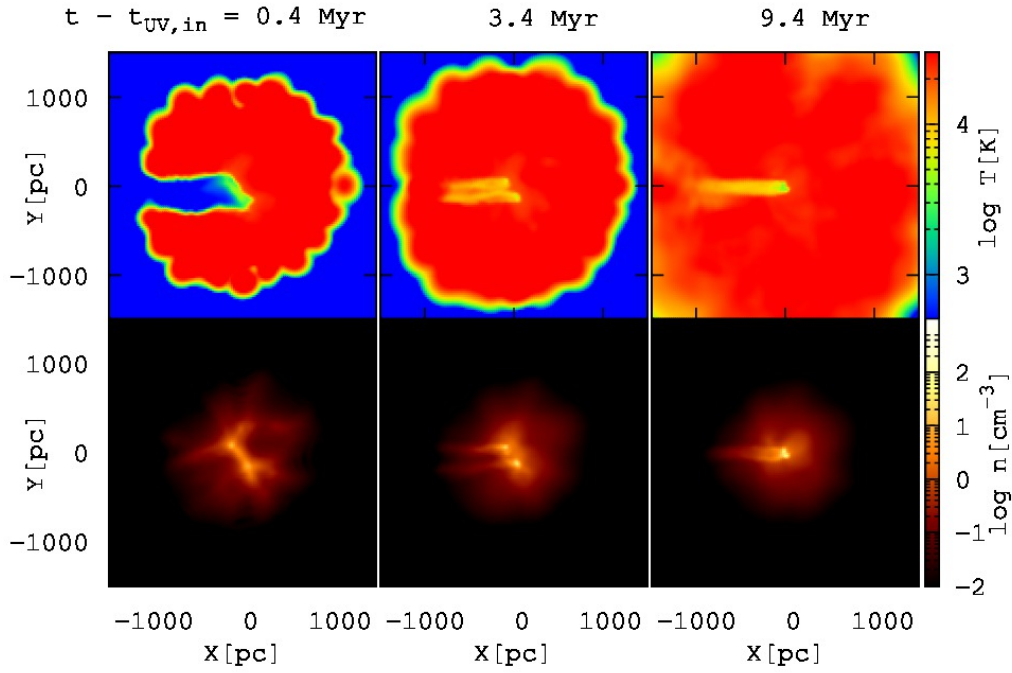
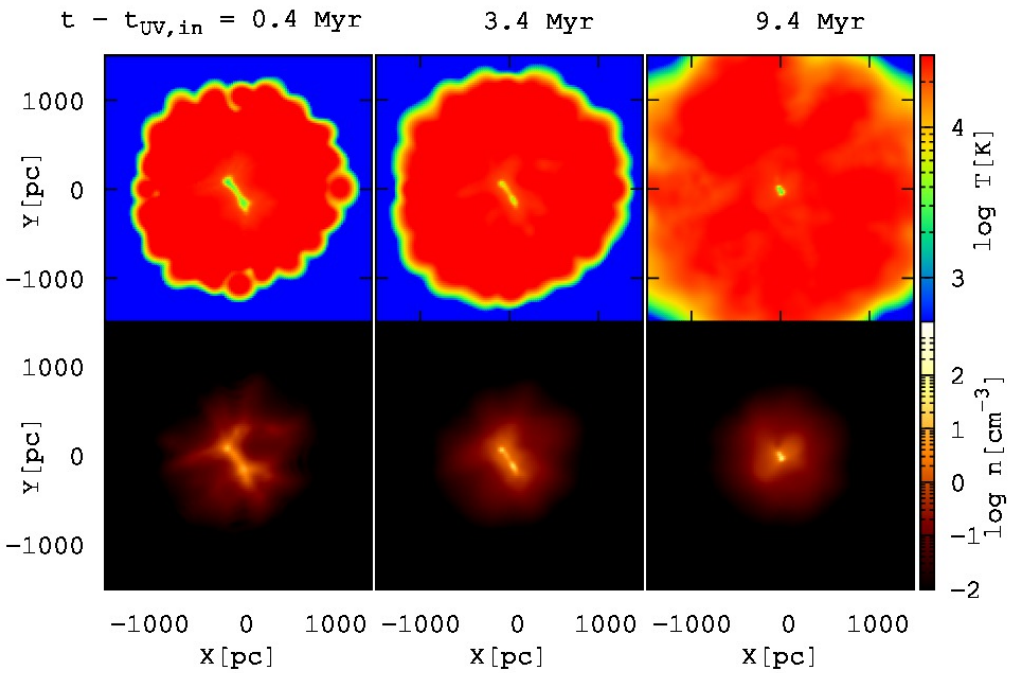


Fig. 3.8: Distribution of position where the SPH particle converted to the stellar particle. The horizontal axis denotes the distance from the center of mass of the cloud in the unit of pc. The vertical axis indicates the number count of the particle at the distance r normalized by the total number of the stellar particle. The thick red line shows the run of the supersonic infall in one-sided background radiation field while the thick blue line is the isotropic background radiation. The thick green line denotes the run of prompt star formation. The thin black line indicates the position of the particles that form star before irradiation. Upper, middle, bottom panels corresponding to the cloud of $z_c = 6, 9,$ and $12,$ respectively. Left-hand panels show the cloud of $M_{\text{ini}} = 2.5 \times 10^6 M_{\odot}$, and right-hand panels are corresponding to $M_{\text{ini}} = 5 \times 10^6 M_{\odot}$.



(a) One-sided background radiation



(b) Isotropic background radiation

Fig. 3.9: Time evolution of the gas cloud of $M_{\text{ini}} = 5 \times 10^6 M_{\odot}$, $z_c = 9$ irradiated at $z_{\text{UV}} = 10.5$ with intensity of $\dot{N}_{\text{ion}}/\dot{N}_{\text{crit}} = 10$. Colors represent the temperature T (upper) and the number density n (lower) distribution on the x-y plane for (a) one-sided and (b) isotropic background radiation field. From left-to-right-hand side, the panel corresponding to the cloud at 1.4 Myr, 5.4 Myr, and 9.4 Myr after irradiation, respectively. The panels show the $1500 \text{ pc} \times 1500 \text{ pc}$ region.

As described in the previous section, supersonic infall, i.e., contraction of photoionized gas with strong kinetic energy dissipation seems to be possible even though the background radiation is quite anisotropic, i.e., one-sided like background. However, since the ionizing structure is different between one-sided and isotropic background radiation, self-shielding procedures and resultant star formation might also be affected by three-dimension of background radiation.

Furthermore, even though the background radiation is isotropic, we find anisotropic structure owing to inhomogeneous density field of the cloud (Figure 3.1). Also in Figure 3.3, we find the filamentary-like cooled structure. According to the three-dimensional non-uniformity, the self-shielding and resultant star formation might take place in a different way from the one-dimensional calculation. In other words, it may be possible that the star formation would occur in the more broad region compared to the one-dimensional calculation. Three-dimensional density structure may also influence the compactness of the star cluster.

To confirm the question, we investigate the position where the SPH particle converted to the stellar particle for each run. Figure 3.8 shows the position distribution where stellar particles were born. As clearly seen in the figure, the distribution is sharply different from supersonic infall and prompt star formation.

In the case of prompt star formation, star formation takes place over the course of $\gtrsim 100$ pc. Although the most efficient position for star formation is ~ 10 pc from the center, the fraction accounts for less than 10 percent, and the distribution smoothly distributed. Since the background radiation intensity is weak, broad self-shielded region forms promptly, thus star formation cover much territory of the cloud. Furthermore, as described in the previous section, the positive feedback of the UV radiation, i.e., efficient H_2 formation also induces the vast area of star formation.

On the other hand, in the case of supersonic infall, the distribution have the peaky shape compared to prompt star formation. The most powerful position for star formation is ~ 10 pc from the center and the fraction account for $\gtrsim 10$ percent. Hence, the most of the stars are formed within a compact region of ~ 10 pc. It should be noted, although the ionizing structure for one-sided background radiation differs from isotropic one, the position distribution for one-sided case exhibits similar way with isotropic background case. This tendency seems to contrary to the intuitive expectation. That is to say, since shaded region forms in the case of one-sided radiation, the star-forming region is thought to be the not so compact as well as the isotropic case. To make sure the reason, the time evolution of temperature of the cloud on x-y plane appears in Figure 3.9. In fact, although the shaded region promptly formed in the case for one-sided background radiation, the photoionized gas comes around behind the shadow as time goes on. Consequently, the star-forming region tends to be compact similar to isotropic radiation case.

Note that, in supersonic infall of the cloud $M_{\text{ini}} = 2.5 \times 10^6 M_{\odot}$, $z_c = 6$ (top-left panel of Figure 3.8), the non-negligible amount of star, say, about one-half of the final stellar mass have already formed before irradiation. However, the position of the star formation formed via supersonically infalling gas tends to be the more inner region of the cloud than UV-free gas component. Because of strong UV intensity and sufficiently large infall velocity, gas continues to contract without star formation. Once sufficiently contacted, a compact region is self-shielded against UV and stars begin to form. As a result, star formation starts at more interior region than the UV-free case. That is to say, the distributions are just evidence for the supersonic infall branch proposed by Hasegawa et al. (2009). In addition to that, we also find that the distribution of prompt star formation is more diffusive that UV-free case. This is caused by the positive-feedback of UV background radiation. These results suggest that the size of the star cluster formed in the UV background radiation may be significantly regulated by the property of the radiation.

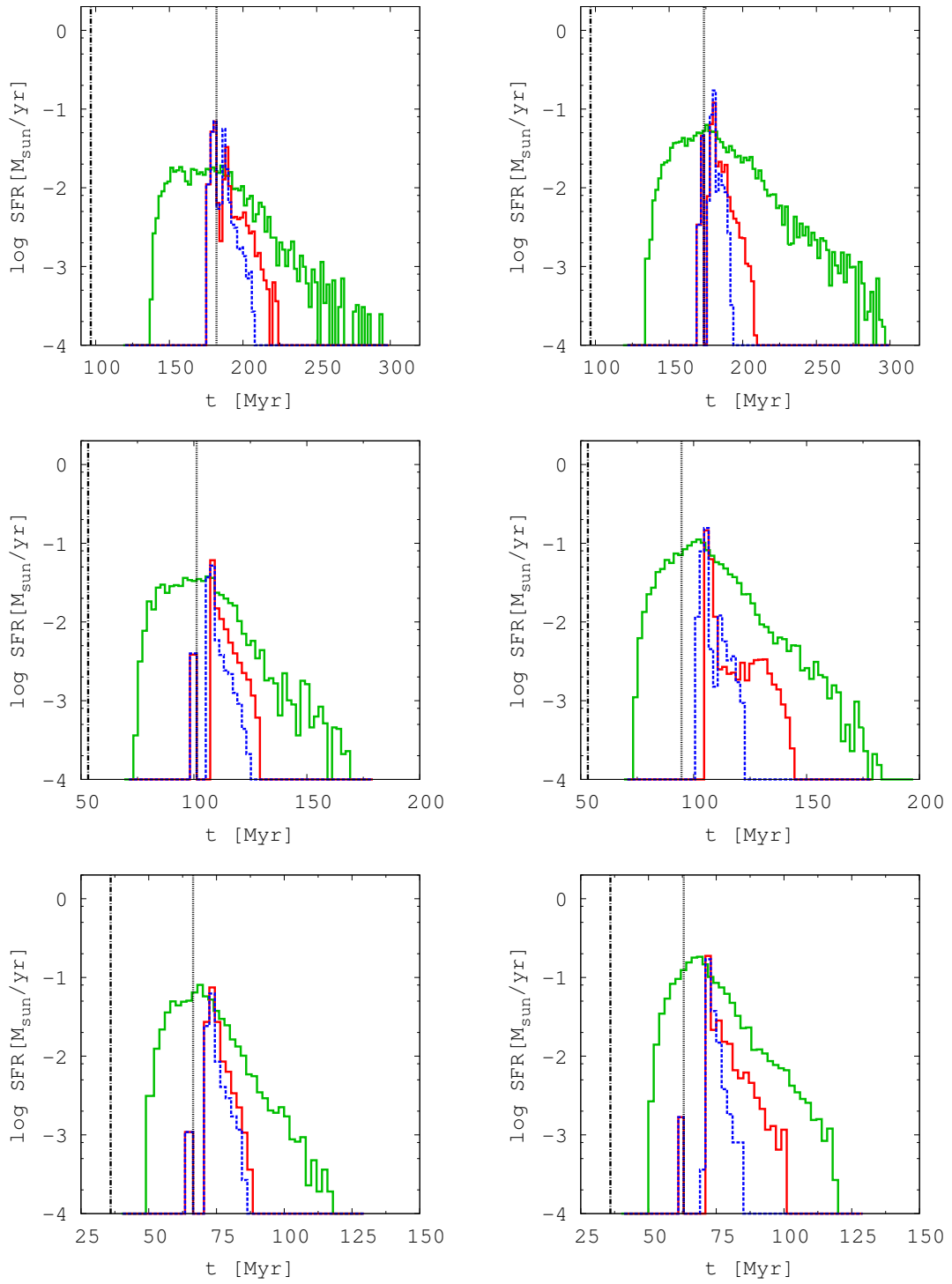


Fig. 3.10: Star formation history of the star cluster formed via supersonic infall and prompt star formation. The horizontal axis denotes the time in the unit of Myr, and the vertical axis is the star formation rate in the unit of M_{\odot}/yr . The thick red line indicates the run of supersonic infall in one-sided background radiation field while the thick blue line is the isotropic background radiation. The thick green line denotes the run of prompt star formation. The vertical dash-dotted and dotted line denotes the epoch of irradiation for prompt star formation, and supersonic infall, respectively. Left-hand panels show the cloud of $M_{\text{ini}} = 2.5 \times 10^6 M_{\odot}$, and right-hand panels are $M_{\text{ini}} = 5 \times 10^6 M_{\odot}$.

Figure 3.10 shows the star formation rate (SFR) of the clusters formed via supersonic infall and prompt star formation.

As we see in the figure, stars begin to form at an early phase of contraction in the case of the prompt star formation. This is because of both prompt self-shielding and efficient H_2 formation due to UV background radiation. Besides, star formation continues to order of ~ 100 Myr with inactive star formation rate. That is, a large amount of gas is converted into stars slowly, this may be inconsistent with the typical single stellar population of GCs. Note that, if we compare the SFR regarding the given z_c (comparing the left-panel with the right panel), the peak SFR exhibits higher value with increasing the initial mass of the cloud. For each cloud, since initial mean density is same, the dynamical time of the cloud is also identical. Therefore, the higher the initial mass of the cloud the higher the SFR that interpreted.

As for star cluster formed via supersonic infall, the star-forming duration is the order of 10 Myr, which might be reasonable to give the explanation for the single population of GCs. We see from Figure 3.10, SFR for isotropic background radiation decreases quickly after peak compared to one-sided one, because gas around the self-shielding region evaporates, inhibiting continual star formation there. On the other hand, owing to shadowing effect, infalling gas component barely remains for one-sided background radiation. Consequently, SFR can be affected by the anisotropy of background radiation though the impact is not so crucial.

3.3 Stellar Dynamics

In the previous section, the contraction and self-shielding procedure in three-dimensional UV background radiation are shown. In particular, we have shown that the supersonic infall proposed by Hasegawa et al. (2009) seems to be possible regardless of three-dimension in terms of background anisotropy and/or inhomogeneous density field. In this section, we pursue the stellar dynamics and evaluate the impact of background radiation on a final state of the star cluster.

3.3.1 Mass Distribution and Stellar Density Profile

Figure 3.11 shows the resultant stellar and DM mass distribution for both prompt star formation and supersonic infall. Clearly, the stellar distribution formed via prompt star formation differs from supersonic infall one, contrary to that the DM components show a similar profile. These profiles are thought to reflect the contraction process of gas cloud as we have seen in the previous section. The prompt star formation branch converts the gas into the stellar particle at an early phase of cloud contraction. Namely, stars are formed from the gas component that insufficiently dissipates the infall kinetic energy owing to thermal pressure. Consequently, diffuse, DM-dominated star cluster tends to be formed. On the other hands, in the case of supersonically infalling gas cloud with strong UV background radiation field, strong kinetic energy dissipation before forming stars can be expected. Moreover, stars begin to form at a compact self-shielded region owing to the intensity of radiation. As a result, compact stellar dense cluster remains at the center of the DM halo.

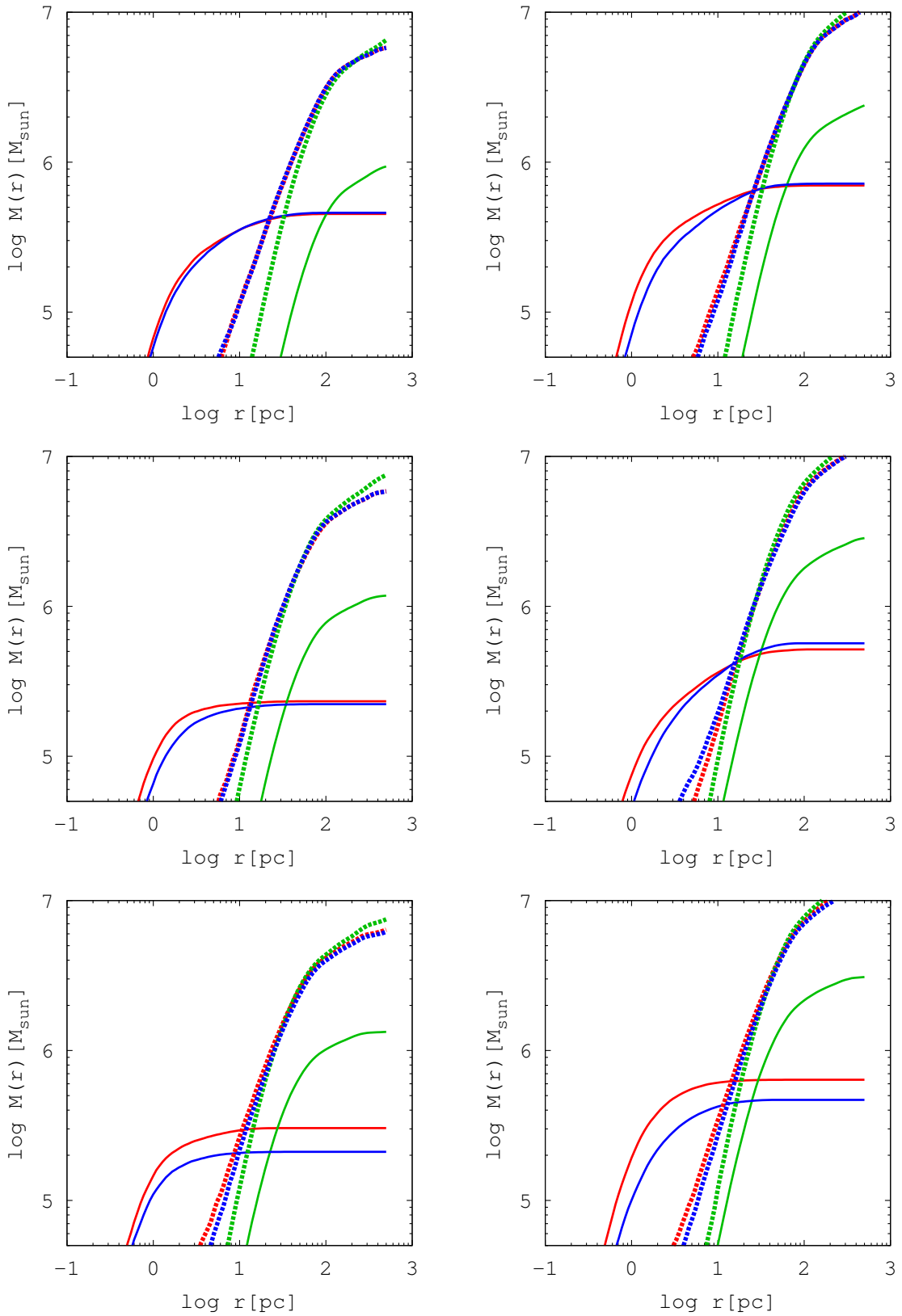


Fig. 3.11: Mass distribution of stellar and DM component. The horizontal axis denotes the distance r from the stellar density peak in the unit of pc. The vertical axis indicates the cumulative mass contained within r . Red line shows the run of supersonic infall in one-sided background radiation field, while the blue line is the isotropic background radiation. Green line denotes the run of prompt star formation. Solid line indicates stellar component while dotted line denotes DM component. Left-hand panels show the cloud of $M_{\text{ini}} = 2.5 \times 10^6 M_{\odot}$, and right-hand panels are $M_{\text{ini}} = 5 \times 10^6 M_{\odot}$.

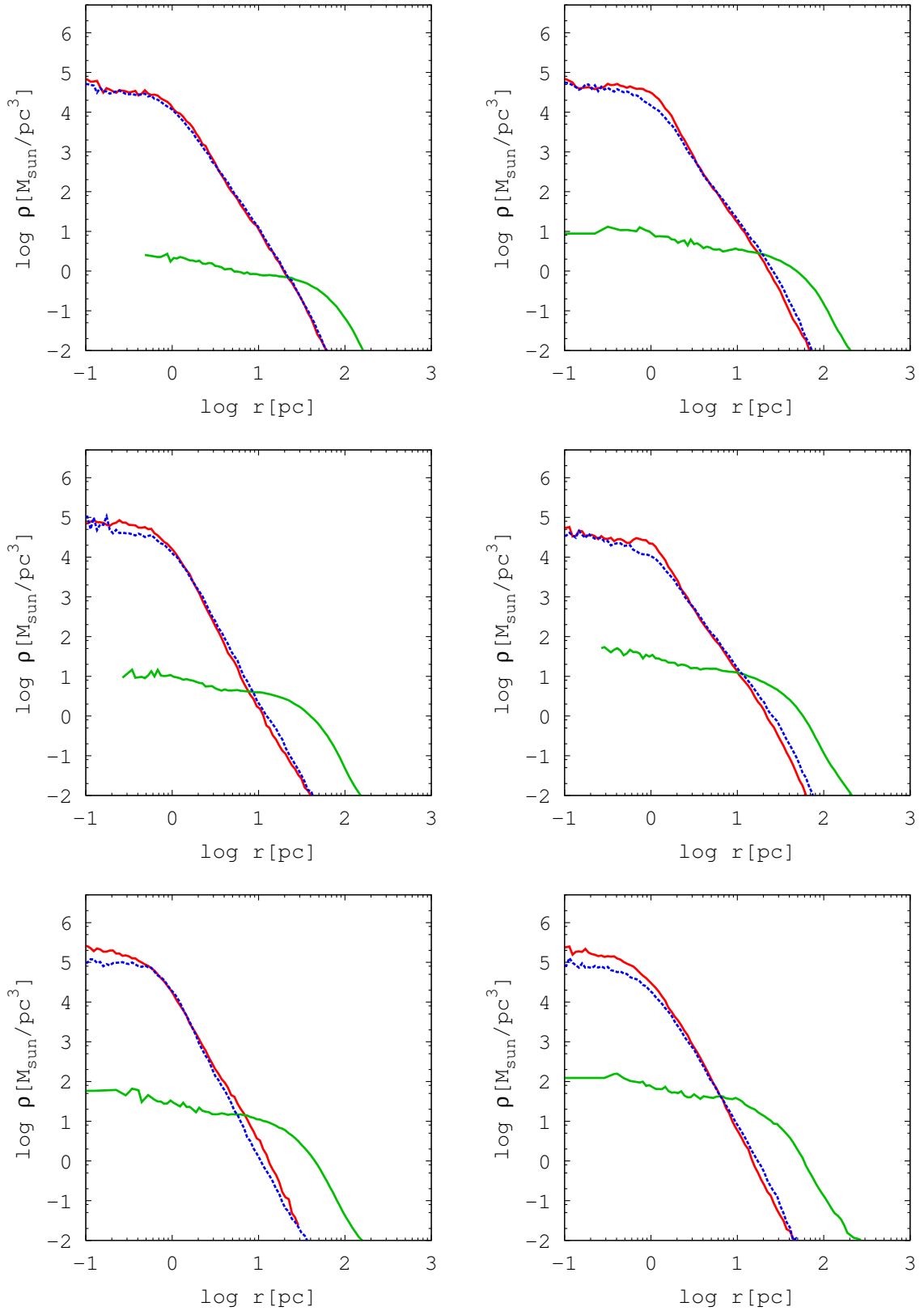


Fig. 3.12: Density profile for the stellar component. The horizontal axis denotes the distance from the stellar density peak in the unit of pc. The vertical axis indicates the stellar density. Red line shows the run of supersonic infall in one-sided background radiation field while the blue line is the isotropic background radiation. Green line denotes the run of prompt star formation. Left-hand panels show the cloud of $M_{\text{ini}} = 2.5 \times 10^6 M_{\odot}$ and the right-hand panels are $M_{\text{ini}} = 5 \times 10^6 M_{\odot}$.

Figure 3.12 shows the stellar density profile for both prompt star formation and supersonic infall in one-sided and isotropic background radiation.

As we see in the figure, star clusters formed via supersonic infall exhibit higher central stellar density ($\gtrsim 10^4 M_\odot \text{pc}^{-3}$) which are similar to one of GCs. Contrary to that, clusters formed via prompt star formation reach only $\sim 10^{1-2} M_\odot \text{pc}^{-3}$. Now we can determine the core radius of the clusters. Usually, observed GC density profile is fitted by assuming King model. However, we do not consider the tidal field in the simulation. Hence, we can not determine the outer limit radius (tidal radius). Thus, we fit the each stellar density profile by assuming the Plummer-model and identify the core radius as the Plummer scale length b . The Plummer model density profile is given by

$$\rho(r) = \frac{3M_*}{4\pi b^3} \left(1 + \frac{r^2}{b^2}\right)^{-5/2} \quad (3.1)$$

where M_* denotes the total stellar mass of the cluster. We adopt the simple least-square approach for fitting procedure. The resultant core radii for all our clusters are listed in Table 3.1.

We see from Table 3.1 that there is no cluster exhibits a core radius $\lesssim 1$ pc for prompt star formation case, while observation appears to show the core radii $\lesssim 1$ pc for GCs (Kormendy 1985). On the other hand, star cluster formed via supersonic infall seems to agree with the observed value.

Here, we roughly estimate the central velocity dispersion σ_0 for both supersonic infall and prompt star formation as

$$\sigma_0 \sim \sqrt{\frac{GM_{\text{core}}}{r_{\text{core}}}} \quad (3.2)$$

For supersonic infall, the core radius (Plummer's b) and stellar mass included within the core distribute around ~ 1 pc and $10^5 M_\odot$. Thus, the velocity dispersion may come up to ~ 10 km/s. On the other hand, as for prompt star formation, the typical core radius seems to be several times 10 pc, though the core masses are not so significantly different with supersonic infall, with a certainty factor of difference at the most. As a result, the velocity dispersion may be $\lesssim 10$ pc. However, it should be noted that the estimation of prompt star formation may exhibit lower than the actual value because the contribution of DM component is not considered in the estimation. As seen in Figure 3.11, since star cluster formed through the prompt star formation tend to be a DM-dominated cluster, the stellar velocity dispersion is thought to be determined by DM. Consequently, the M_{core} in the estimation would be deficient, and the velocity dispersion is considered to be indeed higher value.

Finally, as for prompt star formation, the final fraction of the total stellar mass with respect to an initial gas mass tends to slightly, but systematically increase with increasing the initial gas mass. Naively, it is anticipated that the fraction may be independent of the initial mass since ionizing photon number incident on the clouds are set to be same as 0.1, in other words, fraction of the shielding region is independent of the mass. The tendency is thought to be caused by the difference of the column densities which is the parameter for photodissociation rate for hydrogen molecule (equation 2.66). For each cloud, since the irradiation epoch is set to be same on any given z_c , the mean density of each cloud is same at the phase of irradiation. Then, the distance from the surface which corresponding to the column density required to shielding the dissociation photons is independent of the mass of the cloud. On the other hand, the radius of the cloud depends on the mass as $M^{1/3}$. As a result, the fraction of star forming region with respect to total volume increases with increasing the initial mass.

Table. 3.1: The core radius of our clusters

z_c	M_{ini} [$10^6 M_\odot$]	b [pc]	M_{core}^1 [$10^5 M_\odot$]	M_*/M_{ini}^2	b [pc]	M_{core} [$10^5 M_\odot$]	M_*/M_{ini}	b [pc]	M_{core} [$10^5 M_\odot$]	M_*/M_{ini}
		supersonic/one-sided			supersonic/isotropic			prompt star formation		
6	2.5	1.35	1.03	0.181	1.44	1.05	0.184	54.2	1.93	0.397
6	5.0	1.48	1.83	0.140	1.57	1.43	0.144	46.9	5.04	0.530
9	2.5	0.867	0.750	0.0930	0.925	0.542	0.0890	33.6	2.36	0.487
9	5.0	1.47	1.12	0.103	1.64	0.906	0.11	29.3	4.82	0.595
12	2.5	0.68	0.871	0.121	0.749	0.651	0.0844	22.4	2.46	0.546
12	5.0	0.912	1.67	0.128	1.08	1.07	0.0937	22.1	5.31	0.642
9	1.0	-	-	-	-	-	-	33.2	0.584	0.317
9	10.0	1.68	2.93	0.204	-	-	-	25.7	8.41	0.693
12	1.0	-	-	-	-	-	-	22.0	0.711	0.407
12	10.0	1.24	3.54	0.300	-	-	-	-	-	-

¹ stellar mass included in core radius b normalized by $10^5 M_\odot$

² final total stellar mass to initial gas mass ratio

3.4 Comparison to Observations

As we see in the previous section, the property of the star cluster is strongly affected by the external background radiation. In this section, we try to compare our clusters to observations. To do that, the V-band magnitude M_V of our clusters are derived by assuming the typical mass-to-light ratio for GCs as $M_{\text{GC}}/L_V = 2$ (Pryor & Meylan 1993). Hence, we assume the V-band luminosity of the clusters as

$$\frac{L_V}{L_\odot} = 0.5 \frac{M_*}{M_\odot} \quad (3.3)$$

Therefore, the absolute V-band magnitude of the cluster is given by

$$M_V = -2.5 \log_{10} \frac{L_V}{L_\odot} + 4.72 \quad (3.4)$$

Figure 3.13 shows the resultant half-mass radii r_h as a function of M_V . Also, the observations for GCs, dSphs, and UCDs are plotted in the figure. As we see in the diagram, the star cluster formed through the supersonic infall distribute $r_h \sim 1$ -10 pc, which is consistent with the observation of GCs. This result can be interpreted as their compactness of star-forming regions as well as kinetic energy dissipation at the gas phase of the cloud. As seen in Figure 3.8, the large amount of star formation takes place within ~ 10 pc region for supersonic infall case. Besides, it does not strongly depend on the initial mass of the cloud. The result implies that the strong UV background radiation might be the key to representing the observed feature of the half-mass radius of GCs. i.e., r_h is almost independent of M_V .

Contrary to supersonic infall, there is no star cluster to represent the GC-size half-mass radius for prompt star formation case, rather likely to represent dSphs. The half-mass radii distinct from the supersonic infall one with an order of magnitude at the similar M_V .

In addition to the half-mass radius, we compare the mass-to-light ratio of the clusters, M_{dyn}/L_V . As for the dynamical mass M_{dyn} , we define the total mass within the half-mass radius $M_*(r < r_h) + M_{\text{DM}}(r < r_h)$. The resultant mass-to-light ratio vs. absolute V-band magnitude appears in Figure 3.14.

We find that the mass-to-light ratio for supersonic infall case distributes as well as observed GCs. Again, the prompt star formation cases are separated from GCs. Since the star cluster formed through the prompt star formation is the DM-dominated system (Figure 3.11), it seems to belong to a sequence of dSphs.

In Figure 3.15, we show the central velocity dispersion σ_0 of our clusters as a function of M_V . Obviously, star clusters formed via supersonic infall represents the higher velocity dispersion regarding the M_V than prompt star formation. The higher velocity dispersion can be interpreted as the strong kinetic energy dissipation at the phase of infalling gas. The resultant σ - L relation seems to consistent with the result of one-dimensional RHD calculation obtained by Hasegawa et al. (2009), as shown in Figure 1.11. It should be emphasized again that the outcome is not affected by the anisotropy of background radiation. As for prompt star formation, although the velocity dispersions reach ~ 10 km, they are DM-dominated clusters and the velocity dispersion may be determined by dark matter rather than stars (Figure 3.13, 3.14). Thus, the points tend to locate on the right-hand side in the diagram at any given velocity dispersion compared to supersonic infall.

Here, we mention the observation relation $\sigma \propto L^{1/2}$ for GCs. According to virial theorem, the velocity dispersion is related to the total mass M and half-mass radius r_h as

$$\sigma \sim \sqrt{\frac{GM}{r_h}} \quad (3.5)$$

If we assume $M \propto r_h^3$ and $L \propto M$, the relationship $\sigma \propto L^{1/3}$ is obtained. Actually, the σ - L distribution for the star cluster formed via prompt star formation seem to obey the relation, since the star clusters are formed through a simple gravitational contraction of the self-shielded part of the cloud.

The relation $\sigma \propto L^{1/2}$ might be obtained if the size of the system is almost independent of the mass. In fact, the size of the cluster is significantly regulated by the external radiation according to our numerical model. In particular, only the supersonic infall model can represent the star cluster formation that forms a similar size of clusters regardless of its mass (see Figure 3.8). Also, kinetic energy dissipation of the gas would effectively act in the direction of preventing the cluster from diffusing, but would rather retain the stars within a compact region. Consequently, the star clusters formed via supersonic infall may reproduce the relation of $\sigma \propto L^{1/2}$ within the range of variance of $r_h \sim 1$ -10 pc.

Eventually, the star clusters are sharply distinguished in the diagrams, and the features are regulated by the background radiation, as indicated by (Hasegawa et al. 2009). What needs to be emphasized here is the fact that the result is obtained by three-dimensional numerical simulations, i.e., the anisotropy of background radiation, inhomogeneous density structure of the cloud, local self-shielding, and star formation are taken into account. As a result of comparison with the observation, star clusters formed via supersonic infall seems to be in good agreement with observation. Thus, supersonic infall is no less a possible channel to form star clusters comparable in size to GCs regardless of anisotropy of the background radiation field.

Note that, our clusters of supersonic infall do not cover the all of the observed GCs regarding M_V . The possibility of the supersonic infall depends on the initial mass of the cloud since the infall velocity is proportion to the mass. In other words, as for low-mass cloud, sufficient contraction is needed to reach the supersonic infall velocity of photoionized gas $\gtrsim 10$ km/s. On the other hand, such a sufficient contraction induce the star formation, thereby forming a large amount of the stars before supersonic infalling. In our parameter set, the cloud mass of $M_{\text{ini}} = 10^6 M_\odot$ is corresponding to the case. Nevertheless, low-mass side of the cluster is possible to appear by considering the mass loss due to tidal stripping, evaporation by two-body relaxation, and stellar evolution.

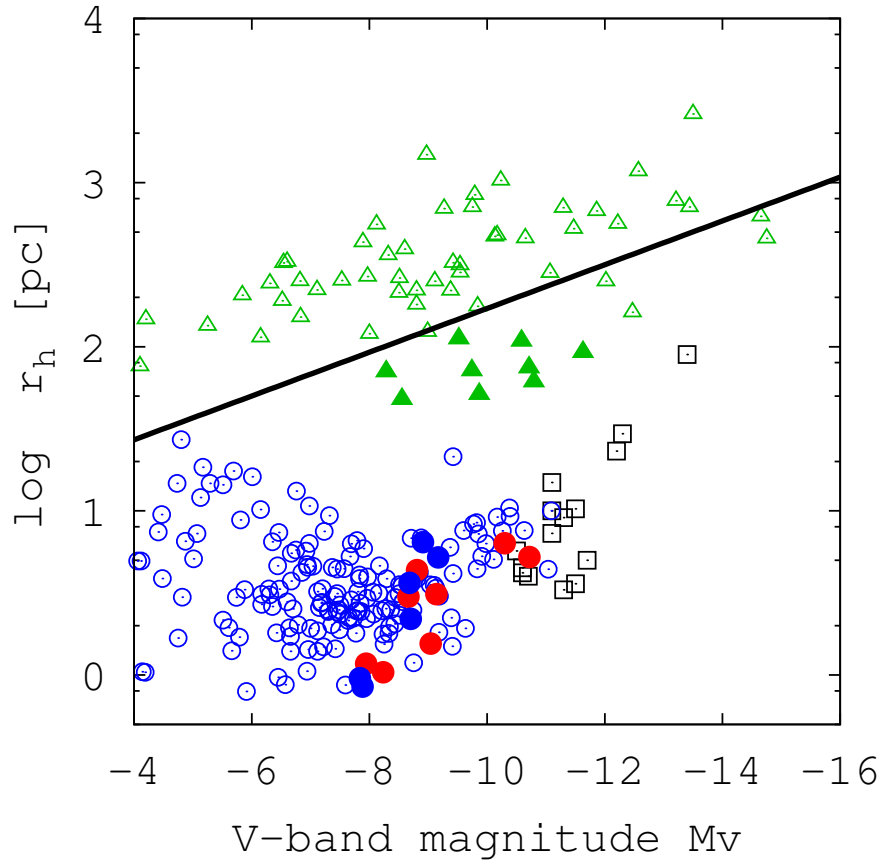


Fig. 3.13: Half-mass radii r_h as a function of absolute V-band magnitude M_V . Filled-red, -blue circles indicate the star clusters formed through supersonic infall in one-sided and isotropic background radiation, respectively. Filled-green triangles are star clusters formed via prompt star formation. Open symbols denote the observation; circles, triangles, squares are corresponding to GCs, dSphs, and UCDs, respectively. The observation data for GCs are taken from MW GCs catalog of (Harris 1996) and NGC 5218 GCs (Martini & Ho 2004). The observation for dSphs are taken from McConnachie (2012). As for UCDs, the data are taken from Drinkwater et al. (2003) and Mieske et al. (2008). The thick solid line indicates the relation of $\sigma \propto L^{1/3}$.

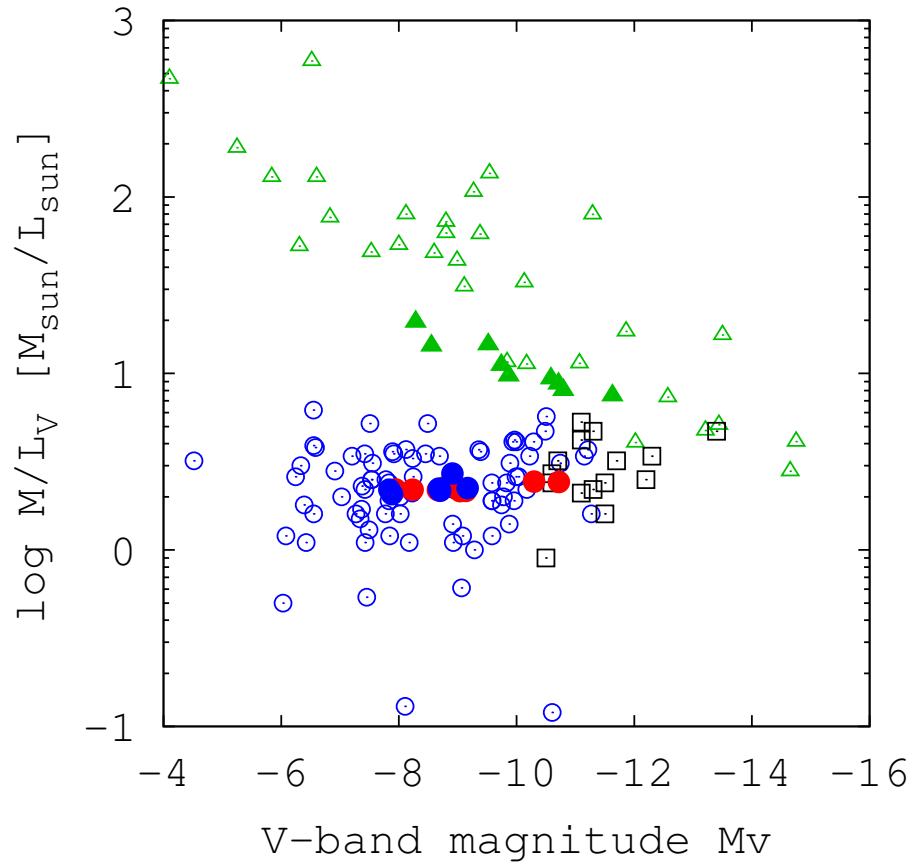


Fig. 3.14: Mass-to-light as a function of absolute V-band magnitude M_V . The symbols indicate same as Figure 3.13. The observation data for GCs are taken from MW GCs, LMC GCs, SMC GCs, Fornax GCs, NGC 5218 GCs, and M31 GCs, compiled by Kenji Hasegawa (Hasegawa et al. 2009). The observation data for dSphs are taken from McConnachie (2012). As for UCDs, the data are taken from Drinkwater et al. (2003) and Mieske et al. (2008).

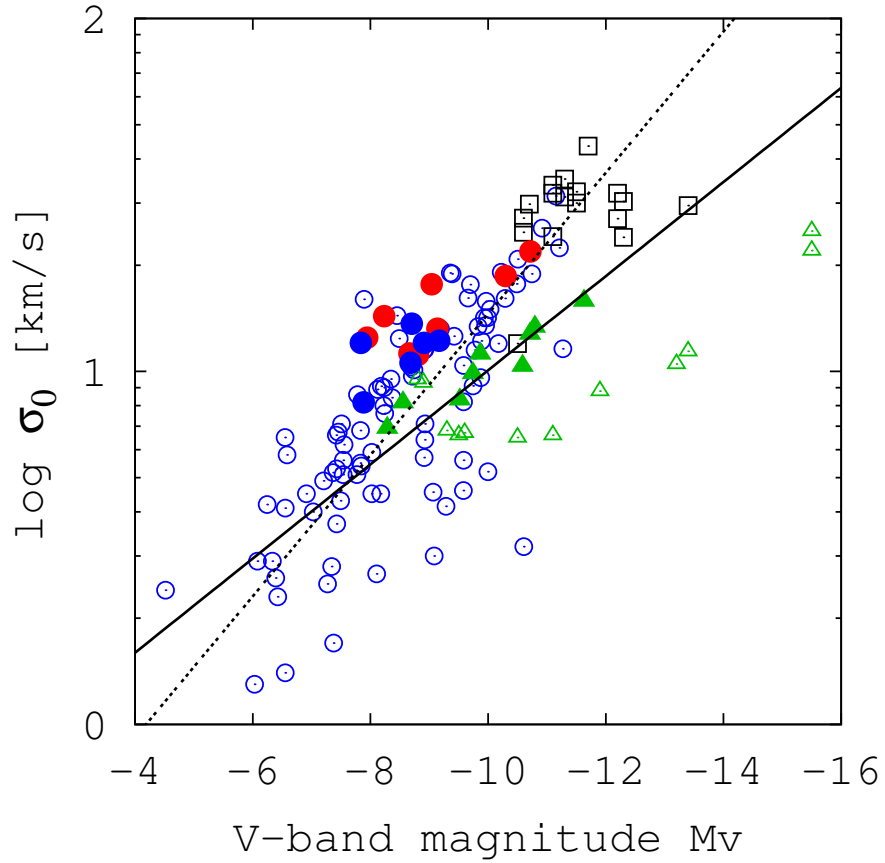


Fig. 3.15: Central velocity dispersion as a function of absolute V-band magnitude. The symbols indicate same as Figure 3.13. The observation data of GCs and UCDs are identical to Figure 3.14. The observation data of dSphs are taken from Mateo (1998). Dotted line represents the relation of $\sigma \propto L^{1/2}$ derived by Håegem et al. (2005). The solid line indicates the relation of $\sigma \propto L^{1/3}$.

Chapter 4 Discussion

4.1 Formation Site of GCs Based on Our Model

In our numerical simulations, the supersonic infall, i.e., supersonically contraction of photoionized gas in strong UV background radiation can form a compact star cluster as well as GCs. Here, we consider the site of old GC formation from our results.

Table 2.1 summarizes the J_{21} of each cloud. As seen the table, the typical value of J_{21} is $\sim 10^{2-3}$, thus, sufficiently strong background radiation is predicted as a condition of GC formation. There may be several possible candidates for such strong UV source in an early universe.

First, we consider the Population III (Pop III) object as the source. Theoretically, a Λ CDM cosmology predicts the priority collapse of low-mass DM mini-halo of $\sim 10^6 M_\odot$ at the very early epoch of $z \sim 20 - 30$ that would evolve into Pop III objects (e.g., Yoshida et al. 2003). Typically, Pop III star is considered to be a massive star. If we assume the stellar mass as $100 M_\odot$, the effective temperature and ionizing photon number per second become to be 10^5 K and 10^{50} s^{-1} (Schaerer 2002). Hence, the emission of strong UV is expected at near the Pop III object. Hasegawa et al. (2009) have argued that the expected intensity emitted by the Pop III star as a function of distance from the source r . The effective intensity of the Pop III object at the distance r is given by

$$I_\nu(r) = B_\nu(T_{\text{eff}}) \left(\frac{r_*}{r} \right)^2 \quad (4.1)$$

where r_* denotes the radius of Pop III star.

According to their estimation, considerable minimum distance is determined as the virial radius of the Pop III objects for given mass. Assuming the total mass of the Pop III object as $M = 10^6 M_\odot$ that collapses at $z = 20$, they have found the resultant intensity as $J_{21} \sim 10^3$. The value is consistent with our parameter set. However, it should be noted that recent theoretical work has revealed that the characteristic mass of the Pop III star shift to lower as decreasing the redshift (Hirano et al. 2015). The evolution of Pop III mass spectrum arises due to the difference in the cooling procedure of the primordial gas (main coolant is hydrogen molecule at $z > 20$, but both H_2 and HD at $z \lesssim 15$). At $z \lesssim 15$, the mass spectrum of the Pop III star express the two peaks at a few $\times 10 M_\odot$ and $\sim 100 M_\odot$. The decreasing of the mass affect the expected intensity. In fact, if we suppose the Pop III star mass of $25 M_\odot$, the ionizing photon number is $5.4 \times 10^{48} \text{ s}^{-1}$ (Schaerer 2002). The effective temperature is 7×10^4 K and expected intensity become a lower factor of ~ 2 . Also, the radius of the Pop III star also decreases. Moreover, lower redshift increases the virial radius since it is proportion to the collapse redshift. As a result, if we consider the Pop III star formed at $z = 10$, the resultant intensity is thought to be reduced to $J_{21} \sim 10$. Nevertheless, above estimation have assumed that one Pop III star would be formed at the halo. If more than one stars form in the halo, the resultant expected intensity increases in proportion to the source number.

On the other hand, the young star forming dwarf galaxies are also the source of background radiation at the high- z universe. Such a galaxies, i.e., highly star-forming small galaxy in the early universe, Lyman α emitters (LAEs) are considered to be the plausible candidates. The SFR for LAE have considered as $1-10 M_\odot/\text{yr}$, and the typical Ly α luminosity exhibits $\sim 10^{42} \text{ erg s}^{-1}$, hence, strong UV background radiation can be expected. Recent theoretical work has suggested the emissivity of ionizing photon as a function of Ly α luminosity (Yajima et al. 2014). According to their study, the ionizing photon number of $\sim 10^{52} \text{ s}^{-1}$ is

expected at the $L\alpha$ luminosity of $\sim 10^{42} \text{ erg s}^{-1}$. If we suppose the typical size of the LAE as $\sim 1 \text{ kpc}$ (Pirzkal et al. 2007), the upper limit of the ionizing photon number flux becomes to be $\sim 10^8 \text{ photons cm}^{-2} \text{ s}^{-1}$. Table 4.1 shows the parameters of background radiation for supersonic infall case in this study. Therefore, it seems to be difficult to realize the ionizing photon flux predicted in our numerical model nearby the LAEs unless the sources are highly clustered and isotropically distributed around the cloud.

The another candidate of the strong external source is the active galactic nuclei (AGNs), which may be corresponding to the quite anisotropic background radiation field. The recent observation of Planck Collaboration et al. (2015) has reported that the cosmic reionization epoch of $z_r = 8.8_{-1.4}^{+1.7}$. The value is quite lower compared to previous works (e.g., Hinshaw et al. 2013; Planck Collaboration et al. 2014). In the traditional view, the contribution of luminous quasars to the cosmic reionization peaks at $z \sim 3$ and inactive at the more high- z universe. At $z > 3$, the primary source is thought to be the young star forming galaxies. However, the delay in completing the reionization suggests that the inactivity of the high- z source as ever considered, i.e., the contribution of the ionizing photons emitted from star-forming galaxy might be weak. In addition to that, recent works have revealed the shape of luminosity function for quasar and faint AGN at the high- z universe. As a consequence, the role of AGNs seems to be significant regarding the cosmic reionization than ever predicted before (Glikman et al. 2011; Giallongo et al. 2015; Madau & Haardt 2015). The candidates of such faint AGNs exhibit the typical luminosity of 10^{43} erg/s in the range of 2-10 keV (Giallongo et al. 2015). If the simple power-law luminosity formula as $L_\nu \propto \nu^{-1}$ is assumed, we can roughly evaluate the ionizing photon number \dot{N}_{ion} emitted by the AGN as

$$\dot{N}_{\text{ion}} = \int_{\nu_L}^{\infty} d\nu \frac{L_\nu}{h\nu} \sim 3 \times 10^{53} \text{ s}^{-1} \quad (4.2)$$

Therefore, the ionizing photon number flux of $\sim 10^9 \text{ photons cm}^{-2} \text{ s}^{-1}$ is obtained at the distance of 1 kpc from the source. We find in Table 4.1 that the evaluated value is consistent with the one-sided supersonic infall calculations. Note that, the GGCs distribute around $\sim 1\text{-}10 \text{ kpc}$ from the galactic center (e.g., Schiavon et al. 2005). This fact is curious consistency with our results. If we suppose the luminous quasar as a source, the required flux can be obtained at a more distant place.

Table. 4.1: The parameters of background radiation for supersonic infall

z_c	z_{UV}	M_{ini} [$10^6 M_\odot$]	F_{ion} [photons $\text{cm}^{-2} \text{ s}^{-1}$]	
			one-sided	isotropic
6	6.8	2.5	0.96×10^9	1.8×10^8
6	6.9	5.0	1.1×10^9	1.9×10^8
9	10.3	2.5	2.1×10^9	4.5×10^8
9	10.5	5.0	0.57×10^9	1.1×10^8
12	13.8	2.5	3.8×10^9	8.4×10^8
12	14.0	5.0	2.6×10^9	5.6×10^8
9	10.5	10.0	1.8×10^9	-
12	14.0	10.0	5.0×10^9	-

4.2 Effect of Tidal Field

Here, we briefly estimate the effect of tidal force by the host galaxy as with Hasegawa et al. (2009). The tidal radius r_t is roughly given by

$$\frac{Gm(r < r_t)}{r_t^2} \sim 2 \frac{GM_{\text{gal}}m(r < r_t)r_t}{r_{\text{gal}}^3} \quad (4.3)$$

where $m(r < r_t)$, M_{gal} , r_{gal} denote the cumulative cluster mass interior to the tidal radius, the host galaxy mass, and distance from the galactic center to the cluster, respectively. In the equation, the host galaxy is assumed as the point-mass. If we suppose the small galaxy with mass $M_{\text{gal}} = 10^9 M_{\odot}$, $r_{\text{gal}} = 0.3\text{-}1$ kpc, and using the mass distribution obtained in this study (Figure 3.11), the resultant tidal radii are obtained as $10 \text{ pc} \lesssim r_t \lesssim 100 \text{ pc}$ for star cluster formed via supersonic infall. As for the star cluster formed through supersonic infall, there is no cluster that tidal radius exceeds the half-mass radius. Thus, the compact stellar dominated component would survive regardless of tidal field, even though the diffuse DM component were stripped away. Consequently, the dynamical mass-to-light ratio (Figure 3.14) would not be significantly influenced by the effect of tidal force in the case of supersonic infall.

Here, it should be mentioned that the tidal field is thought to be drastically changed with time due to interacting of the host galaxies. Renaud & Gieles (2013) have performed the N -body simulation to reveal the role of the merging of the host galaxies on the evolution of the star cluster. As a result, they have found that the tidal perturbations caused by the galaxy-galaxy collisions do not significantly influence the structure of the star clusters since the effective tidal force can be canceled out locally due to the combination of two potentials. Furthermore, although it may be depending on the geometry of the encounter, the tidal perturbation would have a maximum influence at the time of passing the pericenter, and the time-scale to be too short to affect the star cluster. However, the collisions also indirectly affect the star cluster evolution by modifying the orbit of the clusters. That is, the tidal effect is to be weak if the star cluster ejected to a large distance from the galaxy center, while the star cluster remaining in the central region of the host tends to experience the high tidal force.

4.3 Velocity Dispersion Profile

Figure 4.1, 4.2 show the line-of-sight velocity dispersion profile for star clusters formed via supersonic infall. Also, best-fitting Plummer model (Lane et al. 2010) is overplotted.

As we see in the figures, the line-of-sight velocity dispersion decreases with distance from the center of the cluster and the profiles seem to obey more or less the Plummer model in most of the case. However, we also find that the profiles tend to deviate gradually from the Plummer model with distance from the center of the cluster, or to miss to reproduce the central velocity dispersion that would be caused by fitting to the outer part of the profile ($\gtrsim 10$ pc). They are caused by flattening of velocity dispersion profile. At the center of the cluster, radial part of velocity dominates and exhibits the peak in the profile, and the line-of-sight velocity dispersion decreases with distance from the center since the tangential component of velocity for line-of-sight gradually dominates rather than the radial part. However, the existence of DM tend to be negligible at the outer region of the cluster (as seen in Figure 3.11), and the gravity of DM component would contribute to the radial motion of stars. Hence, the cause of flattening is considered to be DM component.

In fact, though it is not necessarily the case, the flattening of line-of-sight velocity dispersion profile have been reported in observation (e.g., Scarpa et al. 2007). Typically, the GC have been considered as a DM-free star cluster, the flattening seems to be an interesting feature to consider the origin of GCs.

However, it should be noted that the explanation for the flattening is not limited to just the DM. Another possible candidate is a tidal heating, i.e., heating due to the external tidal force causes to increase the velocity dispersion at the outer part of the cluster. For instance, Lane et al. (2010) have investigated 10 of halo GGCs and found the flattening of the velocity dispersion in the profile of M4. Also, they have shown that the mass-to-ratio profile of the cluster exhibit order of unity even though the outskirts region of $r \sim r_h$ where flattening of velocity dispersion identified. Therefore, they have concluded that the tidal heating is the most suitable explanation for the flattening and the existence of DM component would be rejected. Since we have defined the dynamical mass as the total mass within the half-mass radius of the cluster, the dynamical mass-to-light ratio of our cluster exhibits the order of unity as shown in Figure 3.14. However, the mass-to-ratio profile of our clusters would increase with distance from the center (Figure 3.11), which is in contradiction to the observation. Therefore, it seems reasonable to conclude that the flattening of velocity dispersion profile in the outskirts region of the cluster is differently originated.

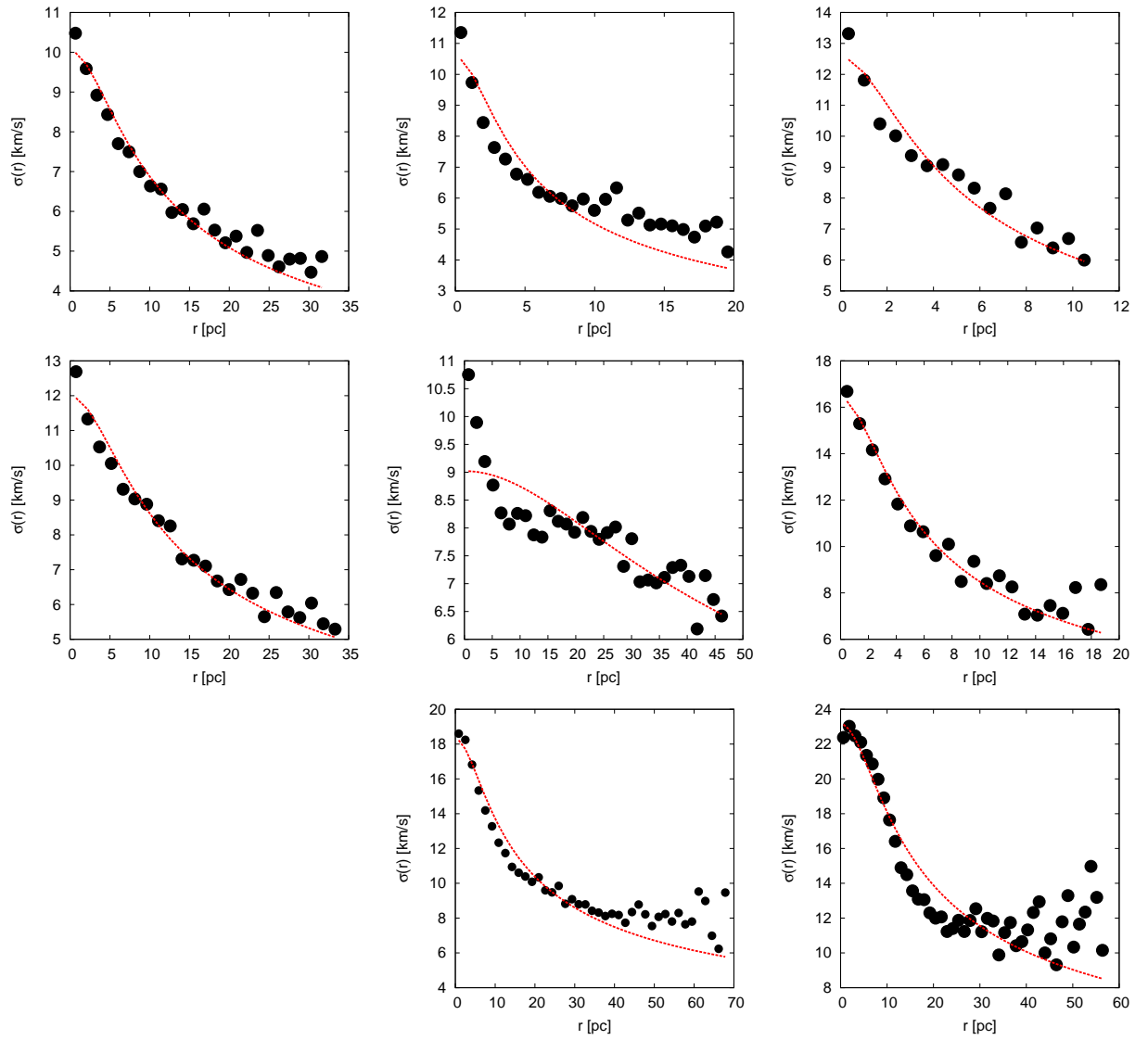


Fig. 4.1: Line-of-sight velocity dispersion profile for star cluster formed via supersonic-infall in one-sided background radiation. Red-line indicates best-fitting Plummer model (Lane et al. 2010).

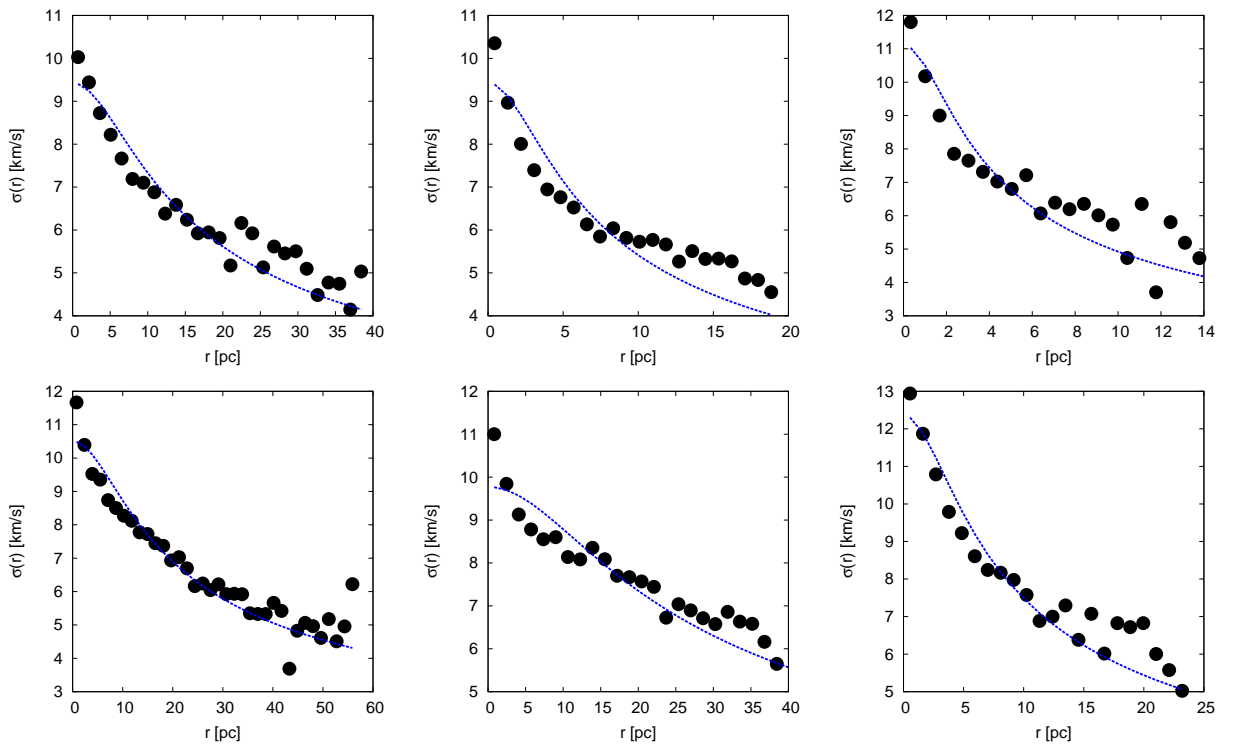


Fig. 4.2: Same as Figure 4.1, but for isotropic background radiation field. Blue line indicates the best-fitting Plummer model.

Chapter 5 Conclusions

In this study, we have performed the three-dimensional radiation hydrodynamical (RHD) simulation to explore the star cluster formation in UV background radiation field. In particular, contrary to the previous one-dimensional RHD calculation (Hasegawa et al. 2009), the anisotropy of background radiation, local self-shielding effect, and local star formation are newly taken into account.

We have found how the contraction of gas cloud and star formation takes place in three-dimensional background radiation as follows. In the case when the gas cloud is irradiated by intense radiation at the phase of its infall velocity exceeds the sound speed of the photoionized gas, the bulk of the cloud photoionized once but continues to contract (Hasegawa et al. 2009). Even in the case of the one-sided background radiation field, although the shaded region is not affected by the radiation, most of the cloud is photoionized and behaves as with isotropic background radiation case. Thus, high kinetic energy dissipation of photoionized gas is observed regardless of anisotropy of background radiation.

Because of the inhomogeneous density field of the cloud, the self-shielding, and star formation locally occur. However, we have revealed that the most of the stars form in sufficient compact region of ~ 10 pc. It is of particular importance that the result is not affected by an anisotropy of background radiation. On the other hand, if the gas cloud is irradiated at an early phase of contraction, star cluster can only form in a weak UV intensity field. In that case, the self-shielded region immediately formed and stars begin to form promptly in the vast area of $\gtrsim 100$ pc.

We have also pursued the stellar motion by N -body calculation and evaluated the dynamical feature of the star clusters. As for star clusters formed via supersonic infall of the photoionized gas, the stellar-dominated star cluster forms. This is because of the strong energy dissipation owing to the contraction of the high thermal gas. Contrary to that, star clusters formed in promptly self-shielded gas become to be diffuse, dark matter dominated stellar system since the dissipation does not effectively work before forming stars.

Our star clusters have been compared to observed dispersion supported low mass stellar system. As a result, the star cluster formed via supersonic infall seem to be in good agreement with observed GCs concerning half-mass radius, dynamical mass-to-light ratio, and its unique relation between the velocity dispersion σ and the luminosity L , $\sigma \propto L^{1/2}$. For the prompt star formation case, their properties seem to be in agreement with dSphs rather than GC. Consequently, we have shown that the dynamics of the star cluster is regulated background radiation. The background radiation field is thought to be the essential to determine the feature of low-mass star cluster formed at an early universe, but the anisotropy is not so crucial than expected.

Our result suggests that the primary key to form the GC-like compact star cluster is a strong UV background, corresponding to $J_{21} \sim 10^{2-3}$ or ionizing photon number flux $\sim 10^9 \text{ cm}^{-2} \text{ s}^{-1}$. At an early universe, Pop III stars, AGNs are the plausible candidate as the source of radiation.

Appendix A Other Suggestive Properties of Globular Clusters

A.1 Specific Frequency

Usually, the number of GC belong to the host galaxy is specified by the specific frequency S_N , given by

$$S_N = N_{\text{GC}} \times 10^{0.4(M_V+15)} \quad (\text{A.1})$$

where N_{GC} denotes the total number of the GC, and M_V is the absolute V-band magnitude of the host galaxy.

It is well known that the specific frequency depends on the morphology of the host galaxy (e.g., Peng et al. 2008; Harris et al. 2013, see Figure A.1). The specific frequency of the late-type galaxies typically show $S_N \sim 1$, but the luminous early-type galaxies exhibit the $S_N \gtrsim 10$. The higher specific frequency also appears in the dwarf galaxies.

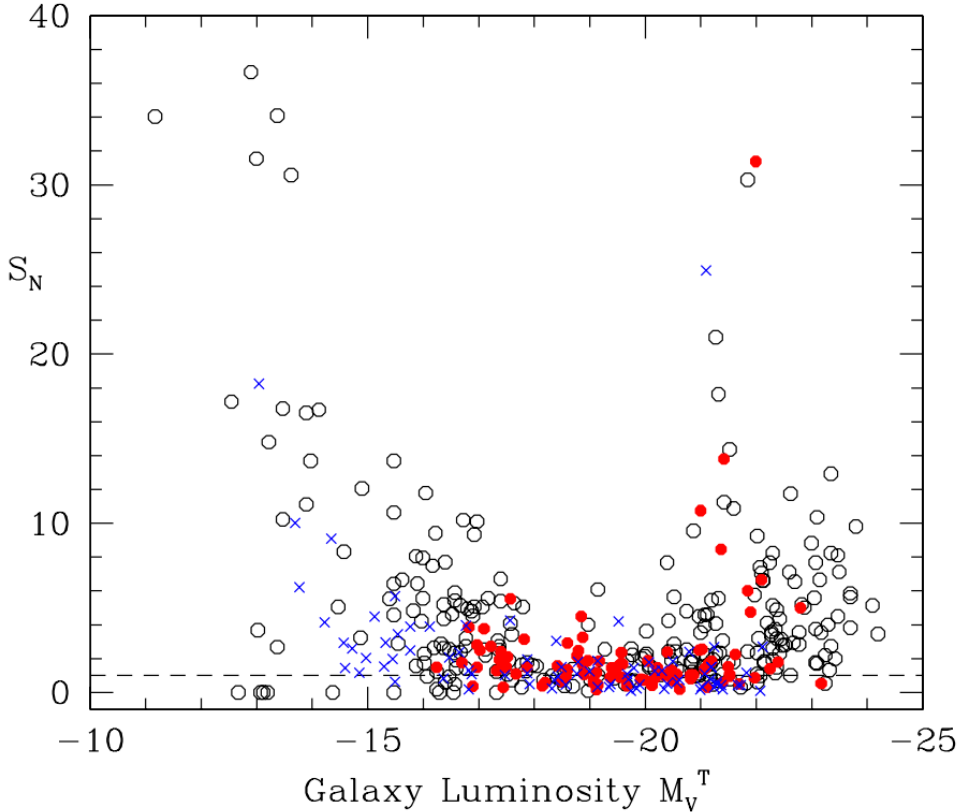


Fig. A.1: Specific frequency S_N vs. absolute V-band magnitude of the host galaxy M_V^T , taken from Figure 10 of Harris et al. (2013). Open circles represent Ellipticals and dwarf ellipticals. Filled red circle denotes the S0 galaxies. Cross denotes the spirals or irregulars.

The minimum mass of the host dwarf galaxy is thought to reflect the briefest unit of the link between

the GC formation and galaxy evolution in an early universe. From the observations, Brodie & Strader (2006) have discussed that the minimum mass of the host halo that contains the GCs seems to be $10^{7-8}M_{\odot}$ though it is still uncertain. One of the intriguing examples of such dwarf is the dIrr WLM (dynamical mass $\sim 10^8M_{\odot}$), which is an old system and contains only one old GC. The WLM may be an example of the formation site of the GC that remains the state of an early date without capturing by the larger systems. Interestingly, Elmegreen et al. (2012) have pointed the correlation between the early starburst epoch of WLM and the age of GC, implying the GC formation with strong UV background radiation.

A.2 Color Bimodality

The color divides the GCs into two subpopulations concerning the color, blue clusters, and red clusters. The fraction of each subpopulation depends on the mass of the host galaxy (Figure A.2); the low-mass galaxies tend to be dominated by blue GCs, and the fraction of red GCs increases with increasing the mass of the host galaxy (Peng et al. 2008). The two subpopulations are respectively old as $\gtrsim 10$ Gyr but slightly younger for red GCs (Strader et al. 2005), and the color bimodality is thought to be due to the metal abundance (Forbes 2005). In fact, the bimodality of the metallicity has been reported in the galaxies including MW (Zinn 1985; Bica et al. 2006; Puzia et al. 2005). Although the origin of the bimodality is still unclear, the blue (metal-poor) population may be particularly a remnant of star cluster formation in the early phase of the hierarchical merging process.

A.3 Age-Metallicity Relation

Marín-Franch et al. (2009) have studied the relative age and age-metallicity relation (AMR) for Galactic GCs (GGCs). As for the metal-poor GGCs ($[Fe/H] \lesssim -1.5$), they are the old stellar component, and the ages distribute with small dispersion ($\lesssim 0.8$ Gyr). Therefore, there is no evidence for age-metallicity relation. On the other hand, the metal-rich clusters exhibit an apparent age-metallicity relation (AMR). The ages distribute over the course of the time interval of ~ 6 Gyr. The AMR suggests the distinction concerning the origin of GCs.

Leaman et al. (2013) have investigated the AMR for GGCs. They have also considered the kinematics of GCs and classified them as either disc or halo population by using Bayesian probabilistic analysis. As a result, they have found that the AMR divides the GCs into the distinct parallel sequence at $[Fe/H] > -1.7$ (Figure A.3). The metal-rich sequence running from $[Fe/H] \sim -1.5$ to -0.4 and $\sim 10.5 - 13.0$ Gyr. They belong to the member of the disc population, thus, the clusters belong to metal-rich sequence seem to be formed in situ in the disc. The metal-poor sequence also spans $\sim 10.5 - 13.0$ Gyr but locates offset of ~ 0.6 dex in $[Fe/H]$. Contrary to the previous sequence, they belong to halo population. Their kinematical classification suggests that the clusters belong to metal-poor sequence have formed in other galaxies and later accreted by MW. In conjunction with the mass-metallicity relation (MMR) for galaxies (e.g., Kirby et al. 2011), and a simple assumption that the GCs trace the metallicity of the host galaxy, the offset in AMR predicts the progenitor host galaxy stellar masses of the metal-poor GCs. They have derived the stellar mass of the progenitor and concluded that the metal-poor halo cluster were formed in relatively low-mass dwarf galaxies (stellar mass of $\sim 10^{5-9}M_{\odot}$) and accreted by MW. Their prediction is in good agreement with numerical simulations of the MW-sized galaxy in Λ CDM cosmology. The interesting implication of their work is that it is likely to be difficult to consider to that the 'metal-rich cluster in metal-poor sequence' forms in situ in the disc.

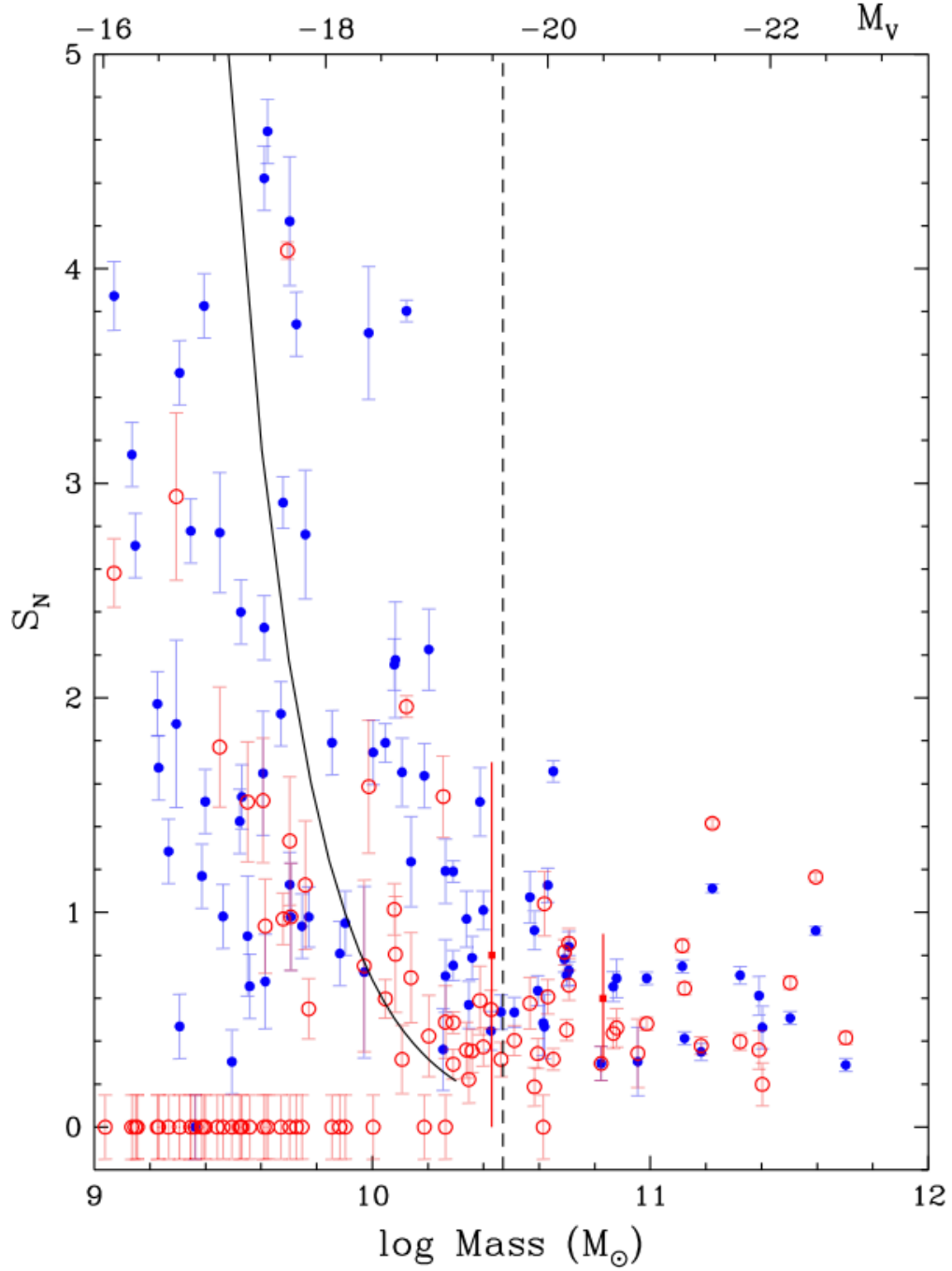


Fig. A.2: Specific frequency S_N vs. host galaxy stellar mass in the unit of M_{\odot} , taken from Figure 1 of Forbes (2005). Blue filled circle denotes the blue GCs, and the open red circle is the red GCs.

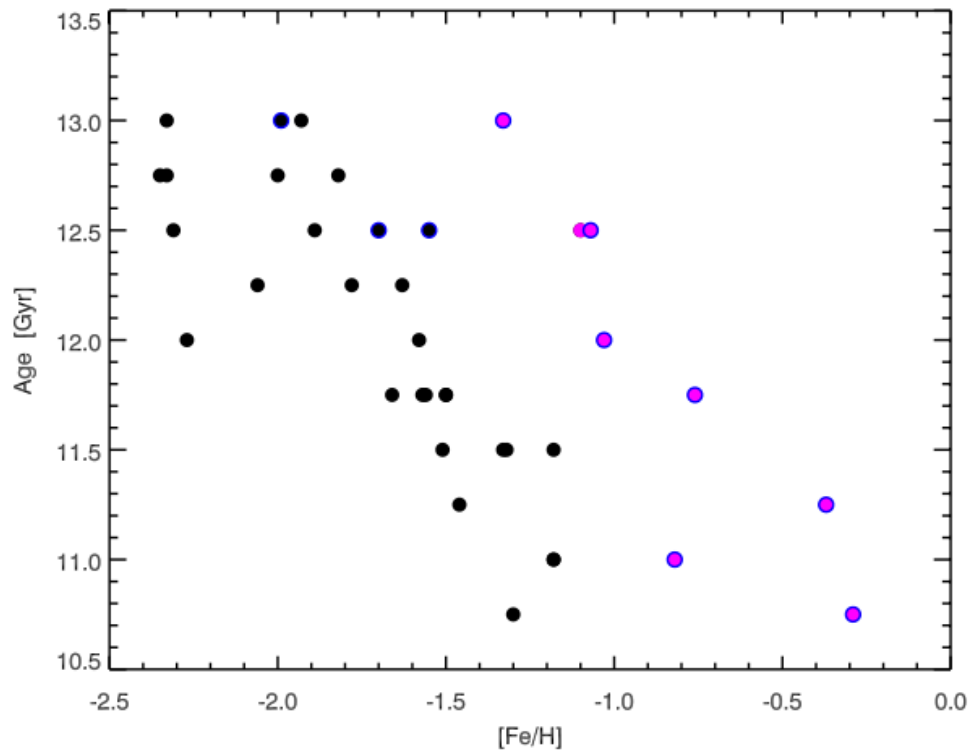


Fig. A.3: Age-metallicity relation (AMR) for the MW GGCs, taken from Figure 2 of Leaman et al. (2013). The blue circles represent clusters which are classified as disc-like kinematics, and the magenta indicates the disc cluster determined 'by eye' regarding their offset in the AMR. The black circles denote the halo GCs.

Appendix B Realization of Random-Gaussian Density Field

As for initial density distribution, we generate the random-Gaussian density fluctuation that obeys a given power spectrum $P(k)$ as below.

First of all, a uniform sphere of which the particles are distributed in a reticular pattern is considered. The density fluctuation is generated by moving the particles from the grid point and perturbing the initial density field. The perturbation vector $\vec{\Psi}$ is given by superimposing the waves that have a random phase,

$$\vec{\Psi}(\vec{r}_0) = \sum_i^{N_k} \sin(\vec{k}_i \cdot \vec{r}_0 + \phi_i) \frac{\vec{k}_i}{k_i^2} \left[\frac{P_i}{w(k_i)} \right] \quad (\text{B.1})$$

where \vec{r}_0 denotes the initial grid position vector for a particle. $P_i^{1/2}$ indicates the normal random number given by a Gaussian distribution with the variance of $P(k_i)$, and ϕ_i is a uniform random number distributed in an interval of $(0, 2\pi)$. \vec{k}_i is a vector distributed randomly in k -space, and the direction of perturbation vector is given by a wave number vector \vec{k}_i . The k_i (the norm of \vec{k}_i) is randomly chosen from the range of (k_{\min}, k_{\max}) with wave number density of $w(k)$. The wave number density $w(k)$ is given by

$$w(k)d^3k = \frac{N_k}{u(k_{\max}) - u(k_{\min})} du(k) \quad (\text{B.2})$$

For instance, for a constant wave number density is assumed, $u(k) = k^3$, thus, each k_i is uniformly distributed in k -space. In this study, we assume $u(k)$ as $u(k) = \ln k$ in common with Braun et al. (1988) so that the k_i distribute uniformly in logarithmic scale. In this instance, $w(k)$ is described as

$$w(k) = \frac{N_k}{4\pi(\ln k_{\max} - \ln k_{\min})} k^{-3} \quad (\text{B.3})$$

Through this study, we generate the $N_k = 2^{15}$ wave number vectors satisfy the condition described above, and obtained the perturbation vector in accordance with equation (B.1).

In practical steps, we first generate the cloud which obeys the profile $\delta(r)$ from the uniform sphere.

Here, we consider the second density fluctuation $\delta'(r)$ with respect to the mean density of the cloud $\bar{\rho}$, rather than critical density ρ_c . At the moment of maximum expansion, the $\bar{\rho}$ is given by $\bar{\rho} = \alpha\rho_c$ where α denotes the density contrast $9\pi^2/16$ (equation 2.76). Immediately, we find the relation

$$\bar{\delta}(r) + 1 = \alpha(\delta' + 1) \quad (\text{B.4})$$

Then, we can set the relation between r and first grid position r_0 as

$$\frac{1/r^3 - 1/r_0^3}{1/r_0^3} = \bar{\delta}'(r) \quad (\text{B.5})$$

Consequently, the new position r that reproduces the overdensity profile $\delta(r)$ is determined by iteratively solving the equation

$$\alpha r^3(\bar{\delta}(r) + 1) - r_0^3 = 0 \quad (\text{B.6})$$

Appendix C Estimation of Ionizing Photon Number Incident on the Cloud

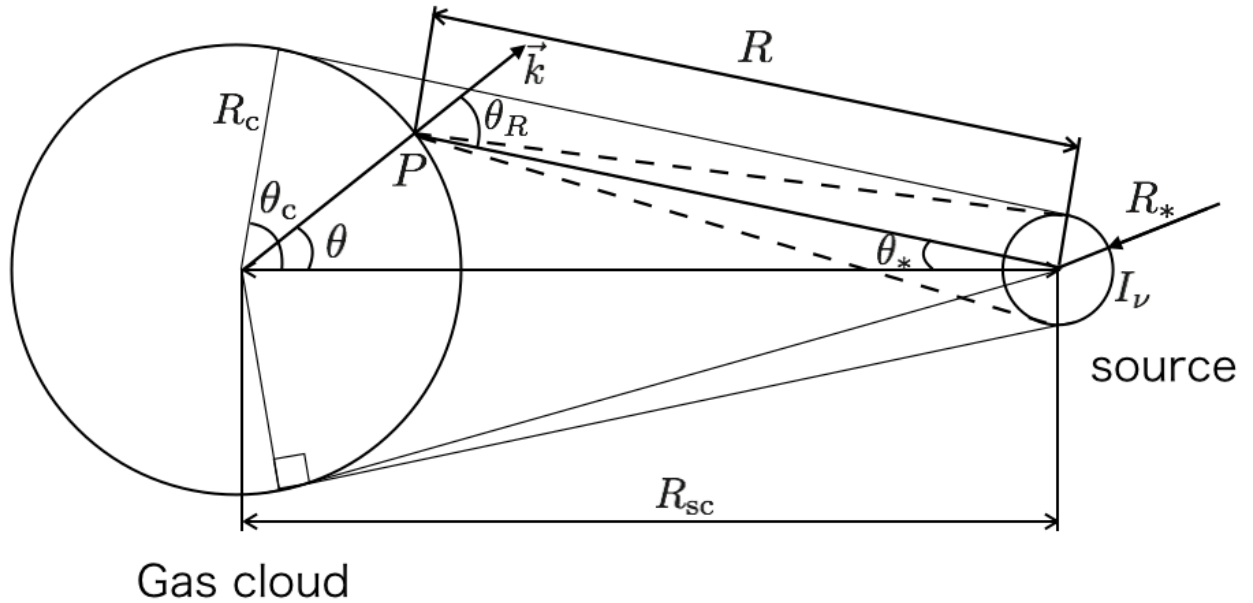


Fig. C.1: Conceptual diagram for the gas cloud radius of R_c that irradiated by a source located at the distance of R_{sc} from the center of the cloud.

Suppose the situation that the cloud radius of R_c is irradiated by a source which is located at a distance of R_{sc} , as shown in Figure C.1. The source intensity I_ν is assumed as isotropic (independent of direction) and has a radius of R_* . Now, we determine the ionizing photon number \dot{N}_{ion} incident upon the cloud as follow.

The flux at point P can be obtained with consideration for unit vector \vec{k} that is normal to the surface of the cloud, namely

$$F_\nu(R, \theta) = \int d\Omega \vec{n} I_\nu \sim I_\nu \cos \theta_R \Delta\Omega = I_\nu \cos \theta_R 4\pi W(R) \quad (\text{C.1})$$

where R is the distance from P to the center of the source. $W(R)$ denotes the dilution factor, defined by dividing the viewing angle at P with respect to the source by 4π . If we suppose the condition $R \gg R_*$, $W(R) \sim R_*^2/4R^2$ can be obtained. $\theta_R = \theta + \theta_*$ denotes the angle between the ray and a normal vector \vec{k} . The term $\cos \theta_R$ means the correction for projection of vertical surface with respect to the direction of the ray.

The ionizing photon number flux $\equiv F_{\text{ion}}$ is given by

$$F_{\text{ion}} = \int_{\nu_L}^{\infty} d\nu \frac{F_\nu}{h\nu} \quad (\text{C.2})$$

For the sake of expedience, we also define the term

$$\int_{\nu_L}^{\infty} d\nu \frac{I_\nu}{h\nu} \equiv \dot{i} \quad (\text{C.3})$$

If we suppose a minute surface area $dS = R_c^2 \sin \theta d\theta d\phi$ at the point P , ionizing photon number incident upon the minute surface is given by $\dot{N}_{\text{ion}} = F_{\text{ion}} dS$. Therefore, total ionizing photon number incident onto the cloud is obtained by integrating about all surface area that exposed to radiation, thus

$$\begin{aligned} \dot{N}_{\text{ion}} &= 4\pi \dot{i} R_c^2 \int_0^{2\pi} d\phi \int_0^{\theta_c} d\theta W(R) \cos \theta_R \sin \theta \\ &= 2\pi^2 \dot{i} R_c^2 \int_0^{\theta_c} d\theta \frac{R_*^2}{R^2} \cos(\theta + \theta_*) \sin \theta \end{aligned} \quad (\text{C.4})$$

According to a law of cosines, the relation $R^2 = R_c^2 + R_{\text{sc}}^2 - 2R_c R_{\text{sc}} \cos \theta$ is derived. Furthermore, we find $\cos \theta_* = (R_{\text{sc}} - R_c \cos \theta) / R$ from Figure C.1.

Consequently, equation (C.4) can be rewritten as

$$\begin{aligned} \dot{N}_{\text{ion}} &= 2\pi^2 \dot{i} R_c^2 R_*^2 \int_0^{\theta_c} d\theta \frac{\sin \theta}{R^2} \left(\frac{R_{\text{sc}}}{R} \cos \theta - \frac{R_c}{R} \right) \\ &= 2\pi^2 \dot{i} R_c^2 R_*^2 \int_0^{\theta_c} d\theta \frac{\sin \theta (R_{\text{sc}} \cos \theta - R_c)}{(R_c^2 + R_{\text{sc}}^2 - 2R_c R_{\text{sc}} \cos \theta)^{3/2}} \end{aligned} \quad (\text{C.5})$$

This integration can be solved analytically as

$$\dot{N}_{\text{ion}} = 2\pi^2 \dot{i} R_c^2 R_*^2 \left[\frac{R_c - R_{\text{sc}} \cos \theta}{R_{\text{sc}} R_c (R_c^2 + R_{\text{sc}}^2 - 2R_c R_{\text{sc}} \cos \theta)^{1/2}} - \frac{(R_c^2 + R_{\text{sc}}^2 - 2R_c R_{\text{sc}} \cos \theta)^{1/2}}{R_{\text{sc}} R_c^2} \right]_0^{\theta_c} \quad (\text{C.6})$$

If the radius of the source is sufficiently small compared to the cloud radius, we can assume the relation $\cos \theta_c \sim R_c / R_{\text{sc}}$. Eventually, \dot{N}_{ion} is given by

$$\dot{N}_{\text{ion}} = 2\pi^2 \dot{i} R_*^2 \left[1 - \frac{(R_{\text{sc}}^2 - R_c^2)^{1/2}}{R_{\text{sc}}} \right] \quad (\text{C.7})$$

Appendix D Ray-Tracing in SPH Scheme

Kessel-Deynet & Burkert (2000) have developed the SPH scheme coupled with radiation transfer by using the neighbor particle and creating the grid point on the light ray. The schematic view of their method appears in Figure D.1. Suppose that we try to evaluate the optical depth of the target particle (represented

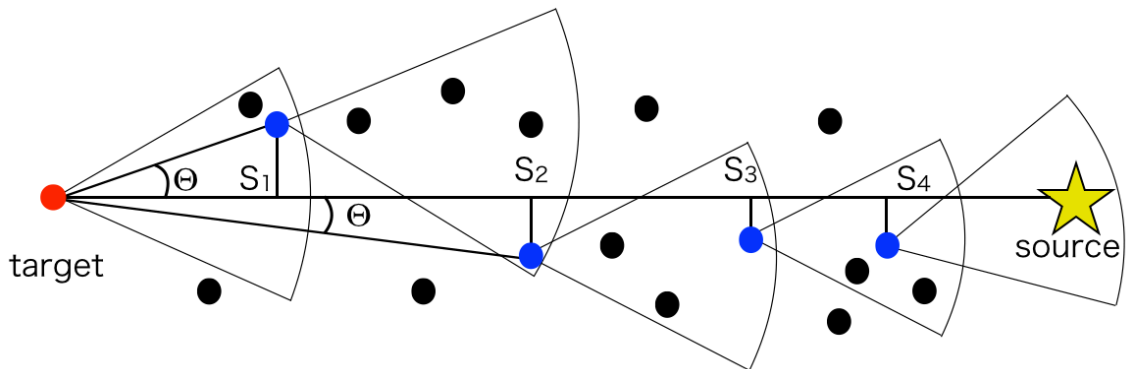


Fig. D.1: Schematic figure for ray-tracing in the scheme of Kessel-Deynet & Burkert (2000). Each circle represents the target particle (red colored), the upstream particle (blue colored, see the text), and others.

by the red particle in Figure D.1). At first, the upstream particle is selected from the neighbor list of the target particle (the blue particle). The upstream particle has the smallest angle Θ with respect to the ray, i.e., the closest particle to the ray is chosen. The grid point is created by projecting the particle position onto the ray (denoted as S_1). Then, the next upstream particle is selected from the neighbor particle of the present upstream particle, which also has the smallest angle Θ , and creates the grid point in turn. The procedure is repeated until the particle finds the source. As a result, the optical depth from the source to the target is given by

$$\tau_i = \sum_j \frac{\sigma}{2} (n_{j+1} + n_j) (S_{j+1} - S_j) \quad (\text{D.1})$$

where σ denotes the cross-section, n_j is the number density at the i -th grid point, and S_i is the position on the ray. The integration is calculated by the trapezoidal approximation.

In this method, average evaluation point on the light ray is $N_{\text{SPH}}^{1/3}$, where N_{SPH} denotes the total number of SPH particle, and the procedure should be done for all particle. Therefore, the computational cost for ray-tracing is evaluated as $\propto N_{\text{SPH}}^{1/3} N_{\text{SPH}} N_{\text{source}}$, where N_{source} indicates the number of the source.

Through this study, we adopt the RSPH scheme developed by Susa (2006). The schematic view of RSPH is shown in Figure D.2. In RSPH, the optical depth of the i -th particle is calculated as follows.

First, the upstream particle is determined from the neighbor list of the i -th particle. The upstream particle should be the most closet particle to the light-ray, which is simply determined by the angle θ_{ij} (Figure D.2, the blue-labeled particle is selected as the upstream particle). Then, a grid point is created on the ray. The grid is determined as the point at the intersection of the sphere of radius r_j (represented by the dotted line in Figure D.2) with the ray. The physical values of the j -th particle are projected onto the grid. Then, the differential optical depth between the j -th and the i -th particle $\Delta\tau_{ij}$ is calculated as simply

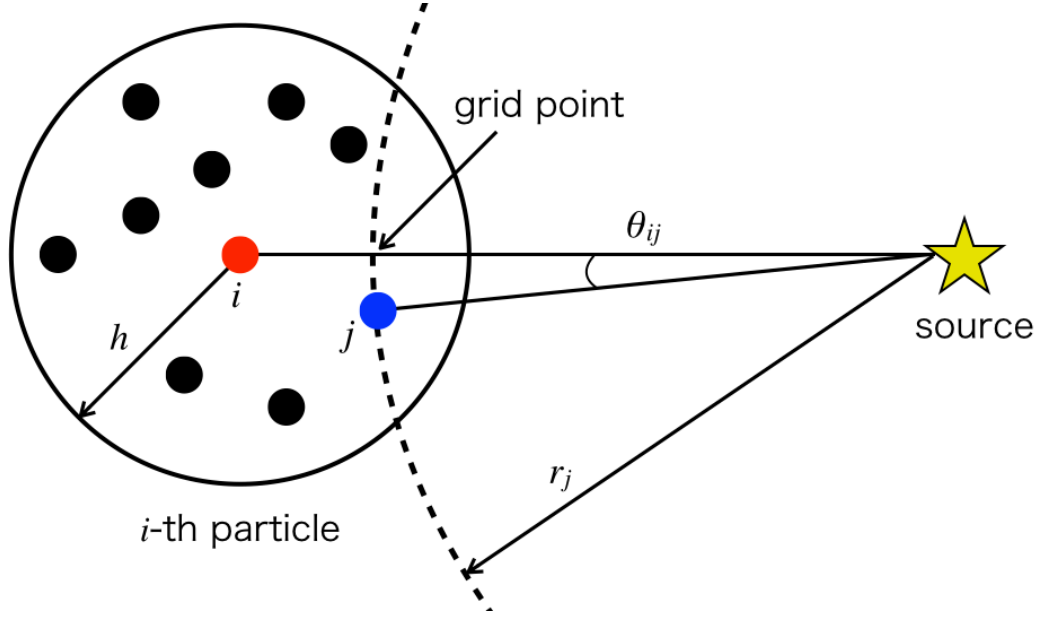


Fig. D.2: Schematic figure for ray-tracing in RSPH scheme. The target particle (red point) and its neighbor particles are shown. The upstream particle (see the text) is represented as the blue point. The h denotes the smoothing length of the target particle.

by the trapezoidal approximation, namely,

$$\Delta\tau_{ij} = \frac{\sigma}{2} (n_i + n_j) \quad (\text{D.2})$$

As the result, the optical depth τ_i is obtained as

$$\tau_i = \Delta\tau_{ij} + \tau_j \quad (\text{D.3})$$

where τ_j denotes the optical depth of j -th particle, which is already calculated in agreement with the same procedure.

Therefore, we need the information of only one upstream SPH particle to calculate the new optical depth contrary to the method of Kessel-Deynet & Burkert (2000).

Consequently, the computational cost for the ray-tracing is evaluated as $\propto N_{\text{SPH}} N_{\text{source}}$.

Acknowledgments

I am particularly grateful to my supervisor Masayuki Umemura of insightful discussion, valuable advice, and strong supports throughout my doctoral program in physics. I also appreciate so much Kenji Hasegawa for providing the simulation code, useful suggestions, helpful comments, and his kindness.

I am grateful to Masao Mori, Kohji Yoshikawa, Alexander Y. Wagner, Daisuke Namekata, Go Ogiya, Yohei Miki, Mariko Nomura, Yu Komatsu, Satoshi Tanaka, Asuka Igarashi, Takanobu Kirihara, Hiroyuki Suzuki and other present and/or past members of astrophysics division for their scientific, and non-scientific supports.

I am very thankful to Masao Mori, Kohji Yoshikawa, and Fumitaka Nakamura for their constructive comments that have improved my doctoral thesis.

Special thanks also to Andreas Burkert for the valuable discussions and his kindness when I stayed at Ludwig Maximilians University.

Finally, I am grateful to my family for their numerous supports.

References

- [1] Barnes, J., & Hut, P. 1986, *Nature*, 324, 446
- [2] Bate, M. R., Bonnell, I. A., & Bromm, V. 2003, *MNRAS*, 339, 577
- [3] Bate, M. R., & Burkert, A. 1997, *MNRAS*, 288, 1060
- [4] Bica, E., Bonatto, C., Barbuy, B., & Ortolani, S. 2006, *A&A*, 450, 105
- [5] Braun, E., Dekel, A., & Shapiro, P. R. 1988, *ApJ*, 328, 34
- [6] Brodie, J. P., & Strader, J. 2006, *ARA&A*, 44, 193
- [7] Chiba, M., & Beers, T. C. 2000, *AJ*, 119, 2843
- [8] Diemand, J., Madau, P., & Moore, B. 2005, *MNRAS*, 364, 367
- [9] Dotter, A., Chaboyer, B., Jevremović, D., et al. 2007, *AJ*, 134, 376
- [10] Draine, B. T., & Bertoldi, F. 1996, *ApJ*, 468, 269
- [11] Drinkwater, M. J., Gregg, M. D., Hilker, M., et al. 2003, *Nature*, 423, 519
- [12] Durrell, P. R., & Harris, W. E. 1993, *AJ*, 105, 1420
- [13] Eggen, O. J., Lynden-Bell, D., & Sandage, A. R. 1962, *ApJ*, 136, 748
- [14] Elmegreen, B. G., Malhotra, S., & Rhoads, J. 2012, *ApJ*, 757, 9
- [15] Faber, S. M., & Jackson, R. E. 1976, *ApJ*, 204, 668
- [16] Fall, S. M., Chandar, R., & Whitmore, B. C. 2005, *ApJ*, 631, L133
- [17] Fan, X., Carilli, C. L., & Keating, B. 2006, *ARA&A*, 44, 415
- [18] Forbes, D. A. 2005, *ApJ*, 635, L137
- [19] Forbes, D. A., Lasky, P., Graham, A. W., & Spitler, L. 2008, *MNRAS*, 389, 1924
- [20] Fukugita, M., & Kawasaki, M. 1994, *MNRAS*, 269, 563
- [21] Galli, D., & Palla, F. 1998, *A&A*, 335, 403
- [22] Giallongo, E., Grazian, A., Fiore, F., et al. 2015, *A&A*, 578, A83
- [23] Glikman, E., Djorgovski, S. G., Stern, D., et al. 2011, *ApJ*, 728, L26
- [24] Hasegan, M., Jordán, A., Côté, P., et al. 2005, *ApJ*, 627, 203
- [25] Harris, W. E. 1996, *AJ*, 112, 1487
- [26] Harris, W. E., Harris, G. L., & Hudson, M. J. 2015, *ApJ*, 806, 36

- [27] Harris, W. E., Harris, G. L. H., & Alessi, M. 2013, *ApJ*, 772, 82
- [28] Hasegawa, K., & Umemura, M. 2010, *MNRAS*, 407, 2632
- [29] Hasegawa, K., Umemura, M., & Kitayama, T. 2009, *MNRAS*, 397, 1338
- [30] Hinshaw, G., Larson, D., Komatsu, E., et al. 2013, *ApJS*, 208, 19
- [31] Hirano, S., Hosokawa, T., Yoshida, N., Omukai, K., & Yorke, H. W. 2015, *MNRAS*, 448, 568
- [32] Iliev, I. T., Ciardi, B., Alvarez, M. A., et al. 2006, *MNRAS*, 371, 1057
- [33] Iliev, I. T., Whalen, D., Mellema, G., et al. 2009, *MNRAS*, 400, 1283
- [34] Kessel-Deynet, O., & Burkert, A. 2000, *MNRAS*, 315, 713
- [35] Kirby, E. N., Lanfranchi, G. A., Simon, J. D., Cohen, J. G., & Guhathakurta, P. 2011, *ApJ*, 727, 78
- [36] Kitayama, T., Susa, H., Umemura, M., & Ikeuchi, S. 2001, *MNRAS*, 326, 1353
- [37] Kormendy, J. 1985, *ApJ*, 295, 73
- [38] Krauss, L. M., & Chaboyer, B. 2003, *Science*, 299, 65
- [39] Kravtsov, A. V., & Gnedin, O. Y. 2005, *ApJ*, 623, 650
- [40] Lada, C. J., & Lada, E. A. 2003, *ARA&A*, 41, 57
- [41] Lane, R. R., Kiss, L. L., Lewis, G. F., et al. 2010, *MNRAS*, 406, 2732
- [42] Leaman, R., VandenBerg, D. A., & Mendel, J. T. 2013, *MNRAS*, 436, 122
- [43] Madau, P., & Haardt, F. 2015, *ApJ*, 813, L8
- [44] Madau, P., Haardt, F., & Rees, M. J. 1999, *ApJ*, 514, 648
- [45] Marín-Franch, A., Aparicio, A., Piotto, G., et al. 2009, *ApJ*, 694, 1498
- [46] Martini, P., & Ho, L. C. 2004, *ApJ*, 610, 233
- [47] Mateo, M. L. 1998, *ARA&A*, 36, 435
- [48] McConnachie, A. W. 2012, *AJ*, 144, 4
- [49] McLaughlin, D. E. 2000, *ApJ*, 539, 618
- [50] Meurer, G. R., Heckman, T. M., Leitherer, C., et al. 1995, *AJ*, 110, 2665
- [51] Mieske, S., Hilker, M., Jordán, A., et al. 2008, *A&A*, 487, 921
- [52] Monaghan, J. J. 1992, *ARA&A*, 30, 543
- [53] Moore, B., Diemand, J., Madau, P., Zemp, M., & Stadel, J. 2006, *MNRAS*, 368, 563
- [54] Nakamoto, T., Umemura, M., & Susa, H. 2001, *MNRAS*, 321, 593
- [55] Okamoto, T., Eke, V. R., Frenk, C. S., & Jenkins, A. 2005, *MNRAS*, 363, 1299
- [56] Okamoto, T., Jenkins, A., Eke, V. R., Quilis, V., & Frenk, C. S. 2003, *MNRAS*, 345, 429
- [57] Omukai, K., Tsuribe, T., Schneider, R., & Ferrara, A. 2005, *ApJ*, 626, 627

- [58] Ouchi, M., Shimasaku, K., Furusawa, H., et al. 2010, *ApJ*, 723, 869
- [59] Peng, E. W., Jordán, A., Côté, P., et al. 2008, *ApJ*, 681, 197
- [60] Perryman, M. A. C., Lindegren, L., Kovalevsky, J., et al. 1997, *A&A*, 323
- [61] Pirzkal, N., Malhotra, S., Rhoads, J. E., & Xu, C. 2007, *ApJ*, 667, 49
- [62] Planck Collaboration, Ade, P. A. R., Aghanim, N., et al. 2014, *A&A*, 571, A16
- [63] —. 2015, ArXiv e-prints, arXiv:1502.01589
- [64] Price, D. J., & Monaghan, J. J. 2007, *MNRAS*, 374, 1347
- [65] Pryor, C., & Meylan, G. 1993, in *Astronomical Society of the Pacific Conference Series*, Vol. 50, *Structure and Dynamics of Globular Clusters*, ed. S. G. Djorgovski & G. Meylan, 357
- [66] Puzia, T. H., Perrett, K. M., & Bridges, T. J. 2005, *A&A*, 434, 909
- [67] Renaud, F., & Gieles, M. 2013, *MNRAS*, 431, L83
- [68] Saitoh, T. R., Daisaka, H., Kokubo, E., et al. 2009, *PASJ*, 61, 481
- [69] Saitoh, T. R., Daisaka, H., Kokubo, E., et al. 2011, in *IAU Symposium*, Vol. 270, *Computational Star Formation*, ed. J. Alves, B. G. Elmegreen, J. M. Girart, & V. Trimble, 483–486
- [70] Saitoh, T. R., Koda, J., Okamoto, T., Wada, K., & Habe, A. 2006, *ApJ*, 640, 22
- [71] Salaris, M., Weiss, A., & Percival, S. M. 2004, *A&A*, 414, 163
- [72] Scarpa, R., Marconi, G., Gilmozzi, R., & Carraro, G. 2007, *A&A*, 462, L9
- [73] Schaerer, D. 2002, *A&A*, 382, 28
- [74] Schiavon, R. P., Rose, J. A., Courteau, S., & MacArthur, L. A. 2005, *ApJS*, 160, 163
- [75] Searle, L., & Zinn, R. 1978, *ApJ*, 225, 357
- [76] Shapiro, P. R., & Kang, H. 1987, *ApJ*, 318, 32
- [77] Shapley, H., & Shapley, M. B. 1919, *ApJ*, 50, doi:10.1086/142486
- [78] Spitzer, L. 1978, *Physical processes in the interstellar medium*
- [79] Springel, V. 2010, *ARA&A*, 48, 391
- [80] Springel, V., & Hernquist, L. 2002, *MNRAS*, 333, 649
- [81] —. 2003, *MNRAS*, 339, 312
- [82] Stancil, P. C. 1994, *ApJ*, 430, 360
- [83] Strader, J., Brodie, J. P., Cenarro, A. J., Beasley, M. A., & Forbes, D. A. 2005, *AJ*, 130, 1315
- [84] Susa, H. 2006, *PASJ*, 58, 445
- [85] Susa, H., & Umemura, M. 2004, *ApJ*, 600, 1
- [86] Susa, H., Umemura, M., & Hasegawa, K. 2009, *ApJ*, 702, 480
- [87] Tajiri, Y., & Umemura, M. 1998, *ApJ*, 502, 59

- [88] Taylor, M. A., Puzia, T. H., Gomez, M., & Woodley, K. A. 2015, *ApJ*, 805, 65
- [89] Tegmark, M., Silk, J., Rees, M. J., et al. 1997, *ApJ*, 474, 1
- [90] Thacker, R. J., Tittley, E. R., Pearce, F. R., Couchman, H. M. P., & Thomas, P. A. 2000, *MNRAS*, 319, 619
- [91] Tollerud, E. J., Bullock, J. S., Graves, G. J., & Wolf, J. 2011, *ApJ*, 726, 108
- [92] Totani, T., Kawai, N., Kosugi, G., et al. 2006, *PASJ*, 58, 485
- [93] VandenBerg, D. A., Brogaard, K., Leaman, R., & Casagrande, L. 2013, *ApJ*, 775, 134
- [94] Whitmore, B. C., & Schweizer, F. 1995, *AJ*, 109, 960
- [95] Whitmore, B. C., Zhang, Q., Leitherer, C., et al. 1999, *AJ*, 118, 1551
- [96] Wilkinson, M. I., & Evans, N. W. 1999, *MNRAS*, 310, 645
- [97] Yajima, H., Li, Y., Zhu, Q., et al. 2014, *MNRAS*, 440, 776
- [98] Yoshida, N., Abel, T., Hernquist, L., & Sugiyama, N. 2003, *ApJ*, 592, 645
- [99] Zinn, R. 1985, *ApJ*, 293, 424